Electronic and transport properties in carbon nano structures

Wei Chen

A dissertationsubmitted in partial fulfillment of
the requirements for the degree of

Doctor of Philosophy

University of Washington

2011

Program Authorized to Offer Degree: Department of Physics

University of Washington
Graduate School

This is to certify that I have examined this copy of a doctoral dissertation by

Wei Chen

and have found that it is complete and satisfactory in all respects,
and that any and all revisions required by the final
examining committee have been made.

Chair of the Supervisory Committee:

_____
Anton Andreev

Reading Committee:

_____
Anton Andreev

_____
Marcel den Nijs

_____
David Cobden

_____
Dam Thanh Son

Date: _____

In presenting this dissertation in partial fulfillment of the requirements for the doctoral degree at the University of Washington, I agree that the Library shall make its copies freely available for inspection. I further agree that extensive copying of this dissertation is allowable only for scholarly purposes, consistent with "fair use" as prescribed in the U.S. Copyright Law. Requests for copying or reproduction of this dissertation may be referred to Proquest Information and Learning, 300 North Zeeb Road, Ann Arbor, MI 48106-1346, 1-800-521-0600, to whom the author has granted "the right to reproduce and sell (a) copies of the manuscript in microform and/or (b) printed copies of the manuscript made from microform."

Signature_____

Date_____

University of Washington

Abstract

Electronic and transport properties in carbon nano structures

Wei Chen

Chair of the Supervisory Committee:
Professor Anton Andreev
Department of Physics

This dissertation studies the electronic and transport properties in one and two dimensional carbon systems, including carbon nanotubes, carbon chains and graphene. The focus is on the effects of e-e interaction on these properties. First we studied the electron band structure of armchair CNTs under interaction. The interactions destroy the metallic ground states in the non interacting picture and open a gap in the electron energy spectrum. The e-e interaction results in a Mott transition and opens a Mott gap while the e-phonon interaction leads to a Peierls transition and opens a Peierls gap accompanied by a lattice deformation. We examined both transitions and studied the interplay of the two interactions. The final ground state of an armchair CNT is discussed based on the studies of the two transitions. Next, the transport properties and energy dissipation of a two terminal carbon nanotube device are studied and the relation between the conductivity and the plasmon decay rate is explored. Particularly, the plasmon decay rate was evaluated and the correction to the conductance due to the interaction was studied in both undoped and doped case. While a uniform doping suppresses the Umklapp processes exponentially and for that reason a long armchair CNT remains metallic, in the non uniformly doped case, particularly in an armchair CNT pn junction, the relevance of the Umklapp scattering can be tuned by the doping electric field. Depending on the steepness of the doping potential, the device can go through a quantum phase transition from

a metal to insulator at zero temperature. The behavior near this critical point was studied by the epsilon expansion. At last, we studied the electron transport through a device composed of a one dimensional chain or wire connected to two graphene leads. Electrons get through the device by narrow resonance states with certain energies due to the vanishing density of states of the graphene leads at the junction. This feature of transport can be generalized to other molecular devices with graphene leads.

TABLE OF CONTENTS

Page

List of Figures 3

Chapter 1: Introduction 1
1.1 Bosonization and Luttinger liquid theory 1
1.2 Overview of the dissertation 6

Chapter 2: Electron structure in a strongly correlated armchair CNT . . . 10
2.1 Introduction 10
2.2 Non-interacting spectrum of carbon nanotubes 12
2.3 Luttinger liquid theory and Mott transition in the CNT 15
2.4 Peierls transition in the armchair CNT in the Luttinger liquid theory framework 20
2.5 Competition between Pierls and Mott transition and the ground state of an armchair CNT 27

Chapter 3: Plasmon decay in armchair carbon nanotubes 29
3.1 Introduction 29
3.2 Plasmon resonance in the absence of intrinsic dissipation 31
3.3 Intrinsic plasmon decay due to back scattering in the device 33
3.4 Summary of the results 44

Chapter 4: Quantum criticality in an armchair carbon nanotube pn junction 47
4.1 Introduction 47
4.2 Perturbation theory of the transport through an armchair CNT pn junction and quantum phase transition 48
4.3 Epsilon expansion approach near the intermediate fixed point 57
4.4 The role of e-phonon interaction and magnetic field 60
4.5 Conclusion 61

Chapter 5: Transport of molecule devices with graphene leads 63
5.1 Introduction 63
5.2 Qualitative discussion 65
5.3 System and model 70
5.4 Device conductance at low energies: asymmetric resonances 81
5.5 Summary and discussion 82

Appendix A: Green function of free Phonons and Bosonic fields 85

Appendix B: fusion rules 87

Appendix C: Renormalization group equations in the marginally irrelevant backscattering case 88

Appendix D: Derivation of the Green function of a half graphene sheet 90

Bibliography 91

LIST OF FIGURES

Figure Number Page

1.1 (a)schematic picture of electron hole excitation spectrum of 2D and 3D systems. (b) Electron hole excitation spectrum of 1D system. The spectrum has a well defined dispersion relation at small q. (c)A schematic picture of the displacement field ϕ as a function of position. 2

2.1 (a) Schematic picture of a graphene sheet. (b) 2D electron spectrum of a graphene sheet. (c)Reciprocal lattice of the graphene sheet in (a). (d)Schematic picture of an armchair carbon nanotube and its non interacting electron spectrum. Green and blue circles denote atoms in the A and B sublattices. The arrows show atomic displacements in the TA and LO phonon modes. + and − denote the parity of the bands. $\alpha = \pm 1$ corresponds to the two valleys with Fermi points at $\pm k_F$. . . 13

2.2 Schematic Feynmann diagram of the TA and LO phonon modes. The thick dashed line and wave line on the left hand side represent the full TA and LO phonon propagator respectively at the presence of interaction. The thin dashed line and wave line on the right hand side represent the free TA and LO phonon propagator respectively. The solid line of the bubble represents the electron propagator with respect to the Luttinger liquid Hamiltonian Eq.(2.20). 22

3.1 (Color online) Schematic representation of the device. A carbon nanotube (CNT) connected to two metal leads is subjected to ac-electric field. 30

3.2 Dependence of the scaling function in the static limit, $F_u(0, x)$ on the doping parameter $x = \frac{k_F v_F}{T}$ for $K_{c+} = 0.2$ (solid line) and $K_{c+} = 0$ (dashed line). 39

4.1 (a) Electron spectrum near the Dirac points $\alpha = \pm 1$ (+ or − indicates parity). (b) Near $x = 0$ the gate potential is $U(x) \approx -eEx$ and saturates to $\pm U_0$ in the p- and n- regions. (c) Schematic picture of the conductance dependence on E at different temperatures. The $G(E)$ curves at different temperatures intersect at the fixed point and increase monotonically with E. The step in $G(E)$ at $T = 0$, indicates a quantum phase transition. (d) RG flow for the conductance. 49

5.1 Schematic picture of the device. The atoms in the wire are labeled by $n = 1, 2, \ldots$. The unit vectors of the graphene Bravais lattice, $\mathbf{a}_1$ and $\mathbf{a}_2$, are shown by blue arrows. Each unit cell (dashed rhomboid) is labeled by (N_1, N_2). 67

5.2 Dependence of the transmission coefficient $\mathcal{T}$ in Eq. (5.38) on ϵ/ϵ_0 (dashed line) with $N = 10$ and $\alpha \sim 1$. The solid curve is the Breit-Wigner resonance with the same resonance energy ϵ_0 and width. . . 69

5.3 An infinite graphene plane is separated into two halves by adding the perturbation $\hat{V}_g$, which nullifies the tunneling along the dashed bonds. 76

5.4 The solid curve represents the intersection of the bulk state spectrum of graphene with the $K_1 = 2\pi/3$ plane that goes through the Dirac point. The dashed curve represents the spectrum of the edge states, which exist only for $2\pi/3 < K_2 < \pi$. The edge state spectrum lies below the bulk state spectrum. 79

ACKNOWLEDGMENTS

The six years of doctoral program is not an easy journey for me so it's especially important to express my gratitude to those who have supported me and helped me during the past six years at this moment.

First I want to express my deepest appreciation to my advisor Anton Andreev. When I first stopped by his office, I had no idea whether I would be able to do theory or not. I only knew that I like theory and wanted to have a try. Anton's patience and trust encouraged me a lot and I made progress rapidly. In the following years, I was constantly impressed by his knowledge and the genuine attitude to physics. I believe all these will have a valuable and long lasting effect on me and my career.

I am also grateful to my collaborators during the program, Professor Leonid Glazman from Yale University, Professor Dror Orgad from the Hebrew University of Jerusalem and Professor Alexie Tsvelik from Brookhaven national lab. They brought me to a broad world of physics and a deep level of thinking and understanding.

Other fellows in condensed matter physics in the department also form an important part of my memory during the past years. I appreciate Dave as my first advisor in my first two years and his care and patience during the time. Even after I left the lab, he was still quite warm hearted and ready to help . Marcel is always very nice and gave me a lot of advice on preparing for the dissertation and graduation. I also want to thank all the graduate students in condensed matter physics. Particulary I want to thank Greg for helping me get through a lot of difficult times in life, and Dima for advices and help on a lot of things, from computer problems to job hunting, and Ahmet for proofreading my dissertation. I also want to thank the two guys, Jiang and Zenghui in Dave's lab for a lot of help in my everyday life. The two close

female friends, Ludan and Esmeralda in the department also help me a lot in easing my mind.

I also want to express my special thanks to Margy, Robin and Bill, for their warm hearts, generosity, wisdom and numerous happy time we spent together in hiking, skiing and parties. My roommate Mengxi has been a great joy and faithful friend in my life since we became roommates. I wish her good luck in the rest of her study in UW.

At last, I want to thank my family in China, especially my three older sisters. Particulary, I want to thank my oldest sister Binbin for her words with wisdom which always help me ease my mind and my second sister Fangfang for always trying her best to help me and being with me during all the tough times and my youngest sister Lili for the unconditional support and acceptance all the time.

Chapter 1

INTRODUCTION

The main subject of this dissertation is the electronic and transport properties in low dimensional interacting systems, particularly in carbon systems. In the 2D and 3D case, the interacting Fermi systems can be described by Landau's Fermi liquid theory, which states that the properties of an interacting system remain essentially similar to those of free fermionic particles, although the elementary particles now are not the individual electrons anymore but electrons dressed by the density fluctuations around them, namely quasiparticles. The situation is drastically different for 1D system. In the 1D case, the Fermi liquid theory breaks down. An electron that tries to propagate has to push its neighbors because of e-e interactions. For that reason, no individual motion is possible and all excitations become collective and Bosonic, which is the physical foundation of the Bosonization method in 1D system. Most of this dissertation will be using the Bosonization method to study 1D interacting systems, particularly carbon nanotubes, so I will first give an introduction of Bosonization and the Luttinger liquid theory in this chapter, and in the second section I will have an overview of the dissertation.

1.1 Bosonization and Luttinger liquid theory

The peculiarity of the particle-hole spectrum in 1D inspired the Bosonization method, which is one of the most useful tools to tackle 1D interacting system. In contrast to high dimensions, when one excites an electron in 1D with momentum k below the Fermi level to above the Fermi level with momentum k+q, the particle-hole excitation or density wave fluctuation has both fixed energy and momentum with linear disper-

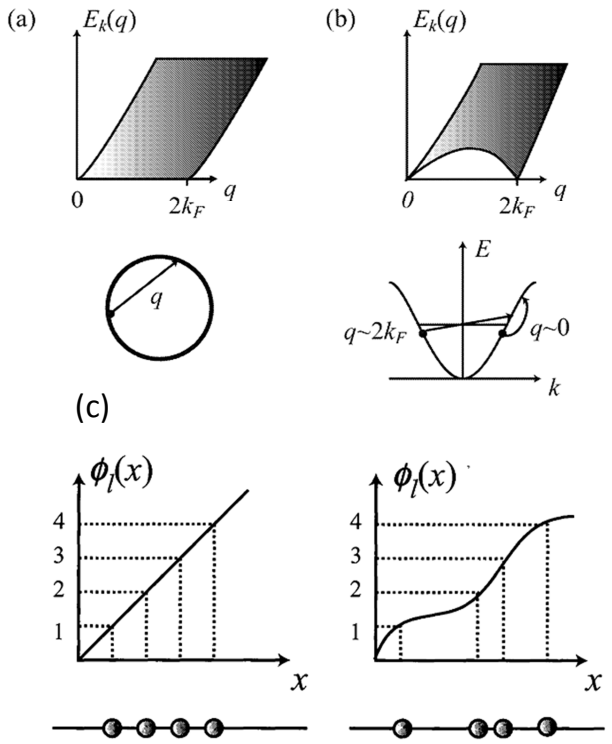

Figure 1.1: (a)schematic picture of electron hole excitation spectrum of 2D and 3D systems. (b) Electron hole excitation spectrum of 1D system. The spectrum has a well defined dispersion relation at small q. (c)A schematic picture of the displacement field ϕ as a function of position.

sion relation $\omega = v_F \mid q \mid$ when q is small, as shown in Fig.1. This linear dispersion relation is identical to that for phonons in one dimension. As an analog to phonon, we can then introduce a displacement field ϕ to describe this linearly dispersing density wave fluctuation $\tilde{\rho} = \partial_x \phi(x)/\pi$, [1] while the full electron density takes the form $\rho(x) = (k_F + \partial_x \phi)/\pi$ and $k_F/\pi \equiv \rho_0$ is the mean electron density which is canceled by the positive background charge.

To get a full mapping from the single particle Fermionic field $\psi(x)$ to the Bosonic fields, one can consider the Jordan-Wigner transformation on a 1D lattice $\psi_j = \exp(i\pi m \Sigma_{i<j} n_i) b_j$ where b_j is a Bosonic field and takes the form $b_j = \sqrt{n_j}\exp(i\theta_j)$, $\exp(i\pi m \Sigma_{i<j} n_i)$ is a string attached to satisfy the Fermionic commutation relations and m is an odd integer. In the continuum limit, i.e., when the scales considered are long compared to the lattice spacing, we replace n_j by $\rho(x)$ and θ_j by $\theta(x)$. As usual, the density and phase satisfy the commutation relation:

$$[\tilde{\rho}(x), \theta(x')] = i\delta(x - x') \tag{1.1}$$

which is equivalent to taking

$$[\phi(x), \theta(x')] = \frac{i\pi}{2} sgn(x - x') \tag{1.2}$$

so the canonical conjugate momentum of $\phi(x)$ is just $\partial_x \theta(x)$ and the same is true with ϕ and θ exchanged.

The Fermionic operator then has a general form

$$\psi(x) \sim \Sigma_{m_{odd}} e^{im(k_F x + \phi)} e^{i\theta(x)} \tag{1.3}$$

The $m = \pm 1$ terms correspond to the left and right moving pieces and describe the slowly varing modes of the electron field. In the low energy regime or continuum limit, the higher harmonics are usually less relevant and the average over them in a scale larger than lattice spacing vanishes so we ignore them. In some special cases, the higher harmonics could become relevant, but we will mention them only when we

encounter this situation. In most of the cases in this dissertation, only the $m = \pm 1$ terms are important and included. The electron field operator containing only these two pieces is

$$\psi(x) = \psi_R + \psi_L = e^{ik_F x} e^{i\Phi_R} + e^{-ik_F x} e^{-i\Phi_L} \tag{1.4}$$

where $\Phi_{R/L} \equiv \phi \pm \theta$. These two fields commute with each other and satisfy

$$[\Phi_R(x), \Phi_R(x')] = -[\Phi_L(x), \Phi_L(x')] = i\pi sgn(x - x') \tag{1.5}$$

The right and left moving electron densities are

$$\rho_{R,L} = \frac{1}{2\pi} \partial_x \Phi_{R,L} \tag{1.6}$$

And the total charge density is

$$\rho = \rho_R + \rho_L + 2k_F \text{ component} \tag{1.7}$$

ρ_R and ρ_L correspond to charge excitation close to the right and left Fermi point respectively, while the $2k_F$ component corresponds to excitation from the left side to right side near the Fermi surface or vice versa. In the continuum limit, the average of the $2k_F$ component over distance larger than lattice spacing vanishes and the smeared density is $\rho = \rho_R + \rho_L = \partial_x \phi / \pi$.

The Hamiltonian of the non-interacting system resembles that of a 1D density wave, which includes the kinetic energy and elastic energy and can be written as

$$H = \frac{v_F}{2\pi} \int dx [g(\partial_x \theta)^2 + \frac{1}{g} (\partial_x \phi)^2] \tag{1.8}$$

where $g = 1$ in the noninteracting case and is renormalized under e-e interaction. The equation of motion of the Bosonic fields at $g = 1$ satisfy

$$\frac{\partial \rho_{R,L}}{\partial t} = i[H, \rho_{R,L}] = \mp v_F \partial_x \rho_{R,L} \tag{1.9}$$

Thus the densities $\rho_{R,L}$ and the fields $\phi_{R,L}$ are only functions of $x - ut$ and $x + ut$. These fields describe excitations that propagate only in the right and left direction

respectively. For that reason, they are called chiral fields. In presence of interaction, the left and right Fermions interact, but one can still find an excitation (that contains both right and left Fermions) that propagates solely to the right or to the left.

It's worth mentioning that the Fermionic field containing only the $m = \pm 1$ terms is an exact mapping from Fermionic fields to Bosonic fields for linear electron spectrum. In the low energy limit, only excitation near the Fermi surface is possible and in this narrow regime of excitation, the spectrum is approximately linear, so in low energy case we can write

$$\psi(x) = \Sigma_{r=\pm 1}\psi_r(x), \text{ and } \psi_r(x) \sim e^{irk_F x}e^{i(r\phi(x)+\theta(x))} \tag{1.10}$$

where $r = \pm 1$ represents right and left mode. This is the mapping we will use extensively in this dissertation.

Another important point we need to note is that since we are only interested in the density wave excitation with respect to the ground state, we should exclude the infinitely occupied Fermi sea in ground state when defining the density operator. To do so, one introduces the normal ordering of a product of operators :ABC:. In a normal ordered product the destruction operators (with respect to a given vacuum) are put on the right and creation operators on the left. For two operators that are linear combinations of creation and destruction operators the normal ordering is equivalent to subtracting the average value in the vacuum : $AB := AB - < 0 \mid AB \mid 0 >$. In the Bosonic form, the normal ordered product of two exponential operators satisfies the relation

$$: e^{i\alpha\phi_r(x)} :: e^{i\beta\phi_r(x')} := (x - x')^{\alpha\beta} : e^{ir(\alpha\phi_r(x)+i\beta\phi_r(x'))} : \tag{1.11}$$

The normal ordering symbol on the right hand side means omitting the contractions between x and x'. For the density operator, we then have

$$\begin{aligned} \psi_r^\dagger(x)\psi_r(x') &= \frac{1}{2\pi}(x - x')^{-1} : e^{i(-\Phi_r(x)+\Phi_r(x'))} : \\ &= \frac{1}{2\pi(x - x')} + \frac{1}{2\pi}i\partial_x\Phi_r(x) + O(x - x') \end{aligned} \tag{1.12}$$

Omitting the singular term when $x = x'$, which is equivalent to excluding the infinite Fermi sea, the density operator is obtained as $\rho(x) = \rho_R(x) + \rho_L(x) = \partial_x\phi(x)/\pi$.

We have already shown that the noninteracting Hamiltonian has a nice quadratic form in Bosonic language. Next let's check the e-e interaction. The Coulomb interaction has the form

$$H_{int} = \int dx V(x - x')\rho(x)\rho(x') \tag{1.13}$$

The density operator is given in Eq.(1.7). We can see that the interaction can be classified by two kinds of processes: forward scattering processes which are quadratic in the Bosonic fields and backward scatterings which have an exponential form of the Bosonic fields. The quadratic part only renormalizes the velocity of the spectrum but will not change it qualitatively, yet the backscattering processes may open a gap and destroy the non interacting ground state, which we will investigate in more detail in the following chapters.

1.2 Overview of the dissertation

A major part of this dissertation will be applying the Bosonization method to study the interaction effects in 1D systems, specifically CNTs, including the effects on the ground state spectrum and transport properties. A minor part of the dissertation will be transport through a molecular wire connected to 2D graphene leads.

In Chapter 2, we will apply Bosonization to study how interactions, namely e-e interactions and e-phonon interactions, change the non-interacting ground state of a single metallic armchair CNT as well as the interplay between these interactions in determining the ground state. The non interacting spectrum of armchair CNT is predicted to resemble a linear gapless Dirac spectrum from the tight binding model. The effect of e-phonon interaction in CNTs without taking into account e-e correlation had been studied in Fermionic language by previous workers, and a twist instability accompanied by a metal insulator transition occurring at very low temperature (less than 0.1 K) was predicted. Our work revealed that the e-e correlation greatly

enhances the transition temperature T_c (by more than two orders of magnitude) to an experimentally easily accessible region. We also showed that the e-e correlation changes the T_c dependence on e-phonon coupling strength from an exponential law to a power law. Yet the e-phonon interaction is not the only interaction that results in an insulator of a CNT at low temperature. The e-e Umklapp processes were also shown to turn the CNT into a Mott insulator at low temperature. The interplay of these two interactions was then studied and we found that the e-phonon processes and e-e Umklapp processes compete in determinating the ground state of a CNT. In wide CNTs, the competition results in a Mott insulator while in very narrow CNTs, the competition may result in a Peierls insulator with twisted lattice at low temperature.

In chapter 3 the plasmon decay in CNTs due to e-e and e-phonon interactions is studied and related to the electron transport properties in a two terminal device. In a pure Luttinger liquid, the Bosonic modes don't decay because they are eigenmodes of the Hamiltonian and there is no dissipation. Yet with backscattering, the Bosonic modes gain a finite lifetime and the transport through the Luttinger liquid becomes dissipative. In armchair CNTs, there are four Bosonic modes: the plasmon mode which carries charge, and three neutral modes. The e-e and e-phonon back scatterings cause the plasmon mode to decay into neutral modes or Phonon modes. This mechanism leads to a correction to the otherwise perfect conductance quanta in a two terminal CNT device. The intrinsic energy dissipation rate in CNTs is proportional to the plasmon decay rate. The latter is related to the ac conductivity of a homogenous CNT through a Drude-like formula. In a real two terminal device, when $L \gg L_T \equiv v_F/T$, the boundary is not important and the tube can be considered to be homogeneous and this is the case we are interested in. In the case $L \ll v_F/\Delta_u$, either for an undoped tube or doped one, the tube remains metallic and the decay rate is small so it can be computed perturbatively.

In chapter 4, we study the electron transport through an armchair CNT pn junction, which reveals an unusual quantum critical phenomenon in such a structure. The

pn junction can be formed experimentally by applying a nonuniform doping potential through two gates. Again the back scatterings, e-e Umklapp processes and e-phonon back scatterings make corrections to the otherwise perfect conductance quanta. The Umklapp processes take place only at the center region of the junction due to momentum conservation, which makes the pn junction resemble a single barrier. Yet in contrast to single barrier scattering in Luttinger liquids, which is always relevant and results in an insulator at low temperature at any strength of the barrier or electron repulsion, the relevance of the e-e Umklapp backscattering in the CNT pn junction can be tuned by the doping electric field. At zero temperature, the pn junction can go through a quantum phase transition from insulator to perfect conductor controlled by the built-in doping field. This also indicates an unstable intermediate fixed point of conductance. The finite temperature conductance at the two limits of weak back scatterings and weak tunneling are obtained by perturbation theory, while the behavior at the fixed point is studied from the RG equations using an epsilon expansion near the marginal point.

In Chapter 5, we switch gears to study the transport through a device consisting of a molecular wire connected to two graphene leads. One such device achieved in experiments is a full carbon device consisting of two graphene leads connected by a single-atom carbon chain. As an initial step, we ignore the e-e interaction which is not so important in a short wire and in a 2D system. Using the Greens function method, we obtained the spectrum of the bulk states as well as the edge states in the graphene leads. From Fermi's golden rule, the tunneling coefficient through one junction can be estimated as $T \sim \mid \gamma \mid^2 \nu_w \nu_g$, where γ is the tunneling matrix through the lead and wire, ν_w and ν_g are the local density of states (DOS) of the wire and graphene lead at the connecting points respectively. The local DOS of the wire is a constant yet the local DOS of the graphene lead at the connecting point, either coming from the bulk states or the edge states, is linear in the energy counted from the Dirac point. Thus the tunneling coefficient through one junction vanishes linearly with the

energy at small doping even if the coupling between the wire and graphene lead is strong. The whole device acts as a Fabry-Perot interferometer and the transmission through the whole device has a very sharp resonance feature with energy due to the strong reflection at the junction. This feature is common for molecular devices with graphene leads only if the electron states in the molecule or wire are extended through the whole molecule or wire. The resonance feature of the transmission makes such devices different from devices with normal metallic leads and being candidates for atom scale transistors.

The details of most of the work above can be obtained from the following papers:

1. Twist instability in strongly correlated carbon nanotubes

Wei Chen, A. V. Andreev, A. Tsvelik, D. Orgad, Phys. Rev. Lett. 101, 246802(2008)

2. Decay of a plasmon into neutral modes in carbon nanotube

Wei Chen, A.V. Andreev, E.G. Mishchenko, L.I.Glazman, Phys. Rev. B 82, 115444(2010)

3. Quantum criticality in a Mott pn junction in an armchair carbon nanotube

Wei Chen, A.V. Andreev, L.I.Glazman, Phys. Rev. Lett. 106, 216801(2011)

4. Conductance of a single atom carbon chain with graphene leads

Wei Chen, A.V. Andreev, G. Bertsch, Phys. Rev. B 80, 085410(2009)

Chapter 2

ELECTRON STRUCTURE IN A STRONGLY CORRELATED ARMCHAIR CNT

2.1 Introduction

In this chapter, we study the interaction effects on the electron structure in armchair carbon nanotubes (CNT). The non-interacting ground state of an armchair carbon nanotube is nominally metallic with gapless Dirac spectrum by the zone folding of the spectrum of graphene from the tight binding model.[2] Yet under interaction, this image may be destroyed. Experiments reveal that all CNTs are actually gapped at low temerature.[3] The origin of the gap could come from both the e-phonon interaction and e-e interaction. The former can induce the Peierls transition and the latter induce the Mott transition. Both transitions result in a gap in the electron spectrum. In this chapter we examine both interactions in CNTs under the Luttinger liquid theory frame and discuss their interplay as well.

It's well known that in a single band 1D system, the response function with wave vector $2k_F$ diverges and leads to various instabilities at low temperature. The response of an electron gas to e-phonon interaction results in a charge density wave ground state consisting of a periodic charge density modulation accompanied by a periodic lattice distortion, both periods with wavelength $\lambda_0 = \pi/k_F$. Consequently both the electron and phonon spectra are strongly modified by the formation of the charge density waves. Generally the phonon spectrum is strongly renormalized near $2k_F$, referred to as the Kohn anomaly. At a finite temperature $\omega_{ren,2k_F} \to 0$ indicating a phase transition, known as the Peierls transition. For a partially filled electron band, the period λ_0 is incommensurate with the underlying lattice. The periodically varying

lattice distortion leads in turn to a single particle gap at the Fermi level, turning the material into an insulator. [4] Meanwhile, e-e Coulomb interaction may also change the electron band structure due to the repulsion between electrons and result in a Mott transition. As a result, the electron spectrum develops a gap.

The Mott transition in armchair carbon nanotubes has been studied by previous workers in the Luttinger liquid theory framework.[15, 16] The e-e Umklapp interaction turns an armchair CNT into a Mott insulator. The gap was estimated in different ways. The Peierls transition in armchair carbon nanotubes was also studied by previous workers, but in the non-interacting picture. A twist instability happens at wave vector $q = 0$ instead of $2k_F$ and as a result, instead of a periodic lattice distortion with wavelength π/k_F at low temperature, the carbon nanotube lattice develops a twist in the circumferential direction with a long wavelength and the electron spectrum develops a Peierls gap.

In this chapter we study the Peierls transition in armchair CNTs within the Luttinger liquid theory frame, i.e., taking into account e-e interaction. We found that the e-e interaction strongly enhances the Pierls transition temperature T_c and changes the T_c dependence on the e-phonon coupling strength from an exponential law to a power law. We also estimate the Pierls gap and twist angle upon transition by a mean field variational method which is valid in the ordered state.

To determine the ground state of the CNT in the presence of both e-e interaction and e-phonon interaction, we studied the interplay of the two interactions and found that they compete with each other and only one transition can happen at one time. Which one wins depends on the condensation energy upon the transition, which in turn is determined by the energy gap developed. The possible ground state in a realistic CNT is discussed at the end.

This chapter is organized as follows: In Sec.2.2, we present the noninteracting spectrum of carbon nanotubes under tight binding approximation. In Sec.2.3, we study the Luttinger liquid theory in armchair CNT and the Mott transition due to

e-e Umklapp interaction. In Sec.2.4, we study the Peierls transition in the armchair CNT in the Luttinger liquid theory frame. In Sec.2.5, we study the interplay between the Mott transition and Peierls transition and discuss the ground state of an armchair CNT under both e-e interaction and e-phonon interaction.

2.2 Non-interacting spectrum of carbon nanotubes

The non interacting spectrum of carbon nanotube can be obtained by zone folding of the spectrum of graphene from the tight binding model. Consider a graphene sheet as shown in Fig.2.1(a). The sp^2 hybridized orbits form 3 binding orbits and 3 anti binding orbits. The 3 binding orbits are fully occupied yet the 3 anti-binding orbits are empty. The remaining p_z orbit is perpendicular to the graphene plane and forms a conducting band. Since there are two atoms in each unit cell, two conducting bands are formed from the combination of the two p_z orbits of two sublattices. In this section we present the tight binding approximation approach to the spectrum of these two bands. [5]

The Bloch wave functions of the two sublattices of the graphene in the tight binding model are written as

$$\psi_A = \frac{1}{\sqrt{N}} \sum_A e^{i\vec{k}\cdot\vec{R}_A} \phi(\overrightarrow{r} - \overrightarrow{R}_A); \quad \psi_B = \frac{1}{\sqrt{N}} \sum_B e^{i\vec{k}\cdot\vec{R}_B} \phi(\overrightarrow{r} - \overrightarrow{R}_B) \tag{2.1}$$

where $\phi(\overrightarrow{r} - \overrightarrow{R}_A)$ and $\phi(\overrightarrow{r} - \overrightarrow{R}_B)$ are the local wave functions for an isolated A and B atom respectively. The electron wave function in the graphene has the form $\psi = \psi_A + \lambda\psi_B$. The energy satisfies the equation

$$H\psi = E\psi \tag{2.2}$$

where the Hamiltonian H includes the kinetic energy of the electron and the periodic potential experienced by the electron from the lattice. The spectrum can be solved by the secular equation

$$\begin{vmatrix} H_{AA} - E & H_{AB} \\ H_{BA} & H_{BB} - E \end{vmatrix} = 0 \tag{2.3}$$

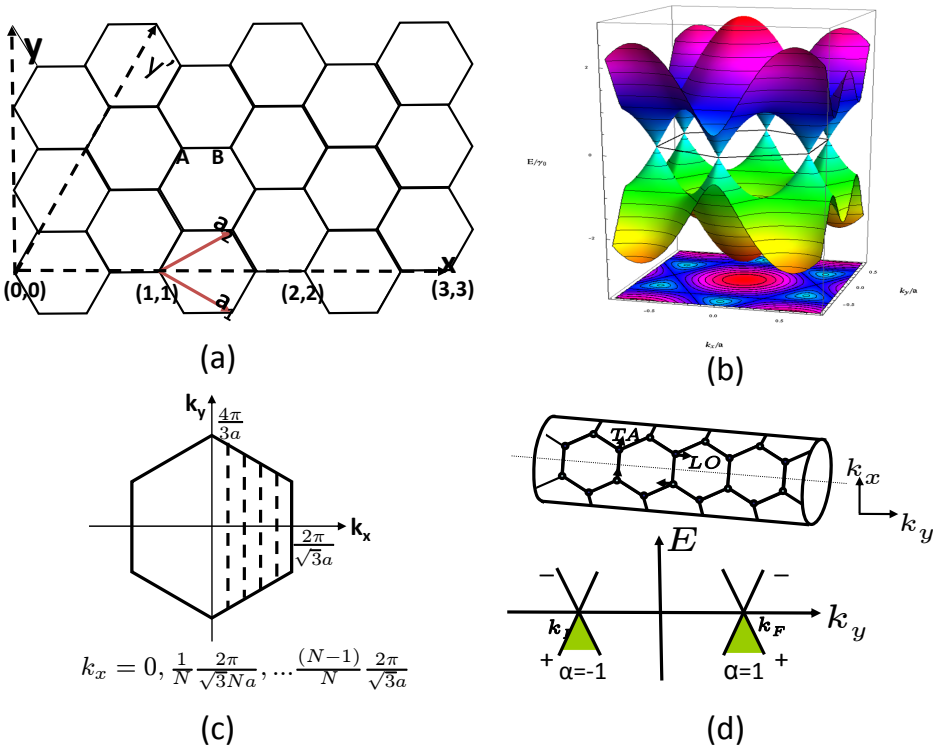

Figure 2.1: (a) Schematic picture of a graphene sheet. (b) 2D electron spectrum of a graphene sheet. (c)Reciprocal lattice of the graphene sheet in (a). (d)Schematic picture of an armchair carbon nanotube and its non interacting electron spectrum. Green and blue circles denote atoms in the A and B sublattices. The arrows show atomic displacements in the TA and LO phonon modes. + and − denote the parity of the bands. $\alpha = \pm 1$ corresponds to the two valleys with Fermi points at $\pm k_F$.

where $H_{AA} = \langle \psi_A \mid H \mid \psi_A \rangle$, $H_{AB} = \langle \psi_A \mid H \mid \psi_B \rangle$, and similarly for H_{BB} and H_{BA}. Assuming there is no overlapping between $\phi(\overrightarrow{r} - \overrightarrow{R}_A)$ and $\phi(\overrightarrow{r} - \overrightarrow{R}_B)$, i.e., $\int \phi(\overrightarrow{r} - \overrightarrow{R}_A)\phi(\overrightarrow{r} - \overrightarrow{R}_B)dr = 0$, one gets

$$\begin{aligned} H_{AA} &= \frac{1}{N} \sum_{R_A, R_{A'}} e^{i\overrightarrow{k}\cdot(\overrightarrow{R}_A - \overrightarrow{R}_{A'})} \int \phi^*(\overrightarrow{r} - \overrightarrow{R}_{A'}) H \phi(\overrightarrow{r} - \overrightarrow{R}_A) dr \\ H_{AB} &= \frac{1}{N} \sum_{R_A, R_B} e^{i\overrightarrow{k}\cdot(\overrightarrow{R}_B - \overrightarrow{R}_A)} \int \phi^*(\overrightarrow{r} - \overrightarrow{R}_A) H \phi(\overrightarrow{r} - \overrightarrow{R}_B) dr \end{aligned} \tag{2.4}$$

Assuming $\int \phi^*(\overrightarrow{r} - \overrightarrow{R}_{A'}) H \phi(\overrightarrow{r} - \overrightarrow{R}_A) dr = \varepsilon_0$ is non vanishing only for $A = A'$, and that $\int \phi^*(\overrightarrow{r} - \overrightarrow{R}_A) H \phi(\overrightarrow{r} - \overrightarrow{R}_B) dr = t$ is nonvanishing only for nearest neighbor atom A and B, we obtain the equation

$$\begin{vmatrix} \varepsilon_0 - E & t \sum_{n.n} e^{i\overrightarrow{k}\cdot\overrightarrow{R}_{AB}} \\ t^* \sum_{n.n} e^{-i\overrightarrow{k}\cdot\overrightarrow{R}_{AB}} & \varepsilon_0 - E \end{vmatrix} = 0 \tag{2.5}$$

where the sum is only over the three nearest neighbor B atoms of A or vice versa. The spectrum is thus obtained as

$$E = \varepsilon_0 \pm |t| \sqrt{1 + 4\cos^2 \frac{k_y a}{2} + 4\cos \frac{k_y a}{2} \cos \frac{\sqrt{3} k_x a}{2}} \tag{2.6}$$

Setting $\varepsilon_0 = 0$, i.e., the energy is counted from the center of the band, one gets the spectrum of graphene as shown in Fig.2.1(b).

Carbon nanotubes can be considered as a rolled sheet of graphene and have different chirality when rolled in different directions. The momentum in the circumferential direction is quantized as $k_y = 2\pi m/R$ to satisfy the periodic boundary condition, where m is a non negative integer. The spectrum of a carbon nanotube contains a series of 1D bands cut by the quantized k_y from the 2D graphene spectrum. The nanotubes are gapless and metallic if the $k_y = m/R$ plane crosses one of the Dirac points. Otherwise, they are semiconducting with a gap. At room temperature, only the lowest band is excited and carbon nanotube can be considered as a 1D wire. In this dissertation, we are most interested in the armchair carbon nanotubes, which

are tubes rolled along the (N, N) direction. The momentum in the circumferential direction has quantized values $k_y = \frac{2\pi}{N\sqrt{3}a}m$ with $m = 1, 2, ..., N-1, N$ which cut the reciprocal lattice of graphene as in Fig.2.1(c). The lowest two bands correspond to $k_y = \frac{2\pi}{\sqrt{3}a}$ and have spectrum

$$E_{\pm} = \mp|t|[1 - 2\cos(k_x a/2)] \tag{2.7}$$

From here on, we drop the | on t and by default t means $|t|$ and represents the nearest neighbor hopping integral. The two bands cross each other at the Dirac points as shown in Fig.2.1(d). The armchair CNT has a symmetry plane that goes through the tube axis and maps the A and B sublattices to each other. The electron spectrum and the phonon modes are both characterized by the parity ± 1 due to this symmetry.

2.3 Luttinger liquid theory and Mott transition in the CNT

The low energy electron bands of an armchair CNT form two pairs of spin-degenerate right and left branches intersecting at the band center, which also locates the two Fermi points. At low energy only the modes near the Fermi surface are important and the electron field operator can be written as

$$\Psi_\sigma(x) = \sum_{\alpha r} e^{i\alpha k_F x}\psi_{\alpha r\sigma} \tag{2.8}$$

where $\alpha = 1, 2$ represent the two valleys, $r = \pm 1$ represent the left and right movers respectively, and $\sigma = \pm 1$ represent the two spin modes. The electron operator can also be expanded in terms of the Bloch waves of the two sublattices $p = \pm 1$,

$$\Psi_\sigma(x, y) = \sum_{\alpha r} e^{i\alpha k_F x}\psi_{\alpha r\sigma} = \sum_{p\alpha} \varphi_{p\alpha}(x, y)\psi_{p,\alpha,\sigma}(x) \tag{2.9}$$

with the phase factor $\varphi_{p\alpha}(x, y) = \frac{e^{-i\alpha k_F x}}{\sqrt{2\pi\xi}}$. The field operator on the two sublattices can be transformed to the basis of left and right movers by the unitary transformation $\psi_{p\alpha\sigma} = \frac{1}{\sqrt{2}}\sum_{r=\pm}(r\alpha)^{(1-p)/2}\psi_{\alpha r\sigma}$.

Near the Fermi surface, the spectrum can be linearized and the low energy free Hamiltonian can be written as

$$H_{0e} = i\hbar v_F \sum_{\alpha,r,\sigma} \int dx \psi^{+}_{\alpha,r,\sigma} \sigma_3 \partial_x \psi_{\alpha,r,\sigma} \tag{2.10}$$

The e-e interaction contains forward and backward scattering terms. At low energy, only scatterings with $q \sim 0$ and $q \sim 2k_F$ are important. The interaction Hamiltonian can be written as

$$H_{int} = \frac{1}{2} \sum_{pp'\sigma\sigma'} \sum_{\alpha_1\alpha_2\alpha_3\alpha_4} \int dx dx' \psi^{\dagger}_{p\alpha_1\sigma}(x) \psi^{\dagger}_{p'\alpha_2\sigma'}(x') V^{pp'}_{\alpha_i}(x-x') \psi_{p'\alpha_3\sigma'}(x') \psi_{p\alpha_4\sigma}(x) \tag{2.11}$$

where $p = \pm 1$ labels two sublattices and $\psi_{p,\alpha,\sigma}(x)$ is the field operator on sublattice p. The 1D potential

$$V^{pp'}_{\alpha_i}(x-x') = \int_0^{2\pi R} dy dy' \varphi^{*}_{p\alpha_1}(x,y) \varphi^{*}_{p'\alpha_2}(x',y') U(x-x', y-y'+pd\delta_{p,-p'}) \varphi_{p',\alpha_3}(x',y') \varphi_{p,\alpha_4}(x,y) \tag{2.12}$$

where $U(x-x', y-y')$ is the Coulomb potential, d is the shift between the two sublattices.

The terms with $\alpha_1 = \alpha_4$ and $\alpha_2 = \alpha_3$ but $\alpha_1 \neq \alpha_2$ correspond to forward scatterings and the ones with $\alpha_1 = -\alpha_2 = \alpha_3 = -\alpha_4$ correspond to back scattering. For undoped tubes, there are Umklapp processes too, corresponding to $\alpha_1 = \alpha_2 = -\alpha_3 = -\alpha_4$.

The forward scattering Hamiltonian can then be written as

$$H_{FS} = \frac{1}{2} \int dx dx' \rho(x) V_0(x-x') \rho(x') \tag{2.13}$$

where

$$V_0(x) = \int_0^{2\pi R} \frac{dy}{2\pi R} \int_0^{2\pi R} \frac{dy'}{2\pi R} U(x, y-y') \tag{2.14}$$

and $\rho(x) = \sum_{p\alpha\sigma} \psi^{\dagger}_{p\alpha\sigma} \psi_{p\alpha\sigma}$ varies slowly in space and doesn't distinguish lattice so we can write

$$H_{FS} = V_0(k=0) \int dx \rho(x) \rho(x) \tag{2.15}$$

For unscreened Coulomb interaction $U(x,y) = \frac{e^2}{\kappa\sqrt{a_0^2+x^2+4R^2\sin^2(y/2R)}}$. $V_0(k)$ for $kR \ll 1$ is reminiscent of a 1D quantum wire and $V_0(k) = (e^2/\kappa)[2|\ln(kR)| + \pi\ln 2]$. The lower cutoff of k is $1/L$ with L the length of the tube and the upper cutoff of k is $1/R$. There is another forward scattering term due to the short range ($r \leq a$) Coulomb interaction, but the interaction strength $\sim e^2/R$ is much less than $V_0(k = 0) = (e^2/\kappa)[2|\ln(R/L)| + \pi\ln 2]$ and this term can be combined to the long range forward scattering.

The backscattering term contains intra lattice ($p = p'$) and inter lattice ($p = -p'$) interactions. The intrasublattice backscattering strength $V_{pp}(2k_F)$ is estimated to be of order $\sim ae^2/R$ where a is the nearest bond length. The inter lattice interaction is much less than the intra lattice interaction due to the C_3 symmetry of the graphene sheet which leads to the vanishing of $V_{p,-p}(2k_F)$ for a plane graphite sheet.

The above Hamiltonians can be bosonized by writing

$$\psi_{\alpha,r,\sigma}(x) = \frac{F_{\alpha\sigma}}{\sqrt{2\pi\xi}} exp[i(\Theta_{\alpha\sigma} + r\Phi_{\alpha\sigma})] \tag{2.16}$$

Here $F_{\alpha\sigma}$ are the Klein factors, $1/\xi$ is an upper momentum cutoff and ξ is the radius of the nanotube. [24] The boson operators in the exponential satisfy the following equal time commutation relations

$$[\Phi_{\alpha\sigma}(x), \Theta_{\alpha'\sigma'}(x')] = i\delta_{\alpha\alpha'}\delta_{\sigma\sigma'}\theta(x - x'), \tag{2.17}$$

with $\theta(x - x')$ being the step function. By introducing the modes combining spins and valleys in different ways as [13]

$$\Phi_{c\pm} = \frac{1}{2}\sum_{\sigma}(\Phi_{1\sigma} \pm \Phi_{2\sigma}), \Phi_{s\pm} = \frac{1}{2}\sum_{\sigma}\sigma(\Phi_{1\sigma} \pm \Phi_{2\sigma}), \tag{2.18}$$

and the corresponding conjugate momentum

$$\Theta_{c\pm} = \frac{1}{2}\sum_{\sigma}(\Theta_{1\sigma} \pm \Theta_{2\sigma}), \Theta_{s\pm} = \frac{1}{2}\sum_{\sigma}(\Theta_{1\sigma} \pm \Theta_{2\sigma}), \tag{2.19}$$

the Luttinger liquid Hamiltonian containing only the free part and forward scattering part can be written as

$$\begin{aligned} H_{0e} &= \tfrac{\hbar}{2\pi} v_F \textstyle\sum_j \int dx[(\nabla\Phi_j)^2 + (\nabla\Theta_j)^2] + V_0(k=0)\int dx(\nabla\Phi_{c+})^2 \\ &= \tfrac{\hbar}{2\pi} u_j \textstyle\sum_j \int dx[K_j(\nabla\Phi_j)^2 + \tfrac{1}{K_j}(\nabla\Theta_j)^2] \end{aligned} \tag{2.20}$$

Here $j = c\pm, s\pm$ labelling the above defined modes. $K_j = 1/\sqrt{1 + 2\pi V_0(k=0)/v_F\hbar}$ for $j = c+$, which is a charged mode and 1 for $j = c-, s\pm$, which are there neutral modes. u_j is the velocity of the j mode and $u_j = v_F/K_j$. It is seen that $K_{c+} \ll 1$ due to strong e-e interaction in carbon nanotube and it is about $\frac{1}{5}$. [] For the same reason, the $c+$ mode is much faster than the other modes.

Collecting all the backscattering terms in Eq.(2.11) and bosonizing them, one finds that the most relevant terms correspond to the so-called Umklapp processes, which transfer two right-moving electrons into left moving ones or vice versa [13, 14, 15, 16]. The bosonized form of the umklapp interaction can be written as [16]

$$\begin{aligned} H_u &= -\frac{1}{2(\pi\xi)^2}\int dx \cos(\sqrt{4\pi}\Phi_{c+}) \\ &\quad \Big\{ g_3 \cos(\sqrt{4\pi}\Theta_{s-}) + (g_3 - g_1)\cos(\sqrt{4\pi}\Phi_{s+}) \\ &\quad + g_1[\cos(\sqrt{4\pi}\Phi_{c-}) - \cos(\sqrt{4\pi}\Phi_{s-})] \Big\}, \end{aligned} \tag{2.21}$$

where the coupling constants originate from the short range part of the Coulomb interaction, V_{AA} and V_{AB}, between electrons on the A and B sublattices. Explicitly, one finds $g_3 = V_{AA}(2k_F) + V_{AB}(2k_F)$ and $g_1 = V_{AA}(0) - V_{AB}(0)$ [15, 16], both $\sim ae^2/R$ where a is the bond length.

The scaling of the Umklapp coupling constant is $1 - K_{c+}$. In the case $K_{c+} \ll 1$, the Umklapp processes are strongly relevant and result in a Mott transition at low temperature accompanied by a gap. The gap could be obtained by the mean field variational method as in Ref.[15]. The gaps obtained in this way are different for the four modes, greatest for the charge mode and proportional to the coupling constant for the neutral modes. Yet they all have the same scaling with respect to the radius

of the tube as $\Delta \sim (\frac{1}{R})^{1+\frac{1}{1-K_{c+}}}$. In the limit of $K_{c+} \to 0$, the charge mode Φ_{c+} is fully pinned and the average $< \cos 2\Phi_{c+} > \sim 1$. In this case we can take the adiabatic limit and integrate out the fast charge mode. The remaining part containing the neutral modes can be refermionized by the mapping [6]

$$\begin{aligned} \psi_R^\dagger \psi_L - \psi_L^\dagger \psi_R &= \frac{i}{\pi\xi} \cos 2\Phi \\ \psi_R^\dagger \psi_L^\dagger - \psi_L \psi_R &= \frac{i}{\pi\xi} \cos 2\Theta \end{aligned} \tag{2.22}$$

The Dirac fermionic fields can be decomposed to Majorana Fermionic operators as

$$\begin{aligned} \psi_{s,R/L} &= \frac{1}{\sqrt{2}}(\chi_{1,R/L} + i\chi_{2,R/L}) \\ \psi_{sf,R/L} &= \frac{1}{\sqrt{2}}(\chi_{3,R/L} + i\chi_{0,R/L}) \\ \psi_{f,R/L} &= \frac{1}{\sqrt{2}}(\eta_{1,R/L} + i\eta_{2,R/L}) \end{aligned} \tag{2.23}$$

and the Umklapp Hamiltonian can then be written as

$$\mathcal{H}_{umkl} = i\frac{1}{\pi\xi}[g_t \sum_{i=1}^{3} \chi_{i,R}\chi_{i,L} + g_0\chi_{0R}\chi_{0L} - g_1 \sum_{i=1}^{2} \eta_{iR}\eta_{iL}] \tag{2.24}$$

where $g_t = g_3 + g_1$, $g_0 = g_1 - g_3$. The Hamiltonian manifests $SU(2)$ symmetry. The triplet of Majorana fermions transforms according to the spin $S = 1$ representation of the $SU(2)$ group and the fermion labeled by $i = 0$ is a singlet under the $SU(2)$. The quadratic part of the Hamiltonian can be written as

$$\mathcal{H}_0 = \mathcal{H}_0[\Phi_{c+}] + \frac{iv}{2}\sum_{i=1}^{2}(-\eta_{i,R}\partial\eta_{i,R} + \eta_{i,L}\partial\eta_{i,L}) + \frac{iv}{2}\sum_{i=0}^{3}(-\chi_{i,R}\partial\chi_{i,R} + \chi_{i,L}\partial\chi_{i,R}) \tag{2.25}$$

The Hamiltonian including the Umklapp interaction is then equivalent to a Hamiltonian of massive Dirac Fermions. The masses of the Dirac Fermions give the gaps of the spectrum, which is

$$M_{c-} = \frac{g_1}{\pi\xi}, \quad M_{s,t} = \frac{g_t}{\pi\xi}, \quad M_{s,s} = \frac{g_0}{\pi\xi} \tag{2.26}$$

These gaps correspond to neutral excitation. The charge gap is

$$\Delta_{c+} = \sqrt{\pi(M_{c-}^2 + 3M_{s,t}^2 + M_{s,s}^2)} \tag{2.27}$$

Since $g_i \sim 1/R$ and $\xi \sim R$, the gap scales as $\Delta \sim 1/R^2$.

2.4 Peierls transition in the armchair CNT in the Luttinger liquid theory framework

In this section we study the Pierls transition in an armchair CNT due to e-phonon interaction.

There are 6 phonon modes in an armchair CNT altogether. Among them, three have positive parity: LA, TO and RA, where L represents longitudinal, T transverse and R radial; and three have negative parity: TA, LO and RO. The positive parity phonon modes cause intraband e-e scattering and the negative phonon modes cause interband e-e scattering. [17] The e-phonon interaction arises from the change of the hopping matrix element induced by the atomic displacement. The coupling of the RO phonon to electron is proportional to the curvature of the tube and is smaller than other couplings by a factor of $1/N$ so we ignore this coupling. [19] By calculation we found that the phonon assisted electron forward scatterings cause only softening of the phonon modes but are not strong enough to result in a Peierls transition so we will not pay much attention to them. The backscattering includes intravalley backscattering with $q = 0$ assisted by TA and LO phonons and intervalley backscattering with $q = 2k_F$ assisted by LA and TO phonons. Since the phonons with wavevector $2k_F$ have much higher frequency $\sim 1000K$ than the $q = 0$ phonons, they are harder to be softened to zero frequency so instability will happen only to $q = 0$ phonons that cause intravalley backscattering, i.e., the Pierls transition will happen only to TA phonons with long wavelength in armchair CNT. Yet we will see that although the LO phonons do not soften to zero frequency, they enhance the twist instability since they lead to the same electron backscattering processes. For this reason we will focus

on the electron interaction with TA and LO phonons, which are schematically shown in Fig.2.1(d).

The classical Hamiltonians of the TA and LO phonon are respectively

$$H_{TA} = \int dx (\frac{\rho}{2}(\partial_t u_T)^2 + \frac{\rho s_T^2}{2}(\partial_x u_T)^2);\ H_{LO} = \int dx \frac{\rho}{2}((\partial_t u_L)^2 + \omega_0^2 (u_L)^2) \quad (2.28)$$

where $u_{T,L}$ is the displacement of atoms relative to equilibrium position, ρ is the linear mass density of the nanotube, s_T is the sound velocity of the TA mode and ω_0 is the LO phonon frequency.

In k space, the LO and TA phonon Hamiltonian can be written in a unified form

$$H_{ph} = \frac{\rho}{2} \sum_{a=L,T} \sum_q \left[|\dot{u}_a(q)|^2 + \omega_a(q)^2 |u_a(q)|^2 \right]. \quad (2.29)$$

The electron-phonon interaction is treated within the tight-binding approximation [26, 27, 17]. The coupling of electrons to the TA and LO phonons is described by the Hamiltonian

$$H_{ep} = \int dx M(x)[g_T \partial_x u_T(x) + g_L u_L(x)], \quad (2.30)$$

with $M(x) = -i \sum_{\alpha r \sigma} \alpha r \psi^\dagger_{\alpha r \sigma}(x) \psi_{\alpha -r \sigma}$. The bosonized form of the operator M is

$$\begin{aligned} M &= -\frac{4}{\pi \xi} \left[\prod_{\nu=\pm} \cos(\sqrt{\pi}\Phi_{c\nu}) \sin(\sqrt{\pi}\Phi_{s\nu}) \right. \\ &\quad \left. + \prod_{\nu=\pm} \sin(\sqrt{\pi}\Phi_{c\nu}) \cos(\sqrt{\pi}\Phi_{s\nu}) \right]. \end{aligned} \quad (2.31)$$

By writing M in this form we adopted the convention $F^\dagger_{\alpha\sigma} F_{\alpha\sigma} = 1$. For $K_{c+} \ll 1$ the e-ph coupling (2.31) leads to a strong renormalization of the twist mode.

The Feynman diagram of the TA and LO phonon propagators is shown in Fig.2.2. The free phonon propagators of unperturbed Hamiltonian can be written in terms of a 2×2 matrix,

$$\mathcal{D}_0(\omega_n, q) = \begin{pmatrix} D_{0,a} & 0 \\ 0 & D_{0,o} \end{pmatrix} \quad (2.32)$$

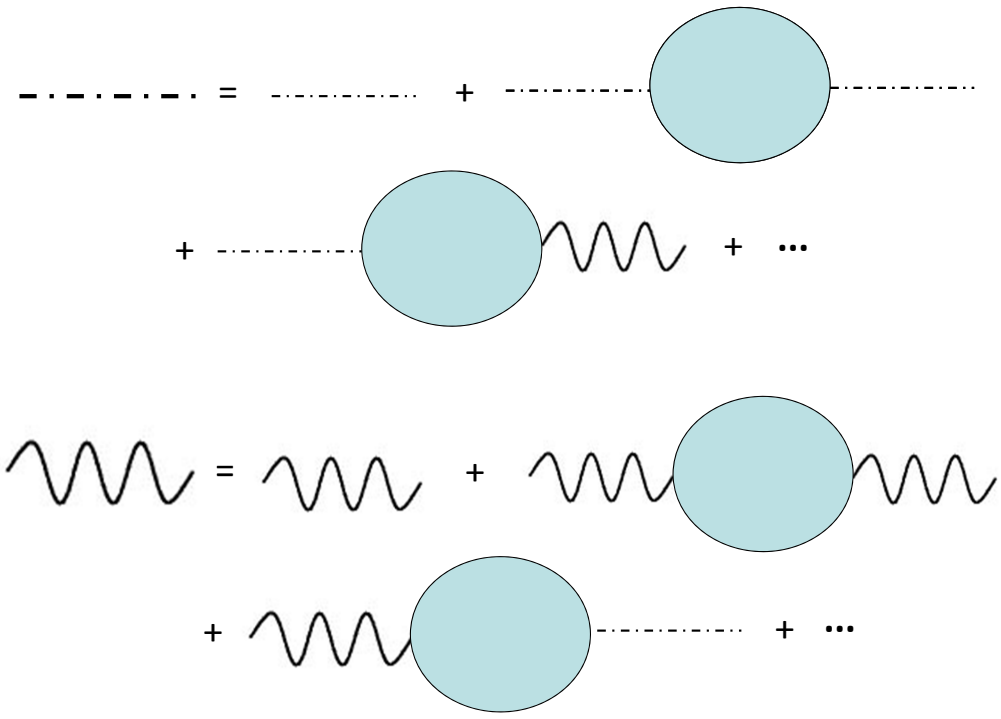

Figure 2.2: Schematic Feynmann diagram of the TA and LO phonon modes. The thick dashed line and wave line on the left hand side represent the full TA and LO phonon propagator respectively at the presence of interaction. The thin dashed line and wave line on the right hand side represent the free TA and LO phonon propagator respectively. The solid line of the bubble represents the electron propagator with respect to the Luttinger liquid Hamiltonian Eq.(2.20).

where $\omega_n = 2n\pi T = 2n\pi/\beta$ is the Matsubara frequency and $\mathcal{D}_{0,a}^{-1}(\omega_n, q) = \delta_{a,a'}\rho[\omega_n^2 + \omega_a^2(q)]$ is shown in Appendix A. The propagation of phonons dressed by the interaction with the electrons is described by the matrix

$$\mathcal{D}(\omega_n, q) = \begin{pmatrix} D_{aa} & D_{ao} \\ D_{oa} & D_{oo} \end{pmatrix} \tag{2.33}$$

It is related to the free phonon propagation matrix $\mathcal{D}_0$ by $\mathcal{D} = \mathcal{D}_0 + \mathcal{D}_0\mathcal{V}\mathcal{D}$, where the interaction process is described in the diagrams in Fig.2.2 and the interaction matrix $\mathcal{V}$ can be written as

$$\mathcal{V} = \begin{pmatrix} g_T g_T^* q^2 & -ig_T g_L^* q \\ ig_L g_T^* q & g_L g_L^* \end{pmatrix} P(\omega_n, q) \tag{2.34}$$

Here $g_{T,L}$ are the e-ph interaction strength at the vortex and $P(\omega_n, q)$ is the electron polarization operator represented by the bubble. To second (lowest) order of the e-phonon interaction, the polarization $P(\omega_n, q) = \int dr e^{i\omega_n\tau - iqx}\langle M(0)M(r)\rangle$ and $\langle \ldots \rangle$ denotes thermal averaging with respect to the Luttinger liquid Hamiltonian (2.20). The phonon propagator matrix thus becomes $\mathcal{D}(\omega_n, q) = [\mathcal{D}_0^{-1}(\omega_n, q) + \Sigma(\omega_n, q)]^{-1}$, where $\Sigma(\omega_n, q)$ is the self energy due to the e-ph interaction and has the form

$$\Sigma(\omega_n, q) = -P(\omega_n, q) \begin{pmatrix} |g_T|^2 q^2 & -ig_T g_L^* q \\ ig_L g_T^* q & |g_L|^2 \end{pmatrix} \tag{2.35}$$

In the bosonized representation $P(\omega_n, q)$ is equal to

$$P(\omega_n, q) \;\; = \;\; \int \frac{2d^2r}{(\pi\xi)^2}\, e^{i\omega_n\tau - iqx - \frac{\pi}{2}\sum_j \langle[\Phi_j(r) - \Phi_j(0)]^2\rangle}.$$

due to the Debye-Waller relation $\langle T_\tau e^{\sum_j i(A_j\phi(r_j) + B_j\theta(r_j))}\rangle = e^{-\frac{1}{2}\langle T_\tau[\sum_j (A_j\phi(r_j) + B_j\theta(r_j))]^2\rangle}$ and the correlator is nonvanishing only if $\sum_j A_j = 0$ and $\sum_j B_j = 0$. The correlation functions of the Bosonic fields $\langle[\Phi_j(r) - \Phi_j(0)]^2\rangle = \frac{1}{2}\ln[\frac{\beta^2 u_j^2}{\pi^2\xi^2}(\sinh^2(\frac{\pi x}{\beta u_j}) + \sin^2(\frac{\pi\tau}{\beta}))]$ as given in the Appendix C of Ref [24]. In the long wavelength limit, $q, \omega \to 0$, and for $K_{c+} \ll 1$ we obtain,

$$P(0,0) \equiv P = \frac{1}{\pi^2 v_F}\left(\frac{\beta v_F}{\pi\xi}\right)^{1/2} B^2\left(\frac{3}{8}, \frac{1}{4}\right), \tag{2.36}$$

where $B(a,b)$ is the Euler Beta function.

The renormalized phonon frequencies are given by the poles of $\det[\mathcal{D}(\omega_n, q)]$ analytically continued to real frequencies. The instability first appears when the renormalized frequency of the acoustic mode, $\tilde{\omega}_T$, turns to zero

$$\tilde{\omega}_T^2 \equiv \omega_T^2 \frac{1-(\tilde{g}_T^2+\tilde{g}_L^2)v_F P}{1-\tilde{g}_L^2 v_F P} = 0, \tag{2.37}$$

where $\tilde{g}_T = g_T/\sqrt{\rho s_T^2 v_F}$ and $\tilde{g}_L = g_L/\sqrt{\rho\omega_o^2 v_F}$ are the characteristic dimensionless e-ph coupling constants for TA and LO phonons respectively. The mean field twist instability temperature is then

$$T_c = (\tilde{g}_T^2+\tilde{g}_L^2)^2 \frac{v_F}{\pi^5\xi} B^4\left(\frac{3}{8},\frac{1}{4}\right). \tag{2.38}$$

In one dimension fluctuations destroy any finite temperature long range order and shift the mean field instabilities to zero temperature. In the case under consideration the order parameter $\partial_x u$ is real and the instability is of the Ising type. As a result, a finite order parameter exists only at $T=0$, whereas at finite T one finds a state with a finite density of solitons (domain walls separating regions with different signs of $\partial_x u$). The mean field T_c is, however, not devoid of meaning and gives an estimate of the spectral gaps associated with the strong e-ph coupling. Using Feynmann's variational principle we can estimate the magnitudes of the gaps of the singlet excitations of the fields. Φ_j [24] These excitations represent small fluctuations around the minima of the action.

Generally one can write the partition function

$$Z = \int \mathcal{D}\phi e^{-S} = \int \mathcal{D}\phi e^{-S_0} e^{-(S-S_0)} = Z_0 \langle e^{-(S-S_0)}\rangle_0 \tag{2.39}$$

where S_0 is a trial action and S is the original one. The free energy is

$$F = F_0 - T\log[\langle e^{-(S-S_0)}\rangle_0] \tag{2.40}$$

which satisfies

$$F \leq F_{var} = F_0 + T\langle S - S_0\rangle_0 \tag{2.41}$$

due to the relation $\langle e^{-(S-S_0)}\rangle > e^{-\langle (S-S_0)\rangle}$. The idea is to use a tentative action S_0 that's simple and solvable yet as close as possible to the original physical one. One can then use this optimized action to compute physical properties of the condensed state. For the gapped state at low temperature, one reasonable trial action is the harmonic oscillator around the minimum of the backscattering Hamiltonian, which can be written as

$$S_0 = (2\beta L)^{-1} \sum_j \sum_{\omega_n, q} G_j^{-1}(\omega_n, q) |\Phi_j(\omega_n, q)|^2 \tag{2.42}$$

with

$$G_j^{-1}(\omega_n, q) = \frac{1}{\pi K_j}[\frac{1}{u_j}\omega_n^2 + u_j q^2 + \frac{\Delta_j^2}{u_j}]. \tag{2.43}$$

In the condensed state, we assume that the lattice is statically deformed, $\partial_x u_T = \eta$, $u_L = \zeta$, and the elastic energy due to this deformation is

$$F_{latt} = \frac{1}{2} N m [s_T^2 \eta^2 + \omega_o^2 \zeta^2], \tag{2.44}$$

where N is the total number of atoms in the CNT and m is the mass of a carbon atom.

The action of the electron including the e-phonon interaction is

$$S = \frac{\hbar}{2\pi} u_j \sum_j \int dx d\tau [K_j (\nabla \Phi_j)^2 + \frac{1}{K_j}(\nabla \Theta_j)^2] + \int dx d\tau M(x)[g_T \eta + g_L \zeta], \tag{2.45}$$

The total free energy corresponding to the variational action is

$$\begin{aligned} F_{var} &= \frac{1}{2} N m [s_T^2 \eta^2 + \omega_o^2 \zeta^2] - T \sum_{j, \omega_n, q} \ln[G_j(\omega_n, q)] + \sum_j \frac{T}{2\pi K_j} \sum_{\omega_n, q} [\frac{1}{u_j}\omega_n^2 + u_j k^2] G(\omega_n, q) \\ &\quad - \frac{8T}{\pi \xi} \beta L (g_T \eta + g_L \zeta) e^{-\frac{1}{2\beta L} \sum_{j, \omega_n, q} G_j(\omega_n, q)} \end{aligned} \tag{2.46}$$

Minimizing the free energy with respect to $G(\omega_n, q)$, i.e. $\frac{\partial F_{var}}{\partial G(\omega_n, q)} = 0$, we get the self consistent equation for the gap as

$$\frac{\Delta_j^2}{2 K_j u_j} = \frac{1}{\xi}(g_T \eta + g_L \zeta) \prod_{j \neq c+} \left(\frac{\xi \Delta_j}{v_F} \right)^{1/4}. \tag{2.47}$$

in the limit $K_{c+} \to 0$. Minimizing the total variational free energy with respect to the static deformations ζ and η one obtains in the same limit

$$\eta = \frac{1}{\pi\xi}\frac{4g_T}{\rho s_T^2}\prod_{j\neq c+}\left(\frac{\xi\Delta_j}{v_F}\right)^{1/4}, \tag{2.48}$$

$$\zeta = \frac{1}{\pi\xi}\frac{4g_L}{\rho\omega_o^2}\prod_{j\neq c+}\left(\frac{\xi\Delta_j}{v_F}\right)^{1/4}. \tag{2.49}$$

Combining Eqs. (2.47)-(2.49) gives identical gaps for the four electronic modes,

$$\Delta_j = \frac{v_F}{\xi}\left[\frac{8(\tilde{g}_T^2+\tilde{g}_L^2)}{\pi}\right]^2, \tag{2.50}$$

and a spontaneous twist angle of magnitude

$$\eta = \sqrt{\frac{2\pi}{1+(\tilde{g}_L/\tilde{g}_T)^2}}\frac{\Delta}{\sqrt{\rho s_T^2 v_F}}. \tag{2.51}$$

In the framework of the tight binding model, the values of the coupling constants can be expressed [27, 26, 17, 19] in terms of the derivative, $\frac{\partial J(r)}{\partial r}$, of the transfer integral $J(r)$ with respect to the bond length r. For armchair nanotubes these coupling constants were found to be $g_T = \frac{\sqrt{3}}{4}a\frac{\partial J(r)}{\partial r}$ and $g_L = \frac{3}{2}\frac{\partial J(r)}{\partial r}$, where $a = 2.5\,\text{Å}$ is the graphene lattice constant, $c = 1.4\,\text{Å}$ is the bond length, and $\frac{\partial J(r)}{\partial r} = -\lambda J_0/c$ with $J_0 = 2.6\,\text{eV}$ the hopping integral [28]. Here λ is a dimensionless constant whose theoretical value is 2 [18]. Theoretical calculations [8] give for the twiston phonon velocity $s_T \sim 1.4\times10^4\,\text{m}\,\text{s}^{-1}$ and for the LO phonon energy $\omega_0 \sim 0.18\,\text{eV}$. The linear mass density of an (N,N) armchair nanotube is $\rho = 4NM/a$ with M being the carbon atom mass. Consequently, the dimensionless couplings $\tilde{g}_T$ and $\tilde{g}_L$ are proportional to $1/\sqrt{R}$, which in turn implies a $1/R^3$ scaling of the twist gap, Eq. (2.50). For a $(5,5)$ armchair nanotube with $R \sim 0.35\,\text{nm}$, our estimate for the transition temperature, Eq. (2.38), is about 40 K and the estimate for the gap, Eq. (2.50), is about 70 K. As expected, the mean field instability temperature and the gap have the same order of magnitude. The twist angle is $\eta \sim 3\times10^{-4}\,\text{rad}$.

As mentioned above, solitonic effects will restore the symmetry at finite temperatures. However, if the length of the tube is shorter than the typical inter-soliton distance, the system will appear twisted on experimental time scales. The estimated characteristic twist angle for $(5,5)$ nanotubes, $\sim 0.01°$, is too small to be detected by STM imaging. However, for a freely suspended tube clamped at one end the accumulated rotation angle at a distance x from the clamp, $\theta(x) = \eta x/R$, becomes substantial for $x \sim 1\,\mu$m. This twist can be detected in torsional nanomechanical resonators, similar to those studied in Ref. [29], by measuring a deflection angle of a paddle attached to an armchair tube.

2.5 Competition between Pierls and Mott transition and the ground state of an armchair CNT

In the presence of both e-ph coupling and e-e interaction, the fate of the ground state of armchair CNT depends on the values of the coupling constants. If $g_1 > g_3 > 0$ it is easy to see from Eqs. (2.21) and (2.31) that the Umklapp processes and the twist instability cooperate and favor the same condensation pattern, $(\Phi_{c+}, \Phi_{c-}, \Phi_{s+}, \Phi_{s-}) = (0, 0, \frac{\sqrt{\pi}}{2}, \frac{\sqrt{\pi}}{2})$, for the bosonic fields. However, it is expected [15] that in nanotubes $g_3 > g_1 > 0$, leading to a competition between the twist instability and the Umklapp processes, which in this case favor a different condensation pattern, $(\Phi_{c+}, \Phi_{c-}, \Phi_{s+}, \Theta_{s-}) = (0, 0, 0, 0)$. The outcome of the competition depends on which transition gains more energy. The condensation energy of the two transitions can be estimated using the mean field action above. It turns out that the condensation energies of the two transitions are equal when the Peierls gap and the Mott gap are equal. So the insulating state with larger gap wins at low temperature. To estimate the gaps, we need to know the interaction constants. The e-phonon coupling constants are estimated within the tight binding approximation in the above text, and the Peierls gap for a (5,5) tube is about 70K. The gap scales with radius as $\sim 1/R^3$. Yet the theoretical estimate of the Umklapp coupling constant is difficult because of their sensitivity to the details of

the short range part of the e-e interaction. Numerical estimate of the Umklapp gap for (5,5) CNT ranges from under 100K to several hundred K depending on the short distance cutoff of the Coulomb interaction. And the Umklapp gap scales as $1/R^2$. So in wide tubes the Umklapp processes win. In ultra thin tubes, the Peierls gap may exceed the Mott gap and the twist instability may happen accompanying with a deformed lattice.

Chapter 3

PLASMON DECAY IN ARMCHAIR CARBON NANOTUBES

3.1 Introduction

In this chapter we consider plasmon decay in a finite geometry illustrated in Fig. 3.1. In this experimentally motivated [41] setup, a carbon nanotube connected to two metal leads is subject to THz electric field. Plasmon modes are excited by the THz electric field. The finite length of the device enables us to study the plasmon decay processes using perturbation theory in the backscattering interactions. We investigate how the decay processes affect the plasmon resonances and modify the device conductance.

In the conventional Fermi liquid description applicable to higher-dimensional conductors, separation of excitations into plasmons and Fermi-quasiparticles is not exact, leading to a plasmon decay by exciting quasiparticles [40]. In contrast, in one-dimensional conductors quasiparticles are ill-defined, and plasmon decays into other collective excitations of the electron liquid. In armchair carbon nanotubes, the other collective excitations are three neutral Bosonic modes. In the Luttinger liquid description, which contains only e-e forward scattering interaction, the plasmon mode as well as the three neutral modes is one of the eigenmodes of the linear spectrum so it does not decay. In the presence of backscattering, however, the plasmon mode is no longer an eigenmode and is subject to decay.

The plasmon decay is directly related to the energy dissipation in the device. Without backscattering, the plasmon mode excited by the THz electric field or temperature flushes to the metallic leads after a few reflections at the boundaries and is

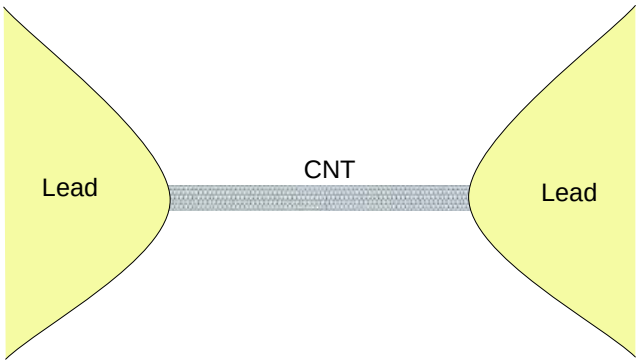

Figure 3.1: (Color online) Schematic representation of the device. A carbon nanotube (CNT) connected to two metal leads is subjected to ac-electric field.

dissipated in the leads. The backscattering in the carbon nanotube causes an intrinsic dissipation and the plasmon decays into neutral modes in the device. The same mechanism leads to the deviation of the device conductance from perfect conductance quanta. In a finite device with length $L \ll v_F/\Delta_u$ or at high temperature or high frequency, i.e. T or $\omega \gg \Delta_u$, perturbation calculation of the intrinsic plasmon decay rate is valid. We computed this decay rate and show that it's related to the ac conductivity of a uniform carbon nanotube by the Drude formula.

The chapter is organized as follows. In Sec. 3.2 we present the plasmon resonance in the absence of backscattering and the dissipation of plasmon into the leads. In Sec. 3.3 we study the intrinsic plasmon decay due to backscattering and its influence on energy dissipation. The relation between the plasmon decay rate and the ac conductivity in a uniform tube is also explored. Our results are summarized in Sec. 3.4.

3.2 Plasmon resonance in the absence of intrinsic dissipation

We consider the setup shown in Fig. 3.1. The plasmons excited in the tube get partially reflected from the junctions with the leads. The plasmon can be described by a one dimensional Luttinger liquid model introduced in Chapter 2,

$$H_0 + H_\rho = \sum_j \frac{u_j}{2\pi} \int dx [K_j^{-1} (\partial_x \Phi_j)^2 + K_j (\partial_x \Theta_j)^2], \tag{3.1}$$

with spatially dependent Luttinger parameters [44, 45, 46] defined as follows. For the charge mode the Luttinger parameter is equal to K_{c+} inside the tube, $0 < x < L$, and unity in the leads. The Luttinger parameters in the neutral modes are equal to unity both in the tube and in the leads.

We denote the THz electric field by $E_\omega(x)$. Its distribution along the wire depends on the details of the device geometry and is a solution of the Maxwell equations with proper boundary conditions; here we assume $E_\omega(x)$ is known. The dissipation rate of the electric field energy in the device can be written as

$$W(\omega) = \frac{1}{2} \mathrm{Re} \int_0^L dx_1 \int_0^L dx_2 E_\omega(x_1) E_\omega^*(x_2) \sigma_\omega(x_1, x_2), \tag{3.2}$$

where $\sigma_\omega(x, x')$ is the nonlocal conductivity, which can be expressed via the retarded current-current correlation function by the usual Kubo formula,

$$\sigma_\omega(x, x') = \frac{e^2}{\omega} \int_0^\infty dt\, e^{i\omega t} \langle [j(x,t), j(x',0)] \rangle. \tag{3.3}$$

We assume that the electric field: (i) varies smoothly on the scale of the lattice constant within the tube and (ii) preserves the reflection symmetry of the tube. Because of (i) it will not scatter electrons between the valleys, which involves momentum transfer $\sim 2Q$. Due to (ii) parity conservation also forbids backscattering of electrons within the same valley. Thus the electric field couples only to the smooth part of the current density, which can be expressed in the bosonized form as $j = 2\frac{e}{\pi} \partial_t \Phi_{c+}$. Therefore we can express the conductivity in terms of the Green's function of the Φ_{c+} field,

$$\sigma_\omega(x, x') = 4e^2 \frac{i\omega}{\pi^2} G_\omega^R(x, x'), \tag{3.4}$$

where

$$G^R_\omega(x,x') = -i\int_0^\infty dt\, e^{i\omega t}\langle[\Phi_{c+}(x,t),\Phi_{c+}(x',0)]\rangle \tag{3.5}$$

is the retarded GF of the plasmon mode.

We denote the Green's function of the plasmon mode in the absence of backscattering by $G^R_{0,\omega}(x,x')$. It satisfies the differential equation

$$\left\{\partial_x\left(\frac{v_F}{K^2(x)}\partial_x\right)+\frac{\omega^2}{v_F}\right\}G^R_{0,\omega}(x,x') = \pi\delta(x-x'), \tag{3.6}$$

with the boundary conditions: (1) $G^R_{0,\omega}(x,x')$ is continuous at $x=0,L$ and $x=x'$; (2) $[v_F/K^2(x)]\partial_x G^R_{0,\omega}(x,x')$ is continuous at $x=0,L$. For our model ($K(x)$ equal to K_{c+} inside the tube and unity outside) the Green's function can be expressed in terms of the reflection amplitude, r, of the plasmon from the junction with the lead. The latter is determined by the ratio of the plasmon velocities in the tube and in the lead and is given by $\mathrm{r}=\frac{1-K_{c+}}{1+K_{c+}}$.

The dissipated power in Eq. (3.2) depends only on the Green's function inside the tube. In this region, for $0<x<x'<L$, it is given by

$$G^R_{0,\omega}(x,x') = \frac{\pi K_{c+}}{2i\omega}\frac{e^{i\omega L/u}}{1-\mathrm{r}^2e^{2i\omega L/u}}\left(e^{-i\frac{\omega}{u}x}+\mathrm{r}\,e^{i\frac{\omega}{u}x}\right)\times\left(e^{i\frac{\omega}{u}(x'-L)}+\mathrm{r}\,e^{-i\frac{\omega}{u}(x'-L)}\right). \tag{3.7}$$

In the region $0<x'<x<L$ the Green's function is obtained by exchanging x and x' in the right hand side.

The above Green's function has poles as a function of frequency ω. The real part of the pole gives the resonance frequency $\omega_n = n\pi u/L$, and its imaginary part gives the resonance half-width, γ_Z. Expressing the plasmon reflection amplitude r in terms of the Luttinger parameter K_{c+} we obtain for the escape half-rate, $\gamma_Z = \frac{u}{L}\log\left(\frac{1+K_{c+}}{1-K_{c+}}\right)$. In the limit of high charge stiffness, $K_{c+}\ll 1$, it becomes much smaller than the spacing between consecutive resonances and independent of the interaction strength, $\gamma_z \simeq 2K_{c+}\frac{u}{L} = 2v_F/L$.

The dissipated power is given by Eqs. (3.2), (3.4), and (3.7) and depends not only on the properties of the tube but also on the spatial distribution of the electric field (as mentioned above, the latter depends on the geometry and is assumed known).

3.3 Intrinsic plasmon decay due to back scattering in the device

The energy dissipation described by the ac conductance obtained in Sec. 3.2 corresponds to the emission of plasmon waves into the leads. The THz electric field excites plasmon modes of the electron fluid, which after a few reflections from the contacts with the leads are radiated out into the leads. Thus the energy absorbed from the THz radiation is re-radiated into the leads in the form of a plasmon flux.

In the presence of backscattering interactions, there is an additional contribution to the dissipation energy in the device. The plasmon waves generated by the THz radiation can decay into neutral modes before escaping into the leads. In this dissipation channel the absorbed energy is carried into the leads by the neutral modes. We discuss the intrinsic plasmon decay and the energy dissipation in the device due to back scattering interaction in Sec. 3.3.1. In Sec. 3.3.2, we evaluate the intrinsic plasmon decay rate and relate it to the ac conductivity of the tube.

3.3.1 Intrinsic plasmon decay and energy dissipation in the device

The backscattering interactions lead to the possibility of plasmon decay into the neutral modes. Using the fact that the backscattering interactions are small in $1/N$ we evaluate the decay rate and the corresponding correction to the device conductance using perturbation theory. We work in the regime where the cumulative plasmon decay rate in the device is smaller than the rate of elastic escape of plasmons into the leads. In this case the correction to the device conductance due to plasmon decay can be treated perturbatively.

Both the Umklapp and the e-ph backscattering interactions are expressed in terms of exponentials of the charge mode, Φ_{c+}. As a result, their contribution to the plasmon decay and the device conductance can be evaluated along similar lines.

To second order in perturbation theory there is no cross-correlation between the Umklapp and electron-phonon backscattering processes, and the retarded Green's

function of the charge mode can be expressed as

$$G^R_\omega(x,x') = G^R_{0,\omega}(x,x') + \sum_\eta \int_0^L dx_1 \int_0^L dx_2\, G^R_{0,\omega}(x,x_1)\mathcal{K}^\omega_\eta(x_1,x_2)G^R_{0,\omega}(x_2,x'), \quad (3.8)$$

where the index η denotes either the Umklapp ($\eta = u$) or the electron-phonon ($\eta = ep$) interaction, and the kernel $\mathcal{K}^\omega_\eta(x_1,x_2)$ can be expressed in terms of the retarded correlation function of the corresponding backscattering perturbation as

$$\begin{aligned}\mathcal{K}^\omega_\eta(x,x') &= -ia_\eta^2 \int dt \left[e^{i\omega t}\langle[\mathcal{H}_\eta(x,t),\mathcal{H}_\eta(x',0)]\rangle_0 - \right. \\ &\left. \int_0^L d\xi \langle[\mathcal{H}_\eta(x,t),\mathcal{H}_\eta(\xi,0)]\rangle_0 \delta(x-x')\right]. \end{aligned} \quad (3.9)$$

Here a_η is the coefficient in the exponential dependence, $\sim (e^{ia_\eta\Phi_{c+}} + h.c.)$, of the corresponding backscattering perturbation on the charge field Φ_{c+}. The derivation of Eqs. (3.8) and (3.9) is outlined in Appendix B. The first term in Eq. (3.8) is the Green's function of the plasmon in the Luttinger liquid approximation, Eq. (3.7). The remaining terms represent correction due to backscattering interactions. The first term in the right hand side of Eq. (3.9) corresponds to the usual RPA-like diagram, the second term comes from the tadpole diagram and describes elastic scattering. The average $\langle \ldots \rangle_0$ is performed with respect to the quadratic Luttinger liquid Hamiltonian, Eq. (3.1).

In the spatially inhomogeneous setup considered here the kernel $\mathcal{K}^\omega_\eta(x_1,x_2)$ depends not only on the coordinate difference but also on the center of mass coordinate $(x_1+x_2)/2$. Its evaluation leads to rather cumbersome expressions. The situation simplifies in the physically relevant regime, where the characteristic thermal wavelength of the neutral modes, $L_T = v_F/T$, is much shorter than the size of the device L, while the wavelength of the plasmon resonance is on the order L.

In this case the Green's functions of the plasmon mode in the second term of Eq. (3.8) depend on x_1 and x_2 on the scale of wavelength of the plasmon resonance, $\sim L$. On the other hand, because backscattering operators depend exponentially on

the neutral modes, $H_\eta(x,t) \sim \exp(ia_\eta \Phi_j(x,t))$, their correlator $\mathcal{K}^\omega_\eta(x_1,x_2)$ falls off exponentially for $|x_1 - x_2| > L_T$, which is much shorter than the length of the tube L. This is especially apparent in the case of a uniform wire for which the correlators of exponentials of bosonic fields have a simple form [24],

$$\begin{aligned} &\left\langle e^{ia\Phi_j(x,t)} e^{-ia\Phi_j(0,0)} \right\rangle_0 \equiv \Pi(K_j, a; x, t) \\ = \quad & \frac{(\pi\xi T K_j/v_F)^{a^2 K_j/2}}{\{\sinh[\pi T(K_j x/v_F - t_-)] \sinh[\pi T(K_j x/v_F + t_-)]\}^{a^2 K_j/4}}, \end{aligned} \tag{3.10}$$

where $t_- = t - i\epsilon$.

In the inhomogeneous situation the kernel $\mathcal{K}^\omega_\eta(x_1,x_2)$ still decays exponentially for $|x_1 - x_2| > L_T$. Therefore the main contribution to the Green's function correction in Eq. (3.8) comes from the region $|x_1 - x_2| \leq L_T$. At such separations only the fluctuations of bosonic modes with wavelengths less than L_T contribute to the correlator. In the regime of interest, $L_T \ll L$, such short wavelength vibrations can be described semiclassically and are insensitive to the boundary conditions at the junctions, which describe reflection processes [1]. Thus we come to the conclusion that in the bulk of the nanotube, i.e. with the exception of the regions of size L_T near the junctions the correlator $\mathcal{K}^\omega_\eta(x_1,x_2)$ is the same as in a homogeneous tube, and can be replaced by the local kernel

$$\mathcal{K}^\omega_\eta(x_1,x_2) \to \delta(x_1 - x_2)\mathcal{K}^\omega_\eta(q=0), \tag{3.11}$$

where

$$\mathcal{K}^\omega_\eta(q=0) = -ia_\eta^2 \int_{-\infty}^{\infty} dx \int_0^\infty dt (e^{i\omega t} - 1) \times \langle [\mathcal{H}_\eta(x,t), \mathcal{H}_\eta(0,0)] \rangle_0. \tag{3.12}$$

This observation enables us to express the correction to the dissipated power due to decay of plasmons into neutral modes in terms of intrinsic parameters of uniform

[1] The quasiclassical treatment becomes inapplicable in the regions within L_T of one of the junctions, but the contribution of these regions to the overall decay rate is small as compared to that of the rest of the tube.

nanotubes. Accordingly, all correlation functions of backscattering operators will be evaluated for infinite homogeneous nanotubes below.

With the aid of Eq. (3.11) the power dissipation rate in Eq. (3.2) can be written in the form

$$W(\omega) = W_0(\omega) + \mathrm{Im}\sum_{\eta} \mathcal{K}_{\eta}^{\omega}(\mathrm{q}=0)\mathrm{F}(\omega). \tag{3.13}$$

Here the first term corresponds to the dissipation rate due to the escape of plasmon to the leads and is given by

$$W_0(\omega) = \frac{2e^2\omega}{\pi^2}\int_0^L dx_1 \int_0^L dx_2 \times \mathrm{Im}\, E_\omega(x_1) E^*_\omega(x_2) G^R_{0,\omega}(x_1,x_2). \tag{3.14}$$

The second term in Eq. (3.13) corresponds to the intrinsic dissipation due to the electronic Umklapp processes and electron-phonon backscattering. It can be expressed in terms of kernel for an infinite tube, Eq. (3.12), and the form-factor $F(\omega)$,

$$F(\omega) = \frac{2e^2\omega}{\pi^2}\int_0^L dx_1 \int_0^L dx_2 \int_0^L dx_3\, E_\omega(x_1)\, E^*_\omega(x_3) \times\, G^R_{0,\omega}(x_1,x_2)\, G^R_{0,\omega}(x_2,x_3), \tag{3.15}$$

which is quadratic in the THz electric field and depends, through its spatial distribution, on the geometry of the device.

Both the electric field and the unperturbed Green's function $G^R_{0,\omega}$ of the Luttinger liquid are temperature independent. Therefore $W_0(\omega)$ and the form-factor $F(\omega)$ do not depend on temperature. All the temperature dependence of the dissipation rate $W(\omega)$ is thus totally determined by intrinsic properties of a uniform CNT and is described by the kernel $\mathcal{K}_{\eta}^{\omega}(q=0)$.

3.3.2 Plasmon decay rate and the ac conductivity of the tube

We note that the kernel $\mathcal{K}_{\eta}^{\omega}(q=0)$ also determines the ac-conductivity $\sigma_\omega(q=0)$ of an infinite wire [24] in the high frequency or high temperature regime, where backscattering interactions can be treated perturbatively. The latter can be expressed in

the form

$$\sigma(\omega, T) = \frac{4e^2 K_{c+} u}{\pi(-i\omega + \sum_\eta \gamma_\eta)}. \tag{3.16}$$

Here γ_η is the relaxation rate due to the Umklapp ($\eta = u$) or electron-phonon ($\eta = ep$) back-scattering, which can be expressed in terms of the local kernel as

$$\gamma_\eta \equiv \frac{i}{\omega} K_{c+} u_{c+} \mathcal{K}_\eta^\omega (q = 0). \tag{3.17}$$

Thus with the aid of Eqs. (3.13), (3.15) and (3.17) the temperature dependent part of the power dissipation in the device can be expressed in terms of the intrinsic plasmon decay rate in a uniform CNT, γ_η, which is given by Eqs. (3.17) and (3.12).

In the remainder of this section we evaluate the intrinsic plasmon decay rate due to various backscattering processes.

Umklapp mechanism of attenuation

We begin by considering Umklapp-mediated plasmon decay rate, γ_u. The Umklapp Hamiltonian density in the equation below contains exponential operators of both Φ- and Θ-fields corresponding to the neutral modes:

$$\mathcal{H}_u = -\frac{\cos(2\Phi_{c+} - 4k_F x)}{2(\pi\xi)^2}\{g_3 \cos(2\Theta_{s-}) + (g_3 - g_1)\cos(2\Phi_{s+}) + g_1[\cos(2\Phi_{c-}) - \cos(2\Phi_{s-})]\}. \tag{3.18}$$

Because the Luttinger parameter K for neutral modes is equal to unity, the correlators of exponential operators of Φ- and Θ-fields coincide. As a result we obtain

$$\langle \mathcal{H}_u(x,t)\mathcal{H}_u(0,0)\rangle_0 = \frac{3g_1^2 + 2g_3^2 - 2g_1 g_3}{16(\pi\xi)^4} \cos(4k_F x) \times \Pi(K_{c+}, 2; x, t)\Pi(1, 2; x, t). \tag{3.19}$$

The analogous correlator corresponding to the opposite ordering of backscattering operators can be obtained from the identity

$$\langle \mathcal{H}_u(0,0)\mathcal{H}_u(x,t)\rangle_0 = \langle \mathcal{H}_u(x,t)\mathcal{H}_u(0,0)\rangle_0^*.$$

Using Eqs. (3.17), (3.12), (3.10), and (3.19) we obtain

$$\gamma_u = \left(\frac{\pi T\xi}{u}\right)^{2K_{c+}} \frac{3g_1^2 + 2g_3^2 - 2g_1 g_3}{4T(\pi\xi)^2} F_u\left(\frac{\omega}{T}, \frac{v_F k_F}{T}\right), \tag{3.20}$$

where $F_u(\frac{\omega}{T}, \frac{v_F k_F}{T})$ is a scaling function depending on the ratio ω/T and $v_F k_F/T$. It is given by the following double integral,

$$F_u\left(\frac{\omega}{T}, \frac{v_F k_F}{T}\right) = \frac{T}{\omega}\int_{-\infty}^{\infty} dX \int_0^{\infty} dY \left(e^{i\frac{\omega}{T}Y} - 1\right)\cos\left(\frac{4k_F v_F}{T}X\right)$$
$$\left[\frac{1}{(\sinh\pi(\frac{v_f}{u}X + Y_-)\sinh\pi(\frac{v_f}{u}X - Y_-))^{K_{c+}}}\frac{1}{\sinh\pi(X+Y_-)\sinh\pi(X-Y_-)} - c.c.\right], \tag{3.21}$$

where $Y_- \equiv Y - i\epsilon$.

Using the standard deformation of the integration contour, $Y_- \to Y - i/2$, in the above equation one may express the real part of the scaling function in the form that is more convenient for numerical evaluation,

$$\Re F_u\left(\frac{\omega}{T}, \frac{v_F k_F}{T}\right) =$$
$$\frac{T}{\pi^2\omega}\sinh\frac{\omega}{2T}\int_{-\infty}^{\infty} dx \int_{-\infty}^{\infty} dy \frac{\cos(y\,\omega/\pi T)\cos(4k_F v_F x/\pi T)}{\left[\cosh(K_{c+}x + y)\cosh(K_{c+}x - y)\right]^{K_{c+}}\cosh(x+y)\cosh(x-y)}. \tag{3.22}$$

In the limit of high charge stiffness, $K_{c+} \to 0$, the above expression simplifies to,

$$\Re F_u\left(\frac{\omega}{T}, \frac{v_F k_F}{T}\right) = \frac{\frac{T}{2\omega}\sinh\frac{\omega}{2T}}{\cosh\left(\frac{4k_F v_F + \omega}{4T}\right)\cosh\left(\frac{4k_F v_F - \omega}{4T}\right)}. \tag{3.23}$$

In the temperature regime of interest, $T \gg \omega \sim u/L$, the function $F_u(\frac{\omega}{T}, \frac{v_F k_F}{T})$ in Eq. (3.21) reaches the dc limit $F_u(0, \frac{v_F k_F}{T})$, which is purely real and depends only on the doping level. For comparison, in Fig. 3.2 we plot the static limit of the scaling function $F_u(0, k_F v_F/T)$ evaluated numerically at $K_{c+} = 0.2$ using Eq. (3.22) and the analytical expression from Eq. (3.23) for $K_{c+} = 0$.

At small doping, the scaling function goes to a constant and γ_u exhibits a power law dependence on the temperature, $\gamma_u \sim T^{2K_{c+}-1}$. At strong doping, $2k_F v_F > T$

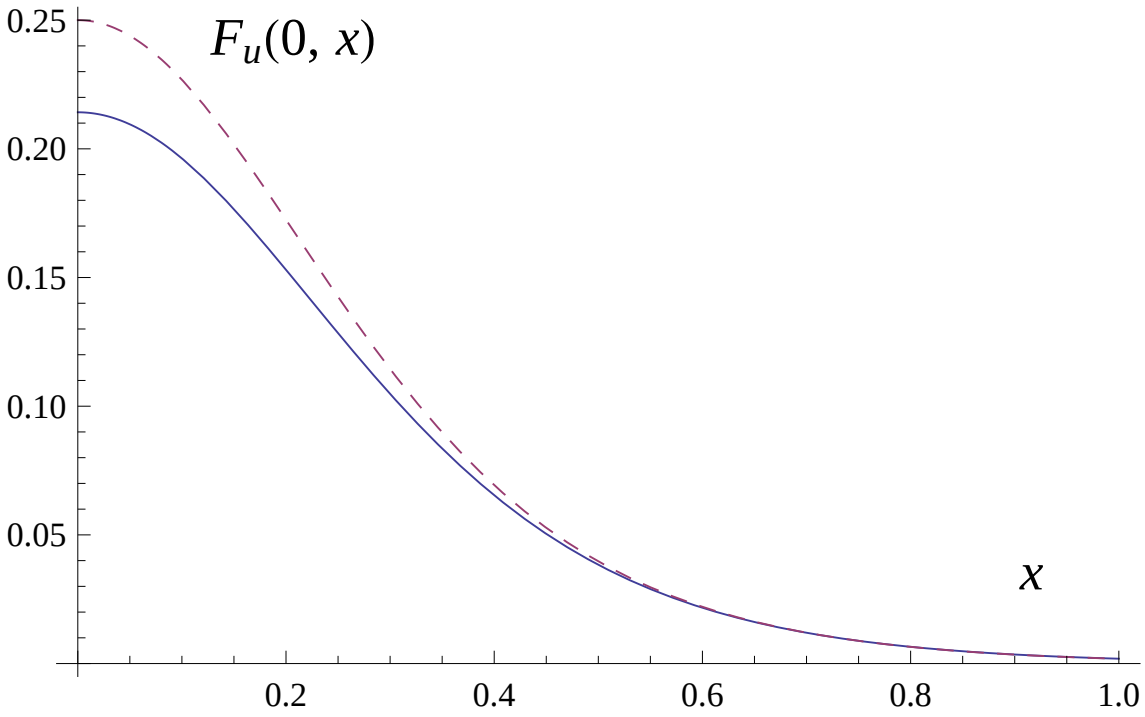

Figure 3.2: Dependence of the scaling function in the static limit, $F_u(0, x)$ on the doping parameter $x = \frac{k_F v_F}{T}$ for $K_{c+} = 0.2$ (solid line) and $K_{c+} = 0$ (dashed line).

the scaling function acquires an activated temperature dependence. This results in exponential decay of $\gamma_u \sim T^{2K_{c+}-1}\exp(-2k_F v_F/T)$. The physical reason for the exponential temperature decay can be understood from simple inspection of energy and momentum conservation, which shows that energetically optimal process involves backscattering of two thermal quasiparticles exactly at the Dirac point $k = Q$. At strong doping, $k_F v_F \gg T$ the occupancy of such states is exponentially small, $\sim \exp(-2k_F v_F/T)$.

Equation (3.20) and the subsequent equations express the plasmon decay rate γ_u in terms of the somewhat arbitrary short distance cutoff, ξ, which has the order of the radius of carbon nanotube. Alternatively, γ_u can be expressed in a renormalized form as a function of an intrinsic cutoff-independent low energy scale. In the case of Umklapp interactions the role of such a low energy scale is played by the Umklapp gap. Namely, the Umklapp interaction is a relevant perturbation relative to the Luttinger liquid fixed point and drives the system to a Mott insulating state with the gap [15],

$$\Delta_u \sim \frac{v_F}{\xi}\left(\frac{g_u}{v_F}\right)^{1/(1-K_{c+})}.$$

Here $g_u \sim e^2/N$ is the strength of the Umklapp interaction. This gap depends on the radius of the CNT as $R^{-[1+1/(1-K_{c+})]}$ and is hard to evaluate theoretically due to the ambiguity of the coupling constant, but numerical results estimate that it's of the order of $1-10$ meV for an armchair CNT of radius ~ 1 nm [15]. For the perturbation calculation to be applicable, the temperature we consider should be above the Umklapp gap. Up to a numerical coefficient on the order unity the plasmon decay rate in Eq. (3.20) can be expressed in terms of this gap as

$$\gamma_u \sim \Delta_u \left(\frac{T}{\Delta_u}\right)^{2K_{c+}-1} F_u\left(\frac{\omega}{T}, \frac{v_F k_F}{T}\right). \tag{3.24}$$

At zero doping, $\gamma_u \sim T$ for $K_{c+} \to 1$, i.e., without considering the Luttinger liquid effect. Yet in the Luttinger liquid description with strong Coulomb interaction, $K_{c+} \to 0$, $\gamma_u \sim \Delta_u^2/T$.

Note that according to Eqs. (3.16) and (3.24) the Umklapp processes yield $\sigma(\omega = 0, T) \propto T^{1-2K_{c+}}$ at zero doping and high temperature, which is consistent with the result obtained in a previous work [13]. In the case $K_{c+} \to 1$, i.e., in the absence of Luttinger liquid effects, the decay rate due to Umklapp processes $\gamma_u \sim T$, and the resistivity has linear dependence on temperature at high temperature, which is consistent with the perturbative calculation of the plasmon decay rate from Umklapp processes in CNTs [47, 23]. We can see that the inclusion of the long range interaction significantly modifies the dependence of the plasmon decay rate on temperature due to Umklapp processes. In the case of strong Coulomb interaction, i.e., $K_{c+} \to 0$, the temperature dependence of decay rate is strongly modified and becomes $\gamma_u \sim T^{-1}$ at high temperature.

Phonon-assisted mechanism of attenuation

We now consider plasmon decay rate due to electron-phonon interactions, γ_{ep}. The e-phonon processes were studied in Chapter 2 and the Hamiltonian in Bosonized form is

$$H_{ep} = \int dx M(x)[g_T \partial_x u_T(x) + g_L u_L(x)], \tag{3.25}$$

where the operator $M(x)$ has the form

$$\begin{aligned} M &= -\frac{4}{\pi\xi}\left[\prod_{\nu=\pm}\cos(\sqrt{\pi}\Phi_{c\nu})\sin(\sqrt{\pi}\Phi_{s\nu})\right. \\ &\quad \left. + \prod_{\nu=\pm}\sin(\sqrt{\pi}\Phi_{c\nu})\cos(\sqrt{\pi}\Phi_{s\nu})\right]. \end{aligned} \tag{3.26}$$

Its physical mechanism can be understood as follows. Parity-breaking deformations in the TA mode cause single particle backscattering, which causes the plasmon decay. Due to the presence of the adiabatic parameter $s_T/v_F \sim 2 \times 10^{-2} \ll 1$ the lattice deformations are effectively static. Thus the energy of the decaying plasmon is transferred into the neutral modes of the electron liquid. Therefore this mechanism, which we analyze below, may be characterized as phonon-assisted plasmon

decay. In two dimensions it has been studied in Ref. [51]. At finite doping single electron backscattering involves phonons with momentum $2k_F$. With the exception of very low temperatures, $T < 2k_F s_T$, the occupation numbers of such phonons are large, $\sim T/2k_F s_T$. This corresponds to the classical thermal fluctuations of the lattice. Since the probability of such fluctuations is determined by the elastic energy $\sim \exp(-s_T \int dx[\partial_x \phi_T(x)]^2/2T)$, the one-electron backscattering potential $\sim \partial_x \phi_{TA}(x)$ (see Eq. (3.25)) may be viewed as δ-correlated in space. More precisely, the correlator of backscattering potential $\sim \partial_x \phi_{TA}(x)$ becomes exponentially small at distances greater than s_T/T, as is clear from Eq. (3.28) below. As the electron correlators depend on the spatial coordinates on much larger scales $\sim L_T \gg s_T/T$ the correlator of deformation potentials becomes effectively short range. In this respect the phonon-assisted plasmon decay mechanism is similar to that induced by a short range disorder potential. The temperature dependence of the disorder-induced conductivity was obtained in Ref. [42] as, $\sigma_{dis} \sim \langle V^2 \rangle T^{(K_{c+}-1)/2}$, where $\langle V^2 \rangle$ is the variance of the random potential. In contrast to the temperature-independent variance of the disorder potential, the variance of the phonon correlator scales linearly with the temperature. This gives the power law $\gamma_{ep} \sim T^{(1+K_{c+})/2}$, which is confirmed by the calculations below.

The phonon-assisted decay rate γ_{ep} can be evaluated similarly to the case of Umklapp processes. Using Eq. (3.10) we obtain the following expression for the correlation function for the electron-phonon Hamiltonian densities given by Eq. (3.25),

$$\begin{aligned} \langle \mathcal{H}_{ep}(x,t)\mathcal{H}_{ep}(0,0)\rangle &= 2\left(\frac{g_T}{\pi\xi}\right)^2 \cos(2k_F x) D_{ph}(x,t) \\ &\quad \times \prod_j \Pi(K_j, 1; x, t), \end{aligned} \tag{3.27}$$

where $j = c\pm, s\pm$, and $D_{ph}(x,t) \equiv \langle \nabla\varphi_T(x,t)\nabla\varphi_T(0,0)\rangle$ is the phonon correlator given by

$$D_{ph}(x,t) = -\sum_{\nu=\pm 1} \frac{(\pi T/s_T)^2}{2\sinh^2[\pi T(\frac{x}{s_T} + \nu t_-)]}. \tag{3.28}$$

The correlator with opposite ordering can be obtained from Eq. (3.27) using the identity $\langle \mathcal{H}_{ep}(0,0)\mathcal{H}_{ep}(x,t)\rangle = \langle \mathcal{H}_{ep}(x,t)\mathcal{H}_{ep}(0,0)\rangle^*$.

Substituting Eqs. (3.27), (3.10) and (3.28) into Eq. (3.12) and using Eq. (3.17) we obtain the phonon-assisted rate γ_{ep}. While carrying out the spatial integration in Eq. (3.12) we may neglect the position dependence in the electronic correlation functions and replace them by $\Pi(K_j, 1; x = 0, t)$ (this is justified by the small value of the adiabatic parameter s_T/v_F). Doing so we obtain

$$\gamma_{ep} = \tilde{g}_T^2 \frac{\pi v_F}{\xi} \left(\frac{\pi T\xi}{v_F}\right)^{\frac{1}{2}} \left(\frac{\pi T\xi}{u}\right)^{\frac{K_{c+}}{2}} F_{ep}\left(\frac{\omega}{T}, \frac{s_T k_F}{T}\right), \tag{3.29}$$

where $\tilde{g}_T \equiv g_T/\sqrt{s_T v_F}$ is the dimensionless coupling constant of e-ph interaction, $F_{ep}(\frac{\omega}{T}, \frac{s_T k_F}{T})$ is the scaling function for the phonon-assisted decay rate. Introducing dimensionless variables $X = xT/s_T$ and $Y = Tt$ we can express it as

$$F_{ep}\left(\frac{\omega}{T}, \frac{s_T k_F}{T}\right) = \frac{T}{\omega}\int_0^\infty dY \int_{-\infty}^\infty dX \left(e^{i\frac{\omega}{T}Y} - 1\right) \cos\left(\frac{2k_F s_T}{T} X\right)$$
$$\left\{ \left[\frac{1}{\sinh^2\left(\pi(X + Y_-)\right)} + \frac{1}{\sinh^2\left(\pi(X - Y_-)\right)}\right] \left(\frac{1}{\sinh\left(\pi Y_-\right)\sinh(-\pi Y_-)}\right)^{\frac{3+K_{c+}}{4}} - c.c. \right\}. \tag{3.30}$$

Similar to the Umklapp case, the real part of the above scaling function can be expressed in a more convenient form,

$$\Re F_{ep}\left(\frac{\omega}{T}, \frac{s_T k_F}{T}\right)$$
$$= \frac{T}{\pi^2 \omega} \sinh\frac{\omega}{2T} \int_{-\infty}^\infty dy \int_{-\infty}^\infty dx \left[\frac{1}{\cosh^2(x+y)} + \frac{1}{\cosh^2(x-y)}\right] \frac{\cos\frac{\omega y}{\pi T} \cos\frac{2k_F s_T x}{\pi T}}{(\cosh y)^{(3+K_{c+})/2}}. \tag{3.31}$$

From the above equations it is clear that the phonon-assisted decay rate is practically unaffected by doping as long as $T > 2k_F s_T$. Because of the slow velocity s_T of the phonon mode, with the exception of very low temperatures, this condition is

satisfied for all practically accessible doping levels. In this regime Eq. (3.31) simplifies to

$$\Re F_{ep}\left(\frac{\omega}{T},0\right)=\frac{2\,T}{\pi^2\omega}\sinh\frac{\omega}{2T}\,2^{\frac{3+K_{c+}}{2}}\times B\left(\frac{3+K_{c+}}{4}-\frac{i\omega}{2\pi T},\frac{3+K_{c+}}{4}+\frac{i\omega}{2\pi T}\right). \qquad (3.32)$$

In the limit $\omega \ll T$, the scaling function goes to a constant, $F_{ep}(0,0) = 2^{\frac{3+K_{c+}}{2}} B([3+K_{c+}]/4, [3+K_{c+}]/4)/\pi^2$.

Similarly to the case of Umklapp processes the phonon assisted decay rate can be expressed in terms of a renormalized form, which does not involve the short distance cutoff. In this case the role of the low energy scale for the electron-phonon interaction with the TA mode is played by the twist Peierls gap [48], $\Delta_{ep} \sim \frac{v_F}{\xi}\,\tilde{g}_T^{4/(1-K_{c+})}$, which depends on the radius of the CNT as $\sim R^{-[1+2/(1-K_{c+})]}$ and in the limiting case $K_{c+} \to 0$ is on the order of a few tens of Kelvin for a $(5,5)$ armchair CNT. This gap is induced by the Peierls instability of the armchair tube with respect to a twist distortion [8, 9, 48]. Up to a numerical coefficient of the order of unity the phonon-assisted decay rate can be expressed in terms of the twist Peierls gap as,

$$\gamma_{ep} \sim \Delta_{ep}\left(\frac{T}{\Delta_{ep}}\right)^{\frac{1+K_{c+}}{2}} F_{ep}\left(\frac{\omega}{T},\frac{s_T k_F}{T}\right). \qquad (3.33)$$

In the dc limit and at zero doping, the Luttinger liquid effects manifest themselves by changing the power dependence of γ_{ep} or resistivity from $\gamma_{ep} \sim T$ for the non-interacting case [49] to $\gamma_{ep} \sim T^{\frac{1+K_{c+}}{2}}$ in a Luttinger liquid at temperatures above the Peierls gap. Experiments on phonon-induced resistivity to date [49, 50] have been conducted on CNTs placed on substrates rather than freely suspended CNTs, and exhibit linear temperature dependence of resistivity, consistent with the non-interacting electron approximation, $K_{c+} = 1$.

3.4 Summary of the results

We studied the intrinsic plasmon decay rates in clean armchair nanotubes. Plasmon oscillations decay into neutral electron modes. Such processes are facilitated by e-e

and electron-phonon backscattering processes. In the second order of perturbation theory in the backscattering interactions, the total decay rate is given by the sum of partial decay rates due to each mechanism. For undoped CNT, both electron-electron and electron-phonon rates reveal power law dependence on the frequency of oscillations or the temperature of the system with non-integer exponent, that depends on the Luttinger liquid parameter K_{c+}.

The plasmon decay processes lead to temperature dependent corrections to the power dissipation in the device depicted in Fig. 3.1. Therefore they can be studied experimentally in a finite device by measuring the temperature dependence of the power dissipation. In the regime where the temperature length $L_T = v_F/T$ is shorter than the plasmon wavelength the temperature-dependent part of the dissipated power can be expressed in terms of the instrinsic plasmon decay rate γ in homogeneous nanotube using Eqs. (3.13-3.15) and (3.17). Furthermore, in this regime γ can be related to the intrinsic ac conductivity of carbon nanotubes via Eq. (3.16). Thus intrinsic plasmon decay rate in CNT can, in principle, be extracted from measurements in finite size devices.

Our description of a finite-length CNT as a one-dimensional system is applicable if the length scale L_T lies between the CNT length and the length of its circumference. For a long ($\sim 10\,\mu$m) single-wall CNT of a typical radius of 1nm this condition is satisfied in the temperature range of $1\text{K} < T < 10^4$ K. The long wavelength limit used to describe phonons reduces the upper constraint to $\sim 3 \times 10^2$ K.

Among the electron-electron interactions resulting in plasmon decay the most relevant ones are the Umklapp processes. They correspond to backscattering of pairs of electrons and lead to a decay rate that scales as $\gamma_u \sim T^{2K_{c+}-1}$ at zero doping and becomes exponentially small, $\sim \exp(-2k_F v_F/T)$, at large doping, see Eq. (3.20). This rate can be expressed in terms of the short distance cutoff and Umklapp coupling constants, see Eq. (3.20) or in terms of the cutoff-independent Umklapp gap, as in Eq. (3.24).

In contrast to the Umklapp processes, the phonon-assisted decay rate depends on the doping level only on a very large scale, $v_F k_F \sim T v_F/s_T \approx 0.6 \times 10^2\, T$. With the exception of rather low temperatures the practically achievable doping levels lie below this scale. In this regime the phonon-assisted decay rate scales as $\gamma_{ep} \sim T^{(1+K_{c+})/2}$, as given by Eq. (3.29). It can also be expressed in terms of a cutoff-independent energy scale Δ_{ep} associated with electron-phonon interactions, see Eq. (3.33). This scale is given by the gap in the electron spectrum induced by the twist Peierls instability.

If the plasmon frequency is smaller than the temperature, the ratio of the phonon-assisted rate and the Umklapp one at zero doping is $\gamma_{ep}/\gamma_u \sim \left(\frac{T^3 \Delta_{ep}}{\Delta_u^4}\right)^{\frac{1-K_{c+}}{2}}$. The phonon assisted decay is dominant in the wide range of temperatures, $T > (\Delta_u^4/\Delta_{ep})^{1/3}$. With the exception of the region of very low temperatures it is dominated by electron-phonon scattering and scales as $T^{(1+K_{c+})/2}$. This is consistent with the temperature dependence of phonon-induced resistivity [13].

Chapter 4

QUANTUM CRITICALITY IN AN ARMCHAIR CARBON NANOTUBE PN JUNCTION

4.1 Introduction

In this chapter, we study the electron transport through a non uniformly doped armchair carbon nanotube, more specifically a pn junction in a clean CNT. The pn junction can be formed by applying a non uniform gate voltage to the carbon nanotube. We will show that the transport in such a structure manifests a quantum critical behavior controlled by the built-in doping field, which makes the pn junction in an armchair CNT drastically different from a semiconductor pn junction. [52] The doping potential is assumed to be smooth so it doesn't cause single particle backscatterings. Such processes can not be induced by the e-e interactions either, due to the parity symmetry we discussed in the previous chapters. Yet the pair backscatterings or Umklapp processes are present due to the e-e interaction. In a CNT pn junction, the Umklapp processes occur only at the central region of the junction due to momentum conservation. The width of the central region is controlled by the doping field E. When E is strong the width is narrow and the Umklapp processes are irrelevant. In this case electrons have perfect transmission at zero temperature. When E is weak, the Umklapp processes become relevant and pn junction becomes an insulator at zero temperature. The existence of two stable fixed points at zero temperature indicates the existence of an unstable intermediate fixed point of the conductance at certain E and a quantum phase transition tuned by the doping field. The backscattering assisted by e-phonon interaction will not destroy this phase transition because of its irrelevance at low temperature. This feature makes a CNT pn junction drastically

different from either a simple barrier in Luttinger liquid or an ordinary band pn junction. The former results in an insulator at zero temperature however weak is the barrier. The latter has a tunneling conductance which obeys the exponential law and also results in an insulator at zero temperature.

The transport near the two stable fixed points of the conductance can be studied by perturbation theory because near perfect transmission, the backscattering correction is small and near the insulating phase the tunneling amplitude is small. Yet near the intermediate fixed point neither of them is small. To approach the physics near this critical point, we apply an epsilon expansion of the RG equations of the interaction strength treating the scalings of Umklapp interaction in the pn junction and its generalized higher order term as small parameters. The values of the conductance and critical index at the intermediate fixed point are obtained from the RG equations.

This chapter is organized as follows: In Sec. 4.2, we study the transport in the weak backscattering and weak tunneling cases respectively and indicate the existence of quantum phase transition and intermediate fixed point. In Sec. 4.3, we examine the physics at the intermediate fixed point using epsilon expansion. In Sec. 4.4, we study the effect of e-phonon interaction and magnetic field on the phase transition. We will show that the e-phonon interaction doesn't destroy the quantum phase transition due to the Umklapp processes, yet the magnetic field induces single particle backscatterings which drive the pn junction to an insulator at zero temperature and destroy the quantum phase transition. In the last section, we briefly summarize the chapter.

4.2 Perturbation theory of the transport through an armchair CNT pn junction and quantum phase transition

We consider a single pn-junction that is formed by a static potential $U(x)$ imposed by two gates, as in Fig. 4.1(b). In the p- and n- regions $U(x)$ saturates to $\pm U_0$, while near the center of the pn-junction $U(x) \approx eEx$, where $-e$ is the electron charge and

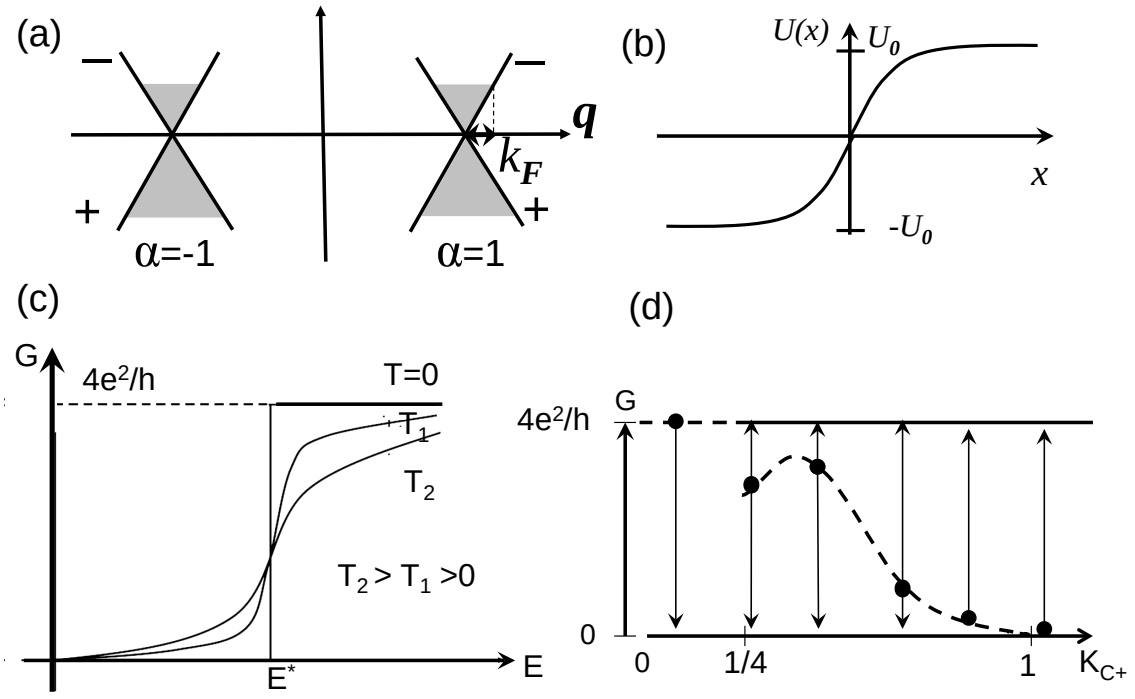

Figure 4.1: (a) Electron spectrum near the Dirac points $\alpha = \pm 1$ (+ or − indicates parity). (b) Near $x = 0$ the gate potential is $U(x) \approx -eEx$ and saturates to $\pm U_0$ in the p- and n- regions. (c) Schematic picture of the conductance dependence on E at different temperatures. The $G(E)$ curves at different temperatures intersect at the fixed point and increase monotonically with E. The step in $G(E)$ at $T = 0$, indicates a quantum phase transition. (d) RG flow for the conductance.

E is the built-in electric field. If the gate potential is not too strong, $|U_0| \ll v_F/R$, where R is the CNT radius (we set $\hbar = 1$ in the intermediate formulas), the pn-junction may be modeled using the low energy CNT band structure shown in Fig. 4.1 (a). We assume that $U(x)$ is smooth on the interatomic scale and does not break the symmetry between the A and B sublattices. Then both inter- and intra-valley backscatterings due to $U(x)$ are absent, and we may write the noninteracting part of the electron Hamiltonian as

$$H_0 = \sum_{\alpha r\sigma} \int dx\, \psi^+_{\alpha r\sigma}(x)\left[-i\, r\, v_F \partial_x + U(x)\right] \psi_{\alpha r\sigma}(x). \tag{4.1}$$

Here $v_F \approx 8 * 10^5$ m/s is the Fermi velocity, $\alpha = \pm$ is the valley index, $r = \pm 1$ labels left and right movers, and σ the electron spin.

The gate potential $U(x)$ results in a position-dependent doping density characterized by the Fermi wave vector $k_F(x) \sim -U(x)/v_F$. The potential field $U(x)$ could be eliminated from Eq.(4.1) by a gauge transformation $\psi(x) \to \psi'(x)e^{-i\ r\int U(x)dx/v_F}$, or equivalently we can add this factor to the standard bosonization procedure [24]

$$\psi_{\alpha r\sigma}(x) = \frac{F_{\alpha\sigma}}{\sqrt{2\pi\xi}}\, e^{ir\left[\int^x k_F(x')dx' - \Phi_{\alpha\sigma}(x)\right] + i\Theta_{\alpha\sigma}(x)}. \tag{4.2}$$

Here $\xi \sim R$ is the short distance cutoff, $F_{\alpha\sigma}$ are Klein factors. The bosonic fields Φ and Θ obey the standard commutation relations $[\Phi_{\alpha\sigma}(x), \Theta_{\alpha'\sigma'}(x')] = -i\pi\delta_{\alpha\alpha'}\delta_{\sigma\sigma'}\theta(x-x')$.

We assume that the number of unit cells N around the circumference of an (N, N) armchair CNT is large. The backscattering strength of Coulomb interaction is small in $1/N$ [23]. The forward scattering part of the e-e interactions is,

$$V_f = \frac{V(0)}{2} \int dx n^2(x); \;\; n(x) = \sum_{\alpha r\sigma} \psi^+_{\alpha r\sigma}(x)\psi_{\alpha r\sigma}(x). \tag{4.3}$$

Here $V(0) \approx 2e^2 \ln(d/R)$ is the forward scattering matrix element (we assume that the Coulomb interaction is screened by the gate at a distance d from the CNT).

In the bosonic representation the electron density is $n(x) = 4k_F(x)/\pi - \sum_{\alpha\sigma} \partial_x \Phi_{\alpha\sigma}(x)/\pi$, where k_F is counted from the Dirac point. After abandoning the static electric energy due to the average charge density $4k_F(x)/\pi$, the forward scattering part of the

Hamiltonian $H_f \equiv H_0 + V_f$ reduces to the same form as in an undoped CNT

$$H_f = \int \frac{dx}{2\pi} \sum_j u_j \left[K_j (\partial_x \Theta_j)^2 + (\partial_x \Phi_j)^2 / K_j \right]. \tag{4.4}$$

Here $j = c\pm, s\pm$ labels charge (c) and spin (s) modes that are symmetric ($+$) or antisymmetric ($-$) in the valley index α. They are related to the fields $\Phi_{\alpha\sigma}$ by $\Phi_{\alpha\sigma} = \left[\Phi_{c+} + \alpha\Phi_{c-} + \sigma\Phi_{s+} + \alpha\sigma\Phi_{s-}\right]/2$. Only the $c+$ mode carries charge and the other three are neutral. The mode velocities are $u_j = v_F/K_j$, where the Luttinger parameters are $K_{c+} = 1/\sqrt{1 + 4V(0)/\pi v_F} \ll 1$ and $K_j = 1$ for the neutral modes.

As discussed in Chapter 2, backscattering interactions are small in $1/N$ [23], and may be treated as perturbations to the Hamiltonian (4.4). The most relevant backscattering interaction corresponds to the Umklapp processes, which scatter two right-movers into left-moving states or vice-versa [15, 16]. In the presence of doping the Umklapp Hamiltonian can be written as

$$\begin{aligned} H_U \;=\; & -\int \frac{dx}{2(\pi\xi)^2} \cos\left(2\Phi_{c+}(x) - 4\int_0^x k_F(y)dy\right) \times \\ & \{g_3 \cos[2\Theta_{s-}(x)] + (g_3 - g_1)\cos[2\Phi_{s+}(x)] \\ & + g_1(\cos[2\Phi_{c-}(x)] - \cos[2\Phi_{s-}(x)])\}. \end{aligned} \tag{4.5}$$

Here the coupling constants g_1 and g_3 are of order e^2/N and $g_3 > g_1$ as discussed in the last chapter. The low energy electron Hamiltonian of the pn-junction is given by the sum of Eqs. (4.4) and (4.5),

$$H = H_f + H_U. \tag{4.6}$$

The position-dependent Fermi vector $k_F(x)$ in Eq. (4.5) saturates to constant values $\pm k_0$ in the deep n- and p- regions whereas near $x = 0$ it has a linear dependence of x,

$$k_F(x) = -x/L_E^2. \tag{4.7}$$

Here the length scale L_E is defined by the built-in electric field E controlled by the gate voltages, $L_E \sim \sqrt{v_F/eE}$. We assume in the experiments, the maximum doping

potential U_0 far exceeds the temperature. In this case we will show that only the center region with length T/E contributes significantly to the resistence so we could extend the linear dependence of k_F to the whole device in the model and the physics will not be affected.

The dc current in a 1D system is uniform in space, and the nonlocal conductivity $\sigma_\omega(x, x')$ varies slowly within the length scale $\min\{\lambda, l\}$, where λ is the plasmon wavelength and l is the mean free path. In the dc limit and in a clean tube, $\min\{\lambda, l\}$ is much larger than the length scale of the tube so one gets

$$j_\omega \approx \sigma_\omega(0,0) \int dx' E(x') = GV \tag{4.8}$$

where $G = \sigma_\omega(0,0)$ is the conductance of the wire and $\sigma_\omega(x, x')$ can be expressed by the usual Kubo formula as

$$\sigma_\omega(x, x') = \frac{e^2}{\omega} \int_0^\infty dt\, e^{i\omega t} \langle [j(x,t), j(x',0)] \rangle \tag{4.9}$$

The current operator is related to the charge field as $j = -2e\partial_t \Phi_{c+}(x = 0, t)/\pi$ so

$$\sigma_\omega(x, x') = 4e^2 \frac{i\omega}{\pi^2} \mathcal{G}^R_\omega(x, x') \tag{4.10}$$

where $\mathcal{G}^0_\omega(x, x') = -i \int_0^\infty dt\, e^{i\omega t} \langle [\Phi_{c+}(x,t), \Phi_{c+}(x',0)] \rangle$ is the retarded Green's function (GF) of the $c+$ mode.

In the absence of Umklapp interactions evaluation of the Green's function in a Uniform CNT is straightforward and gives

$$\mathcal{G}^0_\omega(x, x') = -i\pi (K_{c+}/2\omega_+)\, e^{i\omega_+ |x-x'|/u_{c+}}, \tag{4.11}$$

where $\omega_+ = \omega + i\eta$. In a CNT pn junction, the shift of Bosonic field Φ_{c+} to $\Phi_{c+} + 2\int k_F(x)dx$ doesn't affect the current since $2\int k_F(x)dx$ is static. For the two terminal device, there are two boundaries with the leads. Here we assume that the connection to the leads is adiabatic, i.e., electrons enter the leads from the tube without backscattering at the boundaries. In the absence of Umklapp interactions,

the Green's function $\mathcal{G}^0_\omega(x-x')$ of the setup with two boundaries was solved in the last Chapter and in the dc limit, we got $\mathcal{G}^0_{\omega\to 0}(0,0) = -i\pi(1/2\omega_+)$ which is to replace K_{c+} in Eq.(4.11) by 1. The reason is that in the dc limit, the Bosonic modes have wavelengths much larger than the length of the tube and extend to the leads, where LL effects are absent. Thus the Luttinger parameter K_{c+} should be set to unity when evaluating $\mathcal{G}(0,0)$ [44], yielding $G_0 = 4e^2/h$, which is the same as the conductance for the non-interacting case, that is to say, the forward scattering due to e-e interaction doesn't modify the conductance of the two terminal device.

The Umklapp processes degrade electric current by backscattering pairs of electrons and thus decrease the device conductance. They are most effective near the zero doping point $x = 0$ and strongly suppressed deep in the p- and n- regions. In the deep p and n region where $v_F k_0 \gg T$, the Umklapp backscatterings in the p- and n- regions result in exponentially small resistivity $\sim \exp(-2v_F k_0/T)$ as shown in the last chapter. We assume that the lengths of the p- and n- regions are not sufficient to compensate for this exponential smallness and neglect this contribution. In this approximation the main contribution of the backscattering arises from the spatial region $|x| \le T/eE$, where $|k_F(x)| \le T/v_F$. We assume $T \ll U_0$ in the experiment then the spatial dependence of $k_F(x)$ in the region $|x| \le T/eE$ is linear. Therefore the pn-junction may be modeled by the Hamiltonian (4.6) with $k_F(x)$ given by Eq. (4.7) in the entire space.

The Green's function with interaction can be expressed as,

$$\mathcal{G}_\omega(0,0) = \mathcal{G}^0_\omega(0,0) + \int_{-\infty}^{\infty} dx dx' \mathcal{G}^0_\omega(0,x) T_\omega(x,x') \mathcal{G}^0_\omega(x',0). \tag{4.12}$$

Here $T_\omega(x,x')$ is the part of the T-matrix that corresponds to scattering of a plasmon into neutral modes. Using Wick's theorem (c.f. Appendix B) one can show that in

the lowest order of interaction it can be expressed as

$$T_\omega(x,x') = -ia_\eta^2 \int dt \left[e^{i\omega t} \langle [\mathcal{H}_\eta(x,t), \mathcal{H}_\eta(x',0)] \rangle_0 - \int_0^L d\xi \langle [\mathcal{H}_\eta(x,t), \mathcal{H}_\eta(\xi,0)] \rangle_0 \delta(x-x') \right]. \quad (4.13)$$

where $\mathcal{H}_\eta(x,t)$ is the interaction Hamiltonian density and a_η is the coefficient in the exponential of the Hamiltonian. For Umklapp interaction, $a_\eta = 2$.

The correlation function of the Umklapp interaction Hamiltonian density H_U decays exponentially with decay length $L_T = v_F/T$ as shown in last chapter, which is much less than the plasmon wavelength, so we can express the Green's function of the charge mode as

$$\mathcal{G}_\omega(0,0) = \mathcal{G}^0_\omega(0,0) + \mathcal{G}^0_\omega(0,0) \int_{-\infty}^{\infty} dx dx' T_\omega(x,x') \mathcal{G}^0_\omega(0,0). \quad (4.14)$$

In the dc limit the unperturbed Green's functions $\mathcal{G}^0_\omega$ in Eq. (4.14) are given by Eq. (4.11) with $K_{c+} = 1$. Then the deviation δG of the device conductance from the ideal value, $4e^2/h$, may be expressed as

$$\delta G = -i \frac{e^2}{h} \lim_{\omega \to 0} \frac{2\pi}{\omega} \int_{-\infty}^{\infty} dx\, dx' T_\omega(x,x'). \quad (4.15)$$

The T-matrix properties are dominated by the fluctuations of bosonic modes with frequencies on the order of the temperature T and characteristic spatial scale of $L_T \sim v_F/T$. Provided the device length is much longer than L_T, the boundary of the device is not important and the correlation function of the T-matrix can be replaced by the corresponding correlator of a homogenous tube.

The energy gap $\Delta \sim (v_F/\xi)(g_3/v_F)^{1-K_{c+}}$ [15] induced by the Umklapp interaction in a uniform CNT at zero doping defines an additional characteristic length scale, $\zeta = v_F/\Delta$. The Umklapp coupling constants renormalize to the order of magnitude 1 at length scale ζ, so backscattering at the pn-junction is weak for $L_E \ll \zeta$ and strong for $L_E \gg \zeta$.

For $L_E \ll \zeta$ the correction to the ideal conductance may be expanded in perturbation series in H_U, Eq. (4.5). Using Eqs. (4.16), (4.13) we get to second order in H_U, the correction to the conductance is

$$\begin{aligned}\delta G^{(2)} &= -i\frac{e^2}{h}\lim_{\omega\to 0}\frac{2\pi}{\omega}\int_{-\infty}^{\infty} dx\, dx' T_\omega(x,x') \\ &= -\frac{e^2}{h}\lim_{\omega\to 0}\frac{8\pi}{\omega}\int_0^{\infty} d\tau (e^{i\omega\tau}-1)\langle H_U(\tau)H_U(0)\rangle \\ &= -c\,(2\pi T\xi/u_{c+})^{2K_{c+}}(L_E/\xi)^2(3g_1^2-2g_1g_3+2g_3^2)/v_F^2 \qquad (4.16)\end{aligned}$$

where $c = (e^2/h)B(K_{c+}+1, K_{c+}+1)/2\pi$, with $B(x,y)$ being the Euler Beta function. This result may be rewritten as $\delta G^{(2)} \sim (e^2/h)(L_E/\zeta)^2(T/\Delta)^{2K_{c+}}$. It vanishes as $T \to 0$, which corresponds to the irrelevance of point-like Umklapp scatterings in the renormalization group (RG) sense.

Although higher order terms in the perturbation theory are smaller in powers of L_E/ζ they have different temperature dependence. All higher order corrections are less relevant than the second order one above except for a fourth order term. The fourth order perturbation of Umklapp interaction can generate a backscattering process with effective Hamiltonian density

$$\mathcal{H}_4 = \frac{g_4}{2(\pi\xi)^2}\cos(4\Phi_{c+}) \qquad (4.17)$$

The correction to the conductance due to this term can be obtained following the same procedure as for the Umklapp term and is $\delta G^{(4)} \sim -(e^2/h)(L_E/\zeta)^4(T/\Delta)^{8K_{c+}-2}$. In the case $K_{c+} > 1/4$, this correction is irrelevant and the CNT is still a perfect conductor at $T = 0$. In the case $K_{c+} < 1/4$, the above term becomes relevant and results in an insulator at $T = 0$. The RG fixed point (FP) at perfect transmission is unstable in this regime, and the system flows to strong backscattering even at $L_E \ll \zeta$. The expected RG flow is shown in Fig. 4.1(d). We note that in this case the temperature dependence of conductance is nonmonotonic. In the regime of the applicability of the perturbation theory $\delta G = -a\,(L_E/\zeta)^2\,(T/\Delta)^{2K_{c+}} - b\,(L_E/\zeta)^4\,(T/\Delta)^{8K_{c+}-2}$, where a

and b are constants on the order of e^2/h. The maximum conductance is reached at $T \sim \Delta\,(L_E/\zeta)^{1/(1-3K_{c+})}$.

Because of the large value of the interaction constant, $e^2/v_F \approx 2.7$ and the sensitivity of the forward scattering matrix element $V(0)$ to screening by the gates both cases $K_{c+} < 1/4$ and $K_{c+} > 1/4$ may be realized.

For $K_{c+} > 1/4$ all backscattering operators generated in the process of renormalization are irrelevant by perturbation theory. Therefore the FP at perfect transmission is stable for weak backscattering, $L_E \ll \zeta$. At the same time, the analysis below shows that a perfect reflection fixed point is stable at $K_{c+} < 1$ at strong backscattering, i.e.,for $L_E \gg \zeta$. This indicates the existence at $1/4 < K_{c+} < 1$ of a quantum phase transition in the conductance of pn-junction, controlled by the ratio L_E/ζ.

At strong backscattering, $L_E \gg \zeta$, the pn-junction may be viewed as two semi-infinite Luttinger liquids separated by a strong barrier where the bosonic fields are pinned to one of the classical minima of the Umklapp Hamiltonian at zero temperature. The minima form a periodic lattice in the four-dimensional space $\Phi_j = \pi n_j/2$, where n_j are integers, which are either all even or all odd. At zero temperature, no current could pass by. At finite temperature, the Bosonic fields could tunnel from one minimum to another, which corresponds to charge transport from the p region to the n region or vice versa. The most relevant tunneling events are those between the nearest neighboring minima, e.g., from $(\Phi_{c+}, \Phi_{c-}, \Phi_{s+}, \Phi_{s-}) = (\frac{\pi}{2}, \frac{\pi}{2}, \frac{\pi}{2}, \frac{\pi}{2})$ to $(\Phi_{c+}, \Phi_{c-}, \Phi_{s+}, \Phi_{s-}) = (0, 0, 0, 0)$ which transfer charge e from the left side to the right side of the pn junction or vice versa. The tunneling operator corresponding to the shift $\{n_j\} \to \{n_i + \delta n_j\}$ is $\exp\{i \sum_j [\theta_j(x_1) - \theta_j(x_2)]\delta n_j/2\}$, where x_1 and x_2 label the points just to the left and to the right of the barrier. At the boundary of a semi-infinite Luttinger liquid the correlation function $\langle e^{i\theta_j(x,\tau_1)/2} e^{-i\theta_j(x,\tau_2)/2}\rangle \sim (\frac{1}{\tau_1-\tau_2})^{1/4K_j}$ and $\langle e^{i\Phi_j(x,\tau_1)/2} e^{-i\Phi_j(x,\tau_2)/2}\rangle \sim (\frac{1}{\tau_1-\tau_2})^{K_j/4}$. [24] The scaling dimension of the tunneling operator is then $1 - \sum_j (\delta n_j)^2/(4K_j)$. For $K_{c+} < 1$ all of them are irrelevant. A phenomenological Hamiltonian corresponding to the tunneling between nearest neighbor

minimum can be written as

$$H_t = \frac{v_F}{\xi} t_1 \prod_{j=c\pm,s\pm} [e^{i(\theta_j(x_2)-\theta_j(x_1))/2} + h.c.] \tag{4.18}$$

The bare tunneling amplitude $t_1 \sim e^{-L_E/\zeta}$. The scaling dimension of this tunneling Hamiltonian is $\frac{1}{4}\sum_j(1-\frac{1}{K_j})$, which gives the lowest order RG equation of the tunneling amplitude as

$$\frac{dt_1}{dl} = \frac{1}{4}\sum_j (1-\frac{1}{K_j}) t_1. \tag{4.19}$$

Since $K_j < 1$, the tunneling is irrelevant and flows to a stable fixed point $t_1 = 0$ at zero temperature. At finite T, we stop the flow when the energy cutoff is of the order of the temperature and obtain the conductance as

$$G \sim \frac{e^2}{h} t_1^2(l^*) \sim \frac{e^2}{h} t_1^2 (\frac{u}{\xi T})^{\frac{1}{2}\sum_j (1-\frac{1}{K_j})}. \tag{4.20}$$

which vanishes at $T = 0$ and results in an insulator.

The stable FPs at perfect transmission and reflection for $1/4 < K_{c+} < 1$ must be separated by an unstable FP with an intermediate value of zero temperature conductance. The pn-junction can be tuned to this FP by adjusting the parameter L_E. The dependence of conductance on L_E at low temperature is schematically presented in Fig. 4.1(c). The critical conductance and critical exponents at the intermediate fixed point depend on the values of the Luttinger parameters K_j.

4.3 Epsilon expansion approach near the intermediate fixed point

The behavior near the intermediate fixed point is hard to approach in general because there is no small physical parameter there. Yet in some special situation, a small parameter exists and we can access the intermediate fixed point perturbatively. Near $K_{c+} = 1/4$ we note that the two most relevant backscattering operators, i.e. the Umklapp operator in Eq.(4.5) and Eq.(4.17): H_4 and H_U, both have scaling dimensions that are reasonably small (respective scaling dimensions $4K_{c+} - 1$ and K_{c+}).

All other operators are strongly irrelevant. Near this point one can use a kind of ϵ-expansion to obtain the RG equations in which both $\epsilon = K_{c+}$ and $\epsilon_4 = K_{c+} - 1/4$ are assumed small. In this case the intermediate FP is perturbatively accessible.

Since in this case the backscatterings are irrelevant, which corresponds to narrow pn junction, the Bosonic fields in the pn junction are uniform in the central region and the effective pinning Hamiltonian can be written as $H_{eff} = \Lambda[r_4 \cos(4\Phi_{c+}) + \cos(2\Phi_{c+}) \sum_a r_a \cos(2\Phi_a)]$, where $\Lambda = v_F/\xi$ is the high energy cutoff, r_4, r_a are dimensionless amplitudes and a labels the neutral modes. The RG equations can be obtained by the real-space perturbation method invented by Anderson, Yuval and Hamann. This procedure involves first integrating out closely spaced dipole charges separated by a distance between τ_c and $\tau_c + d\tau_c$, where τ_c is the short distance cutoff in time domain. Then rescale $\tau_c + d\tau_c$ to restore the original cutoff. As shown in the Appendix, we obtain the RG equations to leading order in ϵ, ϵ_4 as

$$dr_a/dl = -\epsilon\, r_a + r_a r_4, \tag{4.21a}$$

$$dr_4/dl = -4\epsilon_4 r_4 + \sum_a r_a^2/4, \tag{4.21b}$$

where $dl \equiv d\tau_c/\tau_c$. The intermediate FP exists for $\epsilon_4 > 0$ and is located at $r_4^* = \epsilon$ and $\sum_a r_a^{*2} = 16\epsilon_4\epsilon$ when the right hand side of the RG equations equals to zero. The FP conductance can be found by using lowest order perturbation theory shown in the last section with FP values of the reflection amplitudes [55], and is obtained to be $G^* = 4(e^2/h)(1 - \epsilon_4 - \epsilon^2/32\epsilon_4)$. The presence of the ϵ_4 in the denominator in the last term signals that Eq. (4.21) is valid provided $\epsilon_4 \gg \epsilon^2$.

To get the critical index near the critical point, we linearize the RG equations near the fixed point and get

$$\frac{d\delta(\sum_a r_a^2)}{dl} = \sum_a (r_a^2)^* \delta r_4$$

$$\frac{d\delta r_4}{dl} = -4\epsilon_4 \delta r_4 + \delta(\sum_a r_a^2)/4, \tag{4.22}$$

The eigenvalues λ_i of the above linearized equations are $\lambda_\pm = -2\epsilon_4 \pm 2\sqrt{\epsilon_4^2 + 2\epsilon\epsilon_4}$, which correspond to the scaling dimension of backscattering amplitude near the fixed point. The positive eigenvalue describes the behavior of a scaling field that's unstable near the fixed point, whereas the negative eigenvalue describes a stable scaling field near the fixed point. In the system we study, by this analysis, the positive eigenvalue is the one that describes the critical behavior of conductance near the intermediate fixed point. At finite temperature, T serves as the low energy cutoff, which is related to the long distance cutoff by $T = v_F/L$. By setting $e^l = v_F/T\xi$, we bring the high energy cutoff down to the value T and get the renormalized backscattering amplitude at temperature T as $r - r^* \sim (\frac{v_F}{T\xi})^{\lambda_+}$. The conductance is related to the backscattering amplitude as $G - G_0 \sim r^2$, so the critical index of G on temperature is the same as r. Near the FP we thus obtain that the conductance behaves as $G(T) - G^* \sim (e^2/h)(1 - L_E/L_E^*)(\hbar v_F/T\xi)^{\lambda_+}$ where $\lambda_+ = -2\epsilon_4 + 2\sqrt{\epsilon_4^2 + 2\epsilon\epsilon_4}$.

Similarly, the intermediate fixed point is also perturbatively accessible near the point $K_j = 1$ where the single electron tunneling process is marginal, by performing the RG equations of the tunneling amplitudes to higher order. Yet near $K_j = 1$, the following tunneling processes are also marginal and will renormalize the single electron tunneling process,

$$H_j = \frac{v_F}{\alpha} t_j [e^{i(\theta_j(x_2) - \theta_j(x_1))} + h.c.] \tag{4.23}$$

Here j includes all the four bosonic modes. The Hamiltonian H_{c+} describes two-charge tunneling process while the other three Hamiltonians describe tunneling of neutral modes. Near $K_j = 1$, we obtain the RG equations of the tunneling amplitudes to second order as

$$\begin{aligned} \frac{dt_1}{dl} &= -\sum_j \frac{\epsilon_j}{4} t_1 + 2\sum_j t_1 t_j \\ \frac{dt_j}{dl} &= -\epsilon_j t_j + 2t_1^2 \end{aligned} \tag{4.24}$$

following the same method in Appendix A, where $\epsilon_j \equiv 1 - K_j$. These RG equations

exhibit a fixed point at $t_1^* = \sqrt{\frac{\sum_j \epsilon_j}{16 \sum_j \frac{1}{\epsilon_j}}}$ and $t_j^* = \frac{1}{8\epsilon_j} \frac{\sum_j \epsilon_j}{\sum_j \frac{1}{\epsilon_j}}$. The conductance at the fixed point $G^* = \frac{e^2}{h}(t_1^{*2} + 4t_{c+}^{*2})$ is universal and separates the flow to the two stable phases, as shown in Fig.1(c) and (d). The critical exponent of the conductance near the fixed point can be extracted from the one relevant eigendirection at the critical fixed point as $G - G^* \sim (\frac{v_F}{T\xi})^{\lambda_+}$, where λ_+ is the one positive eigenvalue of the linearized RG equations near the fixed point. The eigenvalue equation for the above flows is in general fifth order and hard to solve analytically, but in the case K_j are the same for the four modes, $\lambda_+ = \epsilon_j$.

Interpolation between the two limiting cases above gives the RG flow shown in Fig. 4.1(d).

4.4 The role of e-phonon interaction and magnetic field

The above picture is modified if single-electron backscattering is present. In a symmetric armchair CNT it can be caused by a magnetic field B applied along the CNT axis or by the electron-phonon (ep) interactions. The corresponding backscattering Hamiltonian may be written as [57, 49, 48]

$$\delta H = -i \int dx \sum_{\alpha r \sigma} \psi^\dagger_{\alpha r \sigma}(x) \psi_{\alpha -r \sigma} r[\alpha \Delta_u(x) + \Delta_B], \tag{4.25}$$

where Δ_B and Δ_u are respectively the gaps induced in the single particle spectrum by the magnetic field, $\Delta_B = (\pi/2) eB v_F R$, and by the lattice deformation. At low temperatures only the twist acoustic (TA) phonons are important and $\Delta_u(x) = g_T \partial_x u(x)$, where $u(x)$ is the TA mode displacement and $g_T \sim 1/\sqrt{N} \ll 1$ is the corresponding coupling constant. The bosonized form of the e-phonon Hamiltonian is shown in Chapter 2, Eq.(2.31). As in the case of two-particle processes, single electron backscattering is effective only in the vicinity of the pn-junction, $|x| \lesssim L_E$. The leading perturbative correction to the conductance due to the e-TA phonon backscattering is given by $\delta \mathrm{Re} G_{ep} \sim -\frac{g_T^2}{E} T^{\frac{3}{2} + \frac{K_{c+}}{2}}$ in a strong field E and $\sim -g_T^2 T^{\frac{1}{2} + \frac{K_{c+}}{2}}$ in a weak field E, following the same steps as for perturbative Umklapp correction. In

both cases, the conductance corrections are irrelevant and vanish at $T = 0$. Thus the e-phonon interaction doesn't destroy the quantum phase transition due to the Umklapp processes.

When a magnetic field is applied along the tube axis, however, the above quantum phase transition will be destroyed. The magnetic field causes intravalley single particle backscattering with Hamiltonian [57]

$$H_B = \Delta_B \sum_{\alpha,\sigma} \int dx(\psi^+_{\alpha L\sigma}\psi_{\alpha R\sigma} + h.c.) = \frac{\Delta_B}{2\pi\xi} \sum_{\alpha,\sigma} \int dx \cos\Phi_{\alpha\sigma} \tag{4.26}$$

where $\Delta_B = \frac{\hbar v_F}{R}\frac{\pi R^2 B}{\Phi_0}$ is the gap opened by the magnetic field in a uniform CNT. When the applied magnetic field is weak and the tilting field E is strong, the perturbative correction to the conductance due to the magnetic field, or the magnetoconductance, is given by $\delta \mathrm{Re} G_h \sim -\frac{e^2}{h}(\frac{E_F}{T})^{\frac{1-K_{c+}}{2}}\frac{\Delta_B^2}{v_F E}$ and relevant. At a weak tilting field, the correction is even more relevant. Thus at any field E, the magnetic field drives the conductance to zero at $T = 0$ and the quantum phase transition is destroyed. This also reveals that magnetoresistance of a CNT pn-junction is strongly enhanced by the Luttinger liquid effects.

4.5 Conclusion

In conclusion, we studied the electron transport in an armchair CNT pn junction formed by a tilting field E. Without e-e backscattering, the two terminal conductance has perfect value $4e^2/h$. However this value is corrected by backscattering. In a strong tilting field E, the correction due to Umklapp processes is irrelevant for $K_{c+} > 1/4$, resulting in perfect transmission at $T = 0$; and relevant for $K_{c+} < 1/4$, resulting in an insulator at $T = 0$. While in a weak tilting field E, the correction is relevant for any $0 < K_{c+} < 1$ and the current is totally blocked at zero temperature. A quantum phase transition thus happens by tuning the tilting field E in the case $1/4 < K_{c+} < 1$. The existence of the two stable phases at $T = 0$ and $1/4 < K_{c+} < 1$ corresponding to high and low tilting field E suggests an unstable fixed point of the conductance at a

finite value G^*. The intermediate fixed point is perturbatively accessible by an epsilon expansion near the two special cases $K_{c+} \sim 1/4$ and $K_{c+} \sim 1$. The conductance and critical index at the intermediate fixed point is universal and only depends on K_{c+}. The quantum phase transition will not be destroyed by e-phonon backscattering at any field E. However, a magnetic field along the tube axis will drive the conductance to zero at $T = 0$ at any tilting field E and destroy the possible quantum phase transition at zero magnetic field.

Chapter 5

TRANSPORT OF MOLECULE DEVICES WITH GRAPHENE LEADS

5.1 Introduction

The efforts to miniaturize electronic devices have long motivated studies of electron transport in molecular and atomic scale devices. Creating reliable electrical contacts with the molecule presents a major challenge in molecular electronics. Until recently, in molecular electronic devices the molecule was typically attached between two normal metal electrodes, such as gold. [60, 61, 62, 63, 64, 65].

Carbon-based conductors have long been expected to be promising components of electronic devices [66]. Apart from bulk graphite there are also quasi-one dimensional (carbon nanotubes [67]) and two-dimensional (graphene [68]) forms, which have remarkable mechanical and electrical properties. This offers the prospect of building entire electronic devices or circuits out of carbon-based materials. Remarkably, formation of single atom carbon chains (SACCs) between graphene electrodes fabricated by stretching a graphene strip has been observed in Ref. [74]. Such a structure could form a basic unit for integration into more complicated circuits in the future.

In this chapter we study the electron transport through such a structure as shown in Fig5.1 in the non-interacting electron approximation by an analytically solvable model and claim that the major feature of electron transport of such a device could be generalized to other molecular devices with graphene leads too.

We found that the conductance of the system is qualitatively different from that in the case of metal leads. For all electron energies corresponding to practically relevant temperatures and doping levels the junction between the chain and the graphene lead

is almost perfectly reflecting even at strong coupling between the chain and the lead. The transmission coefficient of the contact vanishes linearly with electron energy as the latter approaches the Fermi energy of undoped graphene. This suppression of transmission results from the vanishing of density of states (DoS) in graphene at zero doping. Even though edge states can appear in graphene leads and the edge states have a linear dispersion relation, their wave functions extend into the bulk to distances inversely proportional to the energy and give a linearly vanishing local density of states at the contact point. The whole device behaves like a Fabry-Perot interferometer and electrons get through the device only through narrow resonance states with certain energy, due to the strong reflection at the junctions. The width and the position of the resonances depend on the length of the interconnect and the details of its coupling to the leads. The shape of low energy resonances is universal but markedly different from the Breit-Wigner form, which is the typical case for molecular devices with metallic leads.

Due to the resonant character of transmission the device conductance is very sensitive to the number of atoms in the chain. The conductance difference between chains with odd and even number of atoms in the SACC appears as the difference between the on- and off- state of the device, which suggests that they can be components of atomic scale transistors.

The chapter is organized as follows. In Sec. 5.2 we qualitatively discuss the essential features of electron transport in SACC interconnects between graphene leads. In Sec. 5.3 we formulate an analytically solvable model of electron dynamics in the system. In Sec. 5.3.1 we derive a general formula for the reflection amplitude of the junction between the chain and the lead in terms of the electron Green function (GF) of the lead. In Sec. 5.3.2 we evaluate the GF and study the tunneling density of states at the junction due to the bulk and edge electron states in the lead. In sec. 5.4 we evaluate the transmission coefficient of the device and obtain the universal formula for the resonance shape. We discuss our results and experimental implications in

Sec. 5.5.

5.2 Qualitative discussion

First we discuss the possible ground state of the SACC. As a first step study of the device, we consider the non-interacting picture. As shown in Chapter 2, Coulomb interaction could destroy the non-interacting ground state of a 1D single atom chain in an infinite system, but in experiments, when the length of the chain is short, the interaction is not essential and the system can still be described by the non-interacting picture.

As we know, in a single carbon atom chain, two of the four valence electrons fill the sp hybridized orbits and form σ bands with neighboring sp hybridized electrons. The two lower σ bands are then fully occupied. The remaining two p orbital electrons in each atom form two half filled π bands which are conducting. The two bands are degenerate and have angular momenta ± 1 about the molecule axis. This symmetry prohibits the Jahn-Teller instability which mixes the two orbits by a distortion with respect to the symmetry axis and lower the energy. Another possible distortion is the dimerization along the molecule axis due to Pierls instability, resulting in a structure as $(\cdots \mathrm{C}-\mathrm{C} \equiv \mathrm{C}-\mathrm{C} \cdots)$. Yet *Ab initio* calculations [76] show that because of large quantum fluctuations of the atomic positions, the dimerised state is unstable. Instead only the cumulene structure $(\cdots \mathrm{C}=\mathrm{C}=\mathrm{C}=\mathrm{C} \cdots)$ is stable.

As the conduction π band in graphene leads is formed by the p_z orbitals, which are perpendicular to the graphene plane, only the electrons from the p_z band in SACC can propagate into the leads. Thus electron transport is mediated by a single conducting band in the chain.

Because of the long mean free path of electrons in graphene [68], electron motion in the leads may be assumed to be ballistic. The device conductance is then determined by the elastic electron scattering at the junctions between the molecular wire and the leads and backscattering in the chain. Backscattering in the SACC due to

electron-phonon interaction corresponds to emission or absorption of phonons with a wavelength of order of the interatomic spacing and energy of the order of $10^3 K$. As a result such processes are exponentially suppressed [82, 83] even at room temperature. Although imperfections in the substrate and deviations of the atomic positions from the ideal configuration cause some backscattering of electrons in the wire, we show below that the strongest reflection of the electron wave in the chain occurs at the contact with the graphene lead.

With the aid of the Fermi's golden rule the transmission coefficient of the contact can be estimated as $\mathcal{T}_c \sim |\gamma_c|^2 \nu_w \nu_g$. Here γ_c is the tunneling matrix element that couples the last atom in the chain to the lead, ν_w is the local DoS at that atom and ν_g the DoS at the graphene atom that is connected to the chain. The local DoS in the chain is energy independent and can be estimated as $\nu_w \sim 1/\gamma_w$, where γ_w is the nearest neighbor hopping integral in the atomic wire. The DoS in graphene, on the other hand is strongly energy dependent and is of the order of $\nu_g \sim |\epsilon|/\gamma_g^2$, where γ_g is the nearest neighbor hopping integral in graphene and ϵ is the electron energy measured from the Fermi level of undoped graphene. It might seem that the presence of edge states might give rise to an energy-independent contribution to the tunneling DoS at the point. This is not true however. The wave functions of the edge states at low energies extend into the bulk to distances inversely proportional to the electron energy. As a result their contribution to the local DoS at the contact is also linear in ϵ. The edge states are analyzed in detail in section 5.3.2. Thus the transmission coefficient of the contact can be estimated as

$$\mathcal{T}_c \sim \frac{\gamma_c^2 |\epsilon|}{\gamma_w \gamma_g^2}. \tag{5.1}$$

The hopping integrals in graphene and SACC are of the same order of magnitude. Therefore at typical doping levels, $|\epsilon| \ll \gamma_g$, the transmission coefficient is small even at strong coupling between the chain and the lead, when all hopping integrals between nearest neighbor carbon atoms are of the same order, $\gamma_c \sim \gamma_w \sim \gamma_g$.

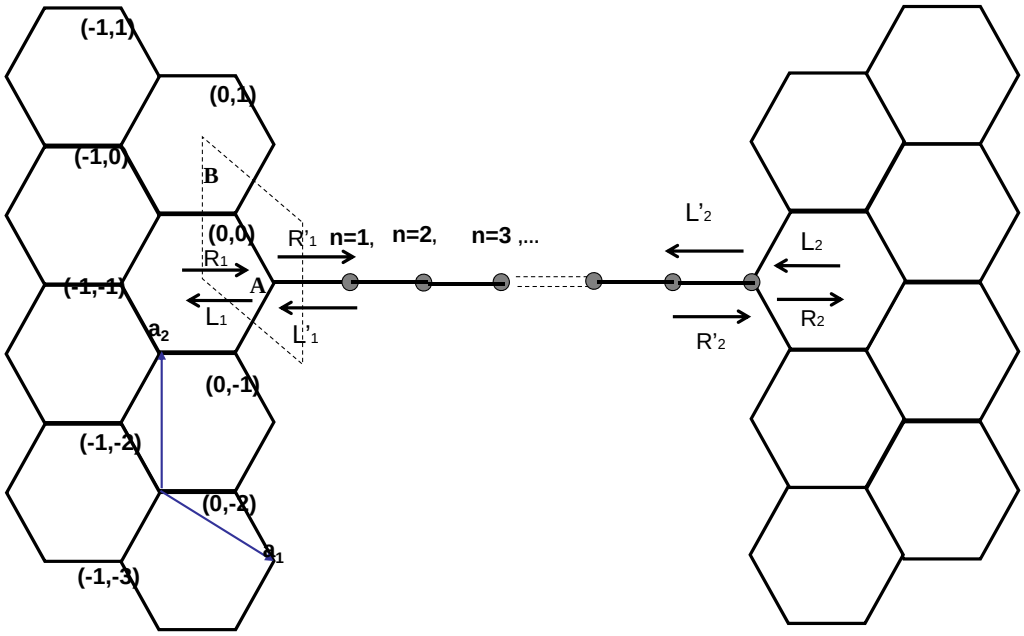

Figure 5.1: Schematic picture of the device. The atoms in the wire are labeled by $n = 1, 2, \ldots$. The unit vectors of the graphene Bravais lattice, $\mathbf{a}_1$ and $\mathbf{a}_2$, are shown by blue arrows. Each unit cell (dashed rhomboid) is labeled by (N_1, N_2).

Neglecting the weak backscattering in the wire, the transmission coefficient through the whole device can be obtained through the scattering matrix, or S matrix. Assume the reflection amplitudes at the two contacts are r_1 and r_2 respectively and the transmission amplitude t_1 and t_2 respectively. The left and right going states in the chain and leads are labeled in Fig 5.1 and they satisfy the relations:

$$\begin{pmatrix} \psi_{L_1'} \\ \psi_{R_1} \end{pmatrix} = \begin{pmatrix} t_1 & r_1' \\ r_1 & t_1' \end{pmatrix} \begin{pmatrix} \psi_{L_1} \\ \psi_{R_1'} \end{pmatrix}; \quad \begin{pmatrix} \psi_{L_2} \\ \psi_{R_2'} \end{pmatrix} = \begin{pmatrix} t_2' & r_2 \\ r_2' & t_2 \end{pmatrix} \begin{pmatrix} \psi_{L_2'} \\ \psi_{R_2} \end{pmatrix} \tag{5.2}$$

The states in the chain satisfy

$$\psi_{L_2'} = \psi_{L_1'} e^{ikL}; \quad \psi_{R_2'} = \psi_{R_1'} e^{-ikL} \tag{5.3}$$

The S matrix is unitary due to the conservation of the probability current. Without a magnetic field, S is not only unitary but also symmetric due to time reversal symmetry, i.e. $r_{1,2} = r_{1,2}'$, $t_{1,2} = t_{1,2}'$. Thus the phase of r and t satisfy $\delta(r)_{1,2} = -\delta(t)_{1,2}$. From these relations, we get

$$\psi_{L_2} = \mathcal{T}\psi_{L_1}; \quad \mathcal{T}(\epsilon) = \frac{|t_1(\epsilon)|^2 |t_2(\epsilon)|^2}{(1 - |r_1(\epsilon)||r_2(\epsilon)|)^2 + 2|r_1(\epsilon)||r_2(\epsilon)|(1 - \cos\phi)}, \tag{5.4}$$

where $\mathcal{T}(\epsilon)$ is the transmission coefficient of the device, $r_{1/2}(\epsilon) = |r_{1/2}(\epsilon)| \exp(i\delta_{1/2})$, $|t_{1/2}(\epsilon)|^2 = 1 - |r_{1/2}(\epsilon)|^2$ are the transmission coefficients of the junctions, and ϕ is the phase accumulated by an electron upon returning to the same point in the chain after being reflected from both contacts. It can be expressed as $\phi = 2k\mathcal{N} + \delta_1 + \delta_2$, where $\mathcal{N}$ is the number of atoms in the chain, k is the absolute value of the dimensionless (measured in units of the inverse lattice spacing d of the chain) electron quasimomentum, and $\delta_{l/r}$ are the phases of the reflection amplitudes of the contacts. In the case the two leads are symmetric, which is the case we consider in this chapter, $r_1 = r_2 = r$, $t_1 = t_2 = t$, the transmission coefficient reduces to

$$\mathcal{T} = \frac{(|r|^2 - 1)^2}{(1 - |r|^2)^2 + 2|r|^2(1 - \cos\phi)} \tag{5.5}$$

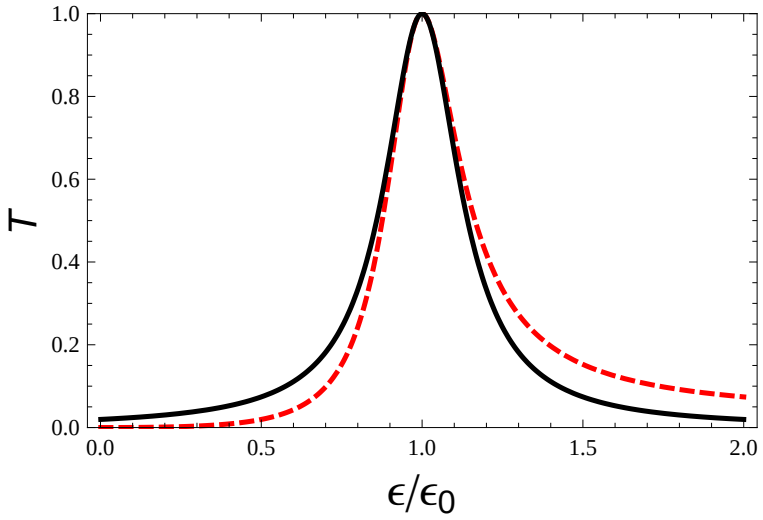

Figure 5.2: Dependence of the transmission coefficient $\mathcal{T}$ in Eq. (5.38) on ϵ/ϵ_0 (dashed line) with $N = 10$ and $\alpha \sim 1$. The solid curve is the Breit-Wigner resonance with the same resonance energy ϵ_0 and width.

Because at low energies the junctions become strongly reflective appreciable transmission through the device in this regime occurs only near resonances, where the phase ϕ equals an integer multiple of 2π. In the chain, $\epsilon \sim v_F k$ near the Fermi surface, so the energy spacing between adjacent resonances is $\sim \gamma_c/\mathcal{N}$.

To obtain a simplified expression for the transmission coefficient near a low energy resonance we write the reflection amplitudes of the junctions at low energies as $|r_{1/2}(\epsilon)| = 1 - c_{1/2}|\epsilon|/\gamma_g$, where $c_{1/2}$ is a numerical coefficient of the order of unity. This expression follows from Eq. (5.1). Linearizing the energy dependence of the phase ϕ near the resonance energy ϵ_0, $\phi = c_\phi(\epsilon - \epsilon_0)/\gamma_g$, where $c_\phi \sim \mathcal{N}$ is a numerical coefficient, we can write the transmission coefficient of the device as,

$$\mathcal{T}(\epsilon) = \left[\mathcal{T}_0^{-1} + \alpha\left(1 - \frac{\epsilon_0}{\epsilon}\right)^2\right]^{-1}. \tag{5.6}$$

Here $\mathcal{T}_0 = (c_1 + c_2)^2/(4c_1c_2)$ is the transmission coefficient at the resonance, and $\alpha = c_\phi^2/(4c_1c_2) \sim \mathcal{N}^2$.

The width of the resonance is of the order of $\epsilon_0/\mathcal{N}$. In the case of symmetric

contacts, $c_1 = c_2$, the device becomes perfectly transmitting on resonance. The shape of the resonance is shown in Fig. 5.2. It is strongly asymmetric and markedly different from the Breit-Wigner form which arises in the case of metal leads.

Since low energy transmission through the device proceeds via a single resonant state in the chain it is clear that Eq. (5.6) holds under very general conditions. The assumption that the coupling γ_c between the chain and the lead is energy independent holds as long as the propagation time of an electron across the junction is much shorter than the time of propagation across the chain. This is true if the SACC is longer than the junction (for example a small peninsular extending between the graphene lead and the chain). As long as the backscattering in the chain does not lead to localization the resonant state will remain coupled to both leads. The backscattering will merely modify its energy and the strength of the coupling to the leads, and can be accounted for by the change of parameters in Eq. (5.6). Similarly electron-electron interactions in a finite chain will renormalize the energy and the coupling of the resonant state with the leads.

In the remainder of the text we present a quantitative treatment of simple model of electron transport through a cumulene SACC interconnect between graphene leads. The transport properties through this structure also manifest in other molecular devices with graphene leads only if the electron states in the molecules extend to the graphene leads (i.e. they are not localized).

5.3 System and model

Consider an ideal cumulene SACC connected to graphene leads with perfect zigzag edges, as shown in Fig. 5.1.

As a first step in the theoretical analysis of the system, we assume that the atoms in the SACC are in the ideal cumulene configuration. We work in the noninteracting electron approximation and describe the electron motion in the conducting π_y and π_z bands using the nearest neighbor tight binding approximation. More complicated

band structure of the carbon wire will not significantly modify our conclusions.

Electron transport through the device is fully determined by the reflection amplitude of the contact between the SACC and the graphene lead. We derive in Sec. 5.3.1 a general formula for the reflection amplitude of the contact in terms of the local DoS in the lead evaluated at the atom which is connected to the SACC (Eq. (5.23). This expression applies for an arbitrary shape of the lead. Then in Sec. 5.3.2 we specialize to the case of graphene leads with zigzag edge. The zigzag edge is likely to be formed as a result of an electric failure [73] or a tear of a graphene strip because it has the least number of dangling bonds per unit length. We find that the edge states present in the case of zigzag edge provide a significant contribution to the tunneling DoS at the edge of the lead, and thus carry a significant portion of the current through the device.

5.3.1 Reflection amplitude of the junction

Let us first consider a single junction between the SACC and a graphene lead. We label the sites in the chain by an integer n which enumerates the atoms starting from the junction, see Fig. 5.1. The reflection amplitude of the contact can be found from the retarded Green function of the auxiliary system evaluated between two points inside the semi-infinite wire using the expression,

$$G(n, n') \sim \exp[-ik|n - n'|] + r(\epsilon) \exp[-ik(n + n')]. \tag{5.7}$$

Here k is the absolute value of the energy-dependent quasimomentum of the electron in the chain, and the Green function is defined in terms of the system Hamiltonian $\hat{H}$ in the standard way,

$$G(n, n') = \langle n|\hat{G}|n'\rangle = \langle n|(\epsilon_+ - \hat{H})^{-1}|n'\rangle, \tag{5.8}$$

where $\epsilon_+ = \epsilon + i0$.

We write Hamiltonian of the system as

$$\hat{H} = \hat{H}_w + \hat{H}_g + \hat{V}, \tag{5.9}$$

where $\hat{H}_w$ and $\hat{H}_g$ are respectively the Hamiltonians of the semi-infinite wire and the semi-infinite graphene lead, and $\hat{V}$ is the perturbation, which describes electron tunneling between them.

Introducing the Green function of the unperturbed system , $\hat{G}_0 = (\epsilon_+ - \hat{H}_w - \hat{H}_g)^{-1}$, we can express the Green function of the full system as

$$\hat{G} = \hat{G}_0 + \hat{G}_0 \hat{T} \hat{G}_0, \tag{5.10}$$

where $\hat{T}$ is the T-matrix of the junction between the chain and the lead given by

$$\hat{T} = (1 - \hat{V}\hat{G}_0)^{-1} \hat{V}. \tag{5.11}$$

In the nearest neighbor tight binding model the tunneling perturbation $\hat{V}$ couples only the $|n = 1\rangle$ orbital in the chain and a single contact site in the graphene lead, which we label as $|\mathbf{0}\rangle$. In the 2×2 subspace spanned by these states the tunneling perturbation $\hat{V}$ can be written as

$$\hat{V} = \gamma_c \begin{pmatrix} 0 & 1 \\ 1 & 0 \end{pmatrix}, \tag{5.12}$$

where γ_c is the hopping integral at the contact between the chain and the graphene lead. In this case the T-matrix depends only on the unperturbed Green function within the 2×2 subspace, where it has the form

$$\hat{G}_0 = \begin{pmatrix} G_g(\mathbf{0}, \mathbf{0}) & 0 \\ 0 & G_w(1,1) \end{pmatrix}. \tag{5.13}$$

Here $G_g(\mathbf{0}, \mathbf{0})$ is the Green function of the graphene lead at the contact site $|\mathbf{0}\rangle$ and $G_w(1,1)$ is the Green function of the semi-infinite wire at the site $n = 1$.

From Eqs. (5.11) and (5.12) it is clear that all matrix elements of the T-matrix outside the 2×2 subspace vanish. Therefore the Green function, Eq. (5.8), within the chain can be expressed in terms of the T-matrix of the contact as

$$G(n, n') = G_w(n, n') + G_w(n, 1)T(1, 1)G_w(1, n'). \tag{5.14}$$

Here $T(1, 1) = \langle 1|\hat{T}|1\rangle$ is the $(1, 1)$ matrix element of the T-matrix and

$$G_w(n, n') = \langle n|(\epsilon_+ - \hat{H}_w)^{-1}|n'\rangle$$

is the Green function of an isolated semi-infinite wire.

We use the tight binding model to describe the electron Hamiltonian of the chain,

$$\hat{H}_w = \gamma_w \sum_{n=1}^{\infty} \Big(u_w|n\rangle\langle n| + |n\rangle\langle n+1| + |n+1\rangle\langle n| \Big), \tag{5.15}$$

where γ_w is the nearest neighbor hopping matrix element in the wire, and the on-site energy $u_w\gamma_w$ describes the difference in the work functions between graphene and the carbon chain (in our notations the Fermi energy of the undoped graphene sheet is set to zero).

We construct the Green function of the semi-infinite wire from that of the infinite wire by adding a perturbation that nullifies the hopping between the two halves.

The retarded Green function of the infinite wire in k space is diagonal and given by

$$G_{0,w}(k) = (\epsilon - \epsilon_k + i0)^{-1} \tag{5.16}$$

with

$$\epsilon_k = u_w\gamma_w + 2\gamma_w \cos k. \tag{5.17}$$

The real space Green function is obtained by integrating over k as

$$G_0(n, n') = \frac{1}{2\pi} \int dk G_{0,w}(k) e^{ik(n-n')} \tag{5.18}$$

which gives

$$G_{0,w}(n, n') = \frac{1}{2i\gamma_w \sin k} \exp(-ik|n - n'|) \tag{5.19}$$

where k is the magnitude of the electron quasimomentum related to the energy by $\epsilon = u_w\gamma_w + 2\gamma_w \cos k$.

The perturbation $\hat{V}_w$ which cuts the wire to two halves has non-vanishing matrix elements only in the 2×2 subspace spanned by the orbitals with $n = 0$ and $n = 1$, where it is given by

$$\begin{pmatrix} V_w(0,0) & V_w(0,1) \\ V_w(1,0) & V_w(1,1) \end{pmatrix} = - \begin{pmatrix} 0 & \gamma_w \\ \gamma_w & 0 \end{pmatrix}. \tag{5.20}$$

The T matrix defined in Eq. (5.11) is also nonvanishing only in the 2×2 subspace and can be expressed solely in terms of the matrix elements of $\hat{G}_{0,w}$ in the 2×2 space,

$$\begin{pmatrix} G_{0,w}(0,0) & G_{0,w}(0,1) \\ G_{0,w}(1,0) & G_{0,w}(1,1) \end{pmatrix} = \frac{1}{2i\gamma_w \sin k} \begin{pmatrix} 1 & e^{-ik} \\ e^{-ik} & 1 \end{pmatrix}. \tag{5.21}$$

Using Eqs. (5.19), (5.20), (5.21), (5.10) and (5.11) we obtain the Green function of the semi-infinite wire, Eq. (5.22).

$$G_w(n,n') = \frac{1}{2i\gamma_w \sin k} \left(e^{-ik|n'-n|} - e^{-ik(n+n')} \right). \tag{5.22}$$

Here k is the magnitude of the electron quasimomentum, which is related to the energy of the electrons by $\epsilon = u_w\gamma_w + 2\gamma_w \cos k$.

With the aid of Eqs. (5.11), (5.12) and (5.13) we can readily express $T(1,1)$ in Eq. (5.14) in terms of the Green function of the graphene lead, $G_g(\mathbf{0},\mathbf{0})$. This yields for the combined Green function evaluated within the wire,

$$G(n,n') = \frac{e^{-ik(n'-n)}}{2i\gamma_w \sin k} \left[1 - \frac{1 - \gamma\, e^{ik}\, G_g(\mathbf{0},\mathbf{0})}{1 - \gamma\, e^{-ik}\, G_g(\mathbf{0},\mathbf{0})}\, e^{-2ikn} \right].$$

Here we introduced a combination of hopping integrals in the junction and in the chain, $\gamma = \gamma_c^2/\gamma_w$.

Comparing the last expression with Eq. (5.7) we obtain the reflection amplitude of the junction,

$$r(\epsilon) = -\frac{1 - \gamma\, e^{ik}\, G_g(\mathbf{0},\mathbf{0})}{1 - \gamma\, e^{-ik}\, G_g(\mathbf{0},\mathbf{0})}. \tag{5.23}$$

Equation (5.23) expresses the reflection amplitude at the contact in terms of the Green function of the lead at the contact point with the wire, $G_g(\mathbf{0},\mathbf{0})$, and holds for an arbitrary lead.

5.3.2 Graphene leads with zigzag edges

We now specialize to the case in which the graphene lead is terminated at the zigzag edge. The zigzag edge has the smallest number of broken bonds per unit length. It is therefore likely that the gap which appears in the graphene strip in the experiments of Ref. [73] is formed along this edge.

We use the nearest neighbor tight binding model to describe the electron dynamics in graphene and denote the electron π-orbitals localized at the atomic sites by $|A,\mathbf{N}\rangle$ (A sublattice) and $|B,\mathbf{N}\rangle$ (B sublattice). Here $\mathbf{N}=(N_1,N_2)$ labels the unit cell with a Bravais lattice vector $N_1\mathbf{a}_1+N_2\mathbf{a}_2$, see Fig. 5.1. The site $|A,\mathbf{N}=\mathbf{0}\rangle$ is chosen at the atom which is connected to the carbon chain.

In these notations $G_g(\mathbf{0},\mathbf{0})$ in Eq. (5.23) can be expressed in terms of the Green function of the semi-infinite graphene plane, $\hat{G}_g=(\epsilon_+-\hat{H}_g)$, as follows:

$$G_g(\mathbf{0},\mathbf{0})=\langle A,\mathbf{N}=\mathbf{0}|\hat{G}_g|A,\mathbf{N}=\mathbf{0}\rangle. \tag{5.24}$$

In order to evaluate the Green function of the semi-infinite plane $\hat{G}_g$ we start with the infinite graphene plane and add the perturbation $\hat{V}_g$, which nullifies the tunneling through the bonds which separate the plane into two halves along the zigzag edge, see Fig. 5.3.

The Green function of the infinite plane is diagonal in the quasimomentum representation due to the translation symmetry. We introduce the spinor Bloch functions as $\Psi^T_{\mathbf{k}}(\mathbf{N})=\exp(iK_1N_1+iK_2N_2)(\psi_A(\mathbf{k}),\psi_B(\mathbf{k}))$, where $\mathbf{k}$ is the quasimomentum, $K_1=\mathbf{k}\cdot\mathbf{a}_1$ and $K_2=\mathbf{k}\cdot\mathbf{a}_2$ are the projections of the quasimomentum onto $\mathbf{a}_1$ and $\mathbf{a}_2$, and $\psi_{A/B}$ are the wave function amplitudes on the A/B sublattices. In the quasimomentum representation the (inverse) Green function of an infinite graphene plane

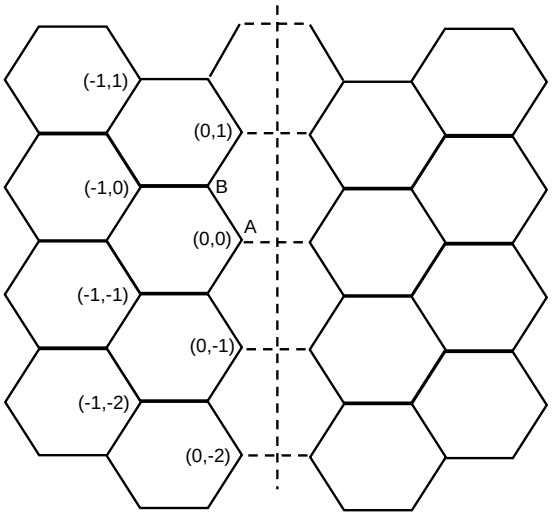

Figure 5.3: An infinite graphene plane is separated into two halves by adding the perturbation $\hat{V}_g$, which nullifies the tunneling along the dashed bonds.

can be written as a matrix in the A/B sublattice space,

$$G_{0,g}^{-1}(\mathbf{k}) = -\gamma_g \begin{pmatrix} -\varepsilon_+ & 1+e^{iK_1}+e^{-iK_2} \\ 1+e^{-iK_1}+e^{iK_2} & -\varepsilon_+ \end{pmatrix}. \tag{5.25}$$

Here γ_g denotes the nearest neighbor hopping integral in graphene and we introduced the dimensionless energy $\varepsilon_+ \equiv \epsilon_+/\gamma_g$.

The Dirac points at the corners of the hexagonal Brillouin zone correspond to $K_1 = K_2 = \pm 2\pi/3$. At these points the off-diagonal matrix elements in the above equation vanish. The Hamiltonian near these points reduces to the familiar Dirac equation with the linear spectrum near the Dirac points as shown in Fig. 2.1.

The perturbation $\hat{V}_g$ that cuts the graphene plane into two halves is given by (see

Fig. 5.3),

$$\hat{V}_g = \gamma_g \delta_{N_2,N_2'} \left[u_g \, \delta_{N_1,N_1'} \begin{pmatrix} \delta_{N_1,0} & 0 \\ 0 & \delta_{N_1,1} \end{pmatrix} - \begin{pmatrix} 0 & \delta_{N_1,0}\delta_{N_1',1} \\ \delta_{N_1,1}\delta_{N_1',0} & 0 \end{pmatrix} \right]. \tag{5.26}$$

The second matrix in the brackets nullifies electron tunneling between the two halves of the plane, and the first matrix describes the on-site potential for the atoms along the zigzag edge. This potential is parameterized in our model by the dimensionless parameter u_g, which is equal to the ratio of the on-site potential to the hopping integral γ_g. Because of the diminished number of neighbors for the edge atoms the on-site potential is expected to be positive and have a magnitude of the order of eV, i.e. of the same order as the hopping integral, $0 < u_g \leq 1$.

Due to the symmetry of the problem with respect to translations along the edge, $(N_1, N_2) \to (N_1, N_2+m)$ the corresponding quasimomentum, K_2, is conserved. Therefore below we use a mixed position/quasimomentum representation, (N_1, K_2).

In this representation the matrix $\hat{V}_g$ is independent of K_2 and has nonzero matrix elements only in the 2×2 space spanned by the states $|A, N_1 = 0\rangle$ and $|B, N_1 = 1\rangle$, which correspond to the carbon atoms on the opposite sides of the bonds cut. In this 2×2 subspace $\hat{V}_g$ is given by

$$V_g = \gamma_g \begin{pmatrix} u_g & -1 \\ -1 & u_g \end{pmatrix}. \tag{5.27}$$

The reflection amplitude of the junction, Eq. (5.23), depends only on the Green function of the semi-infinite graphene inside the same 2×2 subspace. In the mixed representation the latter satisfies the equation

$$G_g(K_2) = G_{0,g}(K_2) + G_{0,g}(K_2) V_g G_g(K_2), \tag{5.28}$$

where the perturbation V_g is given by Eq. (5.27) and $G_{0,g}(K_2)$ is the unperturbed

Green function inside the 2×2 subspace (in the mixed representation). The latter is evaluated in Appendix D and is given by

$$G_{0,g}(K_2) = \frac{1}{\gamma_g \sqrt{ab}} \begin{pmatrix} \varepsilon & 1-C+\varepsilon^2+\sqrt{ab} \\ 1-C+\varepsilon^2+\sqrt{ab} & \varepsilon \end{pmatrix}, \tag{5.29}$$

where we introduced the notations

$$C = 4\cos^2 \frac{K_2}{2},\ a = (1+\varepsilon)^2 - C,\ b = (1-\varepsilon)^2 - C. \tag{5.30}$$

The branch of $\sqrt{ab}$ in Eq. (5.29) is determined by analytic continuation of ε from the positive imaginary axis, where $\sqrt{ab}$ takes positive real values.

Using Eqs. (5.27), (5.28) and (5.29) we obtain

$$G_g(K_2) = \frac{2\sqrt{ab} + (1-u_g)a + (1+u_g)b}{\gamma_g[(1-u_g)^2 a - (1+u_g)^2 b]} \begin{pmatrix} 1 & 0 \\ 0 & 1 \end{pmatrix}. \tag{5.31}$$

The off-diagonal matrix elements in the above expression vanish, as they should due to the absence of tunneling between the two half-planes. The $(1,1)$ matrix element determines the Green function at the zigzag edge for a given quasimomentum K_2 along the edge. Its imaginary part gives the tunneling density of states into the edge for a given quasimomentum. It arises from two distinct contributions of the edge and bulk states, which we discuss next.

Tunneling density of states into the zigzag edge

The tunneling density of states at the zigzag edge of graphene is described by the imaginary part of the diagonal matrix elements in the Green function Eq. (5.31). Physically, the density of states at the edge contains the contributions from the bulk and edge states. The contribution of the bulk states is described by the imaginary part of $\sqrt{ab}$ whereas the contribution of the edge states corresponds to the pole at

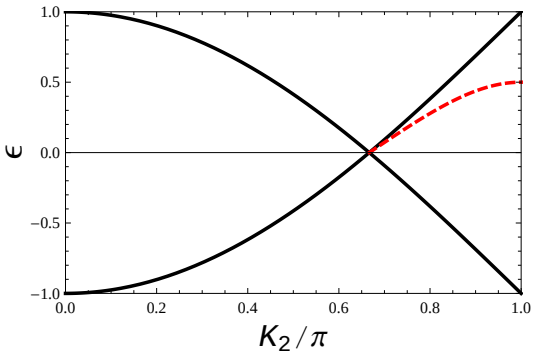

Figure 5.4: The solid curve represents the intersection of the bulk state spectrum of graphene with the $K_1 = 2\pi/3$ plane that goes through the Dirac point. The dashed curve represents the spectrum of the edge states, which exist only for $2\pi/3 < K_2 < \pi$. The edge state spectrum lies below the bulk state spectrum.

$(1-u_g)^2 a - (1+u_g)^2 b = 0$. This condition defines the spectrum of the edge states,

$$\varepsilon = \frac{1+u_g^2 - \sqrt{(1+u_g^2)^2 + 4u_g^2(2\cos K_2 + 1)}}{2u_g} \tag{5.32}$$

with $\cos K_2 < -\frac{1}{2}$.

This spectrum is plotted in Fig. 5.4. The inequality $\cos K_2 < -\frac{1}{2}$ reflects the fact that for $u_g > 0$, the edge states exist only for $\varepsilon > 0$ as shown in the following text. For $\varepsilon < 0$, the density of states for the edge states vanish, or the numerator in Eq. (5.31) vanishes together with the denominator, eliminating the pole.

For weak on-site potential at the edge, $u_g \ll 1$, the edge state spectrum reduces to $\varepsilon = -u_g(1 + 2\cos K_2)$, with $\cos K_2 \leq -\frac{1}{2}$. In this limit the spectrum and the wave functions of the edge states can be understood quite easily. In the absence of the on-site potential at the edge, $u_g = 0$, these states have wave functions which reside only on the A-sublattice and are eigenfunctions of the quasimomentum $\mathbf{k} = (K_1, K_2)$. It is easy to see from Eq. (5.32) that these states form a degenerate band of zero energy states, in agreement with Ref. [78]. From Eq. (5.25) it follows that in order to obey the Schrödinger equation in the interior of the lead the quasimomentum of such states must satisfy the condition $e^{-iK_1} = -1 - e^{iK_2}$. Further, since the wave function of

these states vanishes on the B-sublattice they remain eigenstates of the Hamiltonian even after the plane is separated into two halves. The normalizability condition for the edge states is $\mathrm{Im}K_1 < 0$, implying $|1 + e^{iK_2}| < 1$, which is equivalent to the inequality below Eq. (5.32). And the amplitude of the edge states decay with a factor of $2\cos(K_2/2)$. For weak on-site potential at the edge, $u_g \ll 1$ the edge state spectrum may be obtained from the first order in perturbation, $\varepsilon(K_2) = u_g|\psi_A(K_2)|^2$, where $\psi_A(K_2)$ is the wave function of the edge state at the edge atoms. The normalization condition gives $|\psi_A(K_2)|^2 = 1/\sum_{N_1=-\infty}^{0} \exp(2N_1 \mathrm{Im}K_1) = -(1 + 2\cos K_2)$.

The above consideration illustrates that in the presence of the on-site potential at the edge the band of edge states acquires a finite width of order of the on-site potential. For strong on-site potential at the edge perturbation theory is no longer applicable and the spectrum of the edge states is given by Eq. (5.32). At zero energy the spectrum of these states is linear, which results in a finite density of states in 1 dimension along the edge. It might seem therefore that at small energies, $\varepsilon \ll 1$, the contribution of the edge states to the tunneling density of states will be much larger than that of the bulk states. This is not so however because at small energies near $K_2 = 2\pi/3$ the wave functions of edge states extend into the bulk over many lattice spacings, so that the local density of such states at the edge vanishes linearly with energy. As a result, for $u_g \sim 1$ the contribution of these states to the tunneling DoS at the edge turns out to be of the same order as that of bulk states.

The real space Green function $G_g(\mathbf{0}, \mathbf{0})$ at the contact point is obtained by integrating the diagonal element of $G_g(K_2)(\mathbf{0}, \mathbf{0})$ in Eq. (5.31) over K_2: $G_g(\mathbf{0}, \mathbf{0}) = \int \frac{dK_2}{2\pi} G_g(K_2)$. We write this integral as a contour integral over the unit circle of the variable $z_2 = \exp(iK_2)$. Inside the contour the integrand has a simple pole corresponding to the edge states and a branch corresponding to the bulk states. We denote the contribution of the pole and the branch cut by G_{pole} and G_{bc} respectively,

$$G_g(\mathbf{0}, \mathbf{0}) = \frac{1}{\gamma_g}(G_{pole} + G_{bc}). \tag{5.33}$$

A lengthy but straightforward calculation gives,

$$G_{pole} = -i\frac{|\varepsilon|}{u_g}\frac{(1-u_g^2)\theta(\varepsilon)}{\sqrt{3u_g^2-2u_g\varepsilon-\varepsilon^2}}, \tag{5.34}$$

where $\theta(\epsilon)$ is the step function indicating that the density of states due to edge states is present only for $\varepsilon > 0$. The contribution of the branch cut, G_{bc}, can be evaluated analytically at low energies,

$$G_{bc} = -\frac{1}{3u_g} + \frac{\varepsilon}{\pi u_g}\frac{(1+u_g^2)}{\sqrt{3u_g^2-2u_g\varepsilon-\varepsilon^2}}\log\frac{2|\varepsilon|}{\sqrt{3(3u_g^2-2u_g\varepsilon-\varepsilon^2)}+3u_g-\varepsilon} - ic\frac{|\varepsilon|}{u_g}, \tag{5.35}$$

where $c = \frac{1}{2\pi}(1+\frac{\pi}{2}-\frac{2\pi}{3\sqrt{3}}) \approx 0.22$. The imaginary parts of both contributions (and with them the tunneling DoS at the edge) vanish linearly with energy at small energy.

Reflection coefficient of the junction at low energies

Substituting the previous Eqs. (5.33)-(5.35) into Eq. (5.23) we obtain a simple expression for the reflection coefficient of the junction at low energies, $|\varepsilon| \ll 1$,

$$|r(\epsilon)|^2 = 1 - \eta\varepsilon \tag{5.36}$$

with $\eta = -2\sqrt{4-u_w^2}[(1-u_g^2)/\sqrt{3u_g}+c]/(u_g+\frac{1}{9u_g}-\frac{u_w}{3})$. In this regime the electron wave incident from the carbon chain into the junction is almost perfectly reflected.

5.4 Device conductance at low energies: asymmetric resonances

The strong reflection at the junction at low energies indicates that the transmission coefficient of the whole device in Eq. (5.5) also tends to vanish at small energies except in the vicinity of resonances, $\cos(2\mathcal{N}k+2\delta_0)=1$. Substituting $|r_{r/l}(\epsilon)| = |r(\epsilon)|$ from Eq. (5.36) into Eq. (5.5) we obtain a simple expression for the transmission coefficient of the device at low energies,

$$\mathcal{T}(\epsilon) = \left[1+\frac{\kappa}{\epsilon^2}[1-\cos(2\mathcal{N}k+2\delta_0)]\right]^{-1}. \tag{5.37}$$

Here $\delta_0 = 2\arctan(\gamma/3u)$ is the contact scattering phase shift at zero energy and $\kappa = 2/\eta^2$, where η is a number of order unity defined below Eq. (5.36).

Expanding the cosine near a resonance energy $\epsilon = \epsilon_0$, we obtain a simple expression for the transmission coefficient at small energies,

$$\mathcal{T}(\epsilon) = \left[1 + \alpha\left(1 - \frac{\epsilon_0}{\epsilon}\right)^2\right]^{-1}, \tag{5.38}$$

where $\alpha = \mathcal{N}^2\kappa/2$ is a dimensionless parameter. This reproduces the result (5.6) expected from qualitative considerations in the case of symmetric coupling. The resonance width is $\Gamma \sim \epsilon_0/\mathcal{N}$. The resonance shape is strongly asymmetric and markedly different from that of the Breit-Wigner resonance, as shown in Fig. 5.2.

5.5 Summary and discussion

We studied electron transport through a single atom carbon chain connected to graphene leads. The simplicity of the hybridization pattern of electron orbitals in graphene and carbon chains enabled us to construct an analytically solvable model and thereby gain physical insight into the essential features of electron conduction in the system.

Transmission through the device is dominated by scattering at the contacts between the chain and the lead. For typical temperatures and doping levels in graphene the current-carrying electron states have energies much smaller than the band width. At these energies the contact between the chain and the lead becomes almost perfectly reflecting. Its reflection amplitude can be expressed in terms of the Green's function, $G_g(\mathbf{0}, \mathbf{0})$, of the lead at the atomic site connected to the carbon chain, see Eq. (5.23). In this equation the parameter γ describes the strength of coupling between the chain and the lead. At low electron energies the phase factor e^{ik} may be assumed energy independent, as it changes appreciably only at energy scales of order of the band width in the wire. In this regime the energy dependence of the transmission coefficient is dominated by that of the density of states in the lead. For graphene leads it becomes

linear, see Eqs. (5.36) and (5.1).

For leads with zigzag edges both the bulk and edge states contribute to the DoS at the contact point. Due to the difference in the on-site energy between the atoms at the edge and in the interior of graphene the band of edge states acquires a finite dispersion. The spectrum of this band is given by Eq. (5.32) and is plotted in Fig. 2.2. Although the edge state spectrum is linear at small energies its contribution to the local DoS at the edge is not constant, but rather is linear in the electron energy, $\sim \epsilon\theta(\epsilon)$. This occurs because the edge state wave functions extend into the bulk to distances which are inversely proportional to ϵ, as explained in Sec. 5.3.2. As the difference in the on-site potential between the atoms at the edge and in the interior of the lead is of the same order as the band width the contribution of edge states to the DoS is of the same order as that of the bulk states. Therefore a substantial part of the current through the carbon chain is propagated into the lead by the edge states. The energy dependence of the reflection coefficient of the junction is described by Eq. (5.36).

The interference between reflection amplitudes of the left and right junctions gives rise to the transmission coefficient of the device described by Eq. (5.37). Due to the nearly perfect reflection at the contact the energy dependence of the transmission coefficient of the interconnect has resonant character. Near the resonance the transmission coefficient is described by a simple expression, Eq. (5.38).

Our main conclusions, namely the linear energy dependence of the transmission coefficient of the junction between the chain and the lead and the shape of the resonance in Eq. (5.38) do not depend on many of the simplifying assumptions of our model.

The linear energy dependence of the junction transmission coefficient holds if the coupling between the chain and the lead is energy independent. This assumption is valid as long as the electron energy is smaller than the inverse propagation time across the contact and holds for more complicated junctions, e.g. a small peninsular

connecting the chain to the lead. In this case Eqs. (5.23) and (5.37) will still hold, provided γ and η are replaced by the appropriate parameters describing the coupling strength between the chain and the lead at low energies. Similarly, Eq. (5.38) will also hold provided the resonance energy and the parameter α are chosen appropriately. The generalization of the resonance shape to the case of asymmetric contacts is given by Eq. (5.6).

The resonant character of transmission will be preserved even in the presence of the Coulomb interaction in the wire, as long as the wire is short enough so that the one-dimensional correlation effects can be neglected. Such a wire will act as a molecule with a single resonant level participating in transport. For longer wires the one-dimensional correlations need to be taken into account. In this respect the Umklapp processes and the formation of Friedel oscillations near the contact points are especially important. The study of these effects is left for future work.

Appendix A

GREEN FUNCTION OF FREE PHONONS AND BOSONIC FIELDS

The calculation of the Green function of free phonons follows the same line as that of the Bosonic modes of Luttinger liquid because they both have the Hamiltonian of harmonic oscillators.

For convenience, we define a dimensionless phonon field

$$\phi_\nu(x) = \sqrt{\rho s} u_\nu(x) \tag{A.1}$$

and the corresponding conjugate momentum

$$\Pi_\nu(x) = -i\partial_\tau \phi_\nu(x)/s_\nu \tag{A.2}$$

The action of free phonons in imaginary time space is

$$\begin{aligned} S_{0-ph} &= \int_0^\beta d\tau \int dx [\tfrac{1}{2s_T}(\partial_\tau \phi_T)^2 + \tfrac{s_T}{2}(\partial_x \phi_T)^2] + \int_0^\beta d\tau \int dx [\tfrac{1}{2s_o}(\partial_\tau \phi_\nu)^2 + \tfrac{\omega_o^2}{2s_o}(\phi_o)^2] \\ &= \tfrac{1}{2}\sum_{\nu,q} \tfrac{1}{s_\nu}(\omega_n^2 + \omega_\nu^2)\phi_\nu(q)\phi_\nu(-q) \end{aligned} \tag{A.3}$$

where $q = (\omega_n, k)$, $\omega_\nu = \omega_o$ for the optical phonon and $\omega_\nu = s_T k$ for the TA phonon.

$$\phi_\nu(r) = \frac{1}{\sqrt{\beta L}} \sum_q \phi_\nu(q) e^{iqr} \tag{A.4}$$

The correlator $< AB >$ is equal to

$$< AB >_0 = \frac{1}{Z} \int \prod_{\nu,j} \mathcal{D}\phi_\nu \mathcal{D}\Pi_\nu AB e^{-S_{0E}/\hbar} \tag{A.5}$$

where

$$Z = \int \prod_{\nu,j} \mathcal{D}\phi_\nu \mathcal{D}\Pi_\nu \mathcal{D} e^{-S_{0E}/\hbar} \tag{A.6}$$

is the partition function.

The correlators for phonon fields are then

$$< T\phi_\nu(r_1)\phi_\nu(r_2) >_{q0} = \frac{s_\nu}{\omega_n^2 + \omega_\nu^2}. \tag{A.7}$$

For Bosonic fields of the Luttinger liquid,

$$< T\Phi_j(q)\Phi_j^+(q) >_0 = \frac{\pi K_j}{\frac{\omega_n^2}{u_j} + u_j k^2}. \tag{A.8}$$

The interested real space correlators of TA phonon is

$$\begin{aligned} < \nabla\phi_T(r)\nabla\phi_T(0) > &= \int d\omega dk \frac{k^2 e^{iqr}}{-\frac{\omega^2}{s_T} + s_T k^2} \\ &= \frac{(s_T\tau)^2 - x^2}{[(s_T\tau)^2 + x^2]^2} \end{aligned} \tag{A.9}$$

For Bosonic fields

$$< T[\Phi_j(r) - \Phi_j(0)]^2 >_0 = K_j F_{1j}(r) \tag{A.10}$$

where

$$\begin{aligned} F_{1j}(r) &= \frac{1}{\beta L}\sum_q [1 - \cos(kx + \omega\tau)]\frac{2\pi u_j}{\omega_n^2 + u_j^2 k^2} \\ &= \int_0^\infty dk \frac{e^{-\xi k} f_B(u_j k) 2(1 - cos(kx)cosh(\tau u_j k))}{k} \\ &\quad + \int_0^\infty dk \frac{e^{-\xi k}(1 - cos(kx)e^{-u_j k|\tau|})}{k}, \end{aligned} \tag{A.11}$$

and ξ is an upper momentum cutoff. The factor $e^{-\xi k}$ is to prevent the integral from diverging.

At finite temperature and $(x, u\tau) \gg \xi$,

$$F_{1j}(r) = \frac{1}{2} log[\frac{\beta^2 u_j^2}{\pi^2 \xi^2}(sinh^2(\frac{\pi x}{\beta u_j}) + sin^2(\frac{\pi\tau}{\beta}))] \tag{A.12}$$

When $\frac{\xi}{u_j} \ll \beta$, i.e. at temperature much lower than the energy bandwidth, $F_{1j}(r)$ reduces to a much simpler form

$$F_{1j}(r) = \frac{1}{2} log[\frac{x^2 + (u_j \mid \tau \mid + \xi)^2}{\xi^2}] \tag{A.13}$$

Appendix B

FUSION RULES

Equation (3.8) can be derived by noting that both the Umklapp and electron-phonon backscattering Hamiltonian densities have exponential dependence of the charge field Φ_{c+}, $\sim (e^{ia_\eta \Phi_{c+}} + h.c.)$ and using the following identity that holds for Gaussian averages,

$$\begin{aligned}
&\langle \phi_{c+}(x) e^{ia_\eta \phi_{c+}(x_1)} e^{-ia_\eta \phi_{c+}(x_2)} \phi_{c+}(x') \rangle_0 = \\
&-(ia_\eta)^2 \langle \phi_{c+}(x)\phi_{c+}(x_1)\rangle_0 \langle e^{ia_\eta \phi_{c+}(x_1)} e^{-ia_\eta \phi_{c+}(x_2)}\rangle_0 \langle \phi_{c+}(x_2)\phi_{c+}(x')\rangle_0 \\
&+(ia_\eta)^2 \langle \phi_{c+}(x)\phi_{c+}(x_1)\rangle_0 \langle e^{ia_\eta \phi_{c+}(x_1)} e^{-ia_\eta \phi_{c+}(x_2)}\rangle_0 \langle \phi_{c+}(x_1)\phi_{c+}(x')\rangle_0 + \\
&\text{same terms with } x_1 \leftrightarrow x_2 + \langle \phi_{c+}(x)\phi_{c+}(x')\rangle_0 \langle e^{ia_\eta \phi_{c+}(x_1)} e^{-ia_\eta \phi_{c+}(x_2)}\rangle_0 . \qquad \text{(B.1)}
\end{aligned}$$

This formula can be derived by expanding the exponentials in the left hand side in the Taylor series and applying Wick's theorem to each term. The resulting series sums to the expression in the right hand side.

The last term in the right hand side corresponds to a disconnected diagram and does not contribute to the correlation function.

Appendix C

RENORMALIZATION GROUP EQUATIONS IN THE MARGINALLY IRRELEVANT BACKSCATTERING CASE

In this appendix, we use the real space renormalization group method invented by Anderson, Yuval and Hamann to derive the RG equations for the backscattering coupling constants in Eq.(4.21).

As shown in the text, the effective Hamiltonian we study is

$$H_{eff} = \Lambda[r_4 \cos(4\Phi_{c+}) + \cos(2\Phi_{c+}) \sum_a r_a \cos(2\Phi_a)] \tag{C.1}$$

where $\Lambda = v_F/\xi$ is the high energy cutoff, r_4, r_a are dimensionless amplitudes and a labels the neutral modes.

The partition function of the above Hamiltonian is

$$\frac{Z}{Z_0} = \frac{1}{Z_0} \int \prod_j \mathcal{D}\Phi_j e^{-S_0 - \int H_{eff} d\tau} \tag{C.2}$$

where S_0 is the action of the Luttinger liquid Hamiltonian Eq. (4.4), Z_0 is the partition function corresponding to action S_0. To obtain the RG equations to the order of r_a^2,

we expand the partition function to the 3rd order as

$$\begin{aligned}
\frac{Z}{Z_0} &= 1+\frac{1}{2}\int \Lambda^2 d\tau_1 d\tau_2 \left\{ \langle \cos 2\Phi_{c+}(\tau_1)\cos 2\Phi_{c+}(\tau_2)\rangle \left[\sum_a r_a^2 \langle \cos 2\Phi_a(\tau_1)\cos 2\Phi_a(\tau_2)\rangle\right] \right. \\
&\quad \left. + \; r_4^2 \langle \cos 4\Phi_{c+}(\tau_1)\cos 4\Phi_{c+}(\tau_2)\rangle \right\} \\
&\quad - \frac{1}{3!}\int \Lambda^3 d\tau_1 d\tau_2 d\tau_3 3\langle \cos 2\Phi_{c+}(\tau_1)\cos 2\Phi_{c+}(\tau_2)\cos 4\Phi_{c+}(\tau_3)\rangle \\
&\qquad\qquad \left[\sum_a r_a^2 \langle \cos 2\Phi_a(\tau_1)\cos 2\Phi_a(\tau_2)\rangle\right] \\
&= 1+\frac{1}{2}\int_{\tau_c} \Lambda^2 d\tau_1 d\tau_2 \left[\frac{1}{4}\sum_a r_a^2 \left(\frac{\tau_c}{\tau_1-\tau_2}\right)^{2+2k_{c+}} + \frac{1}{2} r_4^2 \left(\frac{\tau_c}{\tau_1-\tau_2}\right)^{8K_{c+}}\right] \\
&\quad -\frac{1}{2}\int_{\tau_c} \Lambda^3 d\tau_1\tau_2\tau_3 \frac{1}{8}\frac{(\tau_1-\tau_2)^{2K_{c+}}\tau_c^{2K_{c+}}}{[(\tau_1-\tau_3)(\tau_2-\tau_3)]^{4K_{c+}}}\sum_a r_a^2 r_4 \frac{\tau_c^{2K_a}}{(\tau_1-\tau_2)^{2K_a}} \qquad \text{(C.3)}
\end{aligned}$$

The procedure involves first integrating out the correlation functions with distance between τ_c and $\tau_c + d\tau_c$ and then rescaling the cutoff $\tau_c + d\tau_c$ back to τ_c, which is equivalent to first integrating out the fast mode in k space and then rescaling k to restore the whole Hilbert space. After the procedure, we get

$$\begin{aligned}
\frac{Z}{Z_0} &= 1+\frac{1}{2}\int_{\tau_c} \Lambda^2 d\tau_1' d\tau_2' \left[\frac{1}{4}\sum_a r_a^2 \left(\frac{\tau_c}{\tau_1'-\tau_2'}\right)^{2+2K_{c+}} e^{-2K_{c+}dl} + \frac{1}{2} r_4^2 \left(\frac{\tau_c}{\tau_1'-\tau_2'}\right)^{8K_{c+}} e^{(2-8K_{c+})dl}\right] \\
&\quad + \frac{1}{4}\int_{\tau_c} \Lambda^2 d\tau_1 d\tau_2 \sum_a r_a^2 r_4 (\frac{\tau_c}{\tau_1-\tau_2})^{2+2K_{c+}} \ln\frac{\tau_c+d\tau_c}{\tau_c} \\
&\quad + \frac{1}{8}\int_{\tau_c} \Lambda^2 d\tau_1 d\tau_2 \sum_a r_a^2 r_4 (\frac{\tau_c}{\tau_1-\tau_2})^{8K_{c+}} \frac{d\tau_c}{\tau_c} \\
&\quad -\frac{1}{2}\int_{\tau_c} \Lambda^3 d\tau_1 d\tau_2 d\tau_3 \frac{1}{8}\frac{(\tau_1-\tau_2)^{2K_{c+}}\tau_c^{2K_{c+}}}{[(\tau_1-\tau_3)(\tau_2-\tau_3)]^{4K_{c+}}}\sum_a r_a^2 r_4 \frac{\tau_c^{2K_a}}{(\tau_1-\tau_2)^{2K_a}} e^{(1-2K_{c+})dl} \qquad \text{(C.4)}
\end{aligned}$$

In the above equation, $e^{dl} \equiv \frac{\tau_c+d\tau_c}{\tau_c}$ and we already take $K_a = 1$ for the neutral modes. From above, we get the RG equation for the backscattering coupling constants as shown in the text,

$$dr_a/dl = -\epsilon\, r_a + r_a r_4, \qquad \text{(C.5)}$$

$$dr_4/dl = -4\epsilon_4 r_4 + \sum_a r_a^2/4, \qquad \text{(C.6)}$$

where $\epsilon \equiv K_{c+}$, $\epsilon_4 \equiv K_{c+} - \frac{1}{4}$.

Appendix D

DERIVATION OF THE GREEN FUNCTION OF A HALF GRAPHENE SHEET

In this appendix we derive the expression for the half plane graphene Green function within the 2×2 subspace spanned by the rows of atoms on the opposite sides of the dashed link in Fig. 5.3.

The unperturbed Green function in the quasimomentum representation is obtained by inverting the matrix in Eq. (5.25),

$$G_{0,g}(\mathbf{k}) = -\frac{1}{D}\begin{pmatrix} -\varepsilon & 1+e^{iK_1}+e^{-iK_2} \\ 1+e^{-iK_1}+e^{iK_2} & -\varepsilon \end{pmatrix},$$

where $D = \gamma_g\left[\varepsilon^2 - (1+e^{-iK_1}+e^{iK_2})(1+e^{iK_1}+e^{-iK_2})\right]$.

In the mixed representation the Green function $\hat{G}_{0,g}(K_2)$ in the 2×2 subspace of states $|A, N_1 = 0\rangle$ and $|B, N_1 = 1\rangle$, can be obtained by the inverse Fourier transform of $G_{0,g}(\mathbf{k})$ with respect to K_1. An elementary calculation gives

$$\begin{aligned} &\langle A,0|\hat{G}_{0,g}(K_2)|A,0\rangle = \langle B,1|\hat{G}_{0,g}(K_2)|B,1\rangle \\ &= \int \frac{dK_1}{2\pi}\frac{\varepsilon}{D} = \frac{\varepsilon}{\gamma_g\sqrt{ab}}, \end{aligned} \tag{D.1}$$

and

$$\begin{aligned} &\langle A,0|\hat{G}_{0,g}(K_2)|B,1\rangle = \langle B,1|\hat{G}_{0,g}(K_2)|A,0\rangle^* \\ &= -\int \frac{dK_1}{2\pi}\frac{1+e^{iK_1}+e^{-iK_2}}{D}e^{-iK_1} \\ &= \frac{1}{\gamma_g\sqrt{ab}}\left[1 - C + \varepsilon^2 + \sqrt{ab}\right], \end{aligned} \tag{D.2}$$

where a, b and C are defined in Eq. (5.30).

Combining the above matrix elements into one 2×2 matrix we arrive at Eq. (5.29).

BIBLIOGRAPHY

[1] F.D. M. Haldane, J.Phys.C14,2585(1981); Phys. Rev. Lett. 47 1840(1981); M.P.A.Fisher and L.I.Glazman, arXiv:cond-mat/9610037v1

[2] For a review, see R. Saito, G. Dresselhaus, and M. S. Dresselhaus, *Physical Properties of Carbon Nanotubes* (Imperial College Press, London 1998).

[3] V. V. Deshpande, B. Chandra, R. Caldwell, D. Novikov, J. Hone, M. Bockrath, Science 323, 106 (2009).

[4] G.Gruner, *density waves in solids* (Addison Wesley publishing company)(1994)

[5] P.R. Wallace, Phys. Rev. 71, 622(1947)

[6] R Egger, A. O. Gogolin, Euro. Phys. J. B, **3**, 281(1998)

[7] J. W. Mintmire, B. I. Dunlap, and C. T. White, Phys. Rev. Lett. **68**, 631 (1992).

[8] M. T. Figge, M. Mostovoy, and J. Knoester, Phys. Rev. Lett. **86**, 4572 (2001); Phys. Rev. B **65**, 125416 (2002).

[9] H. Suzuura, and T. Ando, in *Proc. of the 25th Internat. Conf. on Phys. of Semiconductors*, p 1625, edited by N. Miura and T. Ando (Springer 2001).

[10] N. Viet, H. Ajiki and T. Ando, J. Phys. Soc. Jpn. **63**, 3036 (1994).

[11] H. Ajiki and T. Ando, J. Phys. Soc. Jpn. **65**, 505 (1996).

[12] D. Connétable, G.-M. Rignanese, J.-C. Charlier, and X. Blase, Phys. Rev. Lett. **94**, 015503 (2005).

[13] C. Kane, L. Balents, and M. P. A. Fisher, Phys. Rev. Lett. **79**, 5086 (1997).

[14] R. Egger and A. Gogolin, Phys. Rev. Lett. **79**, 5082 (1997).

[15] A. Odintsov and H. Yoshioka, Phys. Rev. B **59**, R10457 (1999).

[16] A. A. Nersesyan and A. M. Tsvelik, Phys. Rev. B **68**, 235419 (2003).

[17] R. Jishi, M. S. Dresselhaus and G. Dresselhaus, Phys. Rev. B **48**, 11385 (1993).

[18] H. Suzuura and T. Ando, Phys. Rev. B **65**, 235412 (2002).

[19] G. D. Mahan, Phys. Rev. B **68**, 125409 (2003).

[20] D. Mann *et al.*, Nano Lett. **3**, 1541 (2003).

[21] Strong e-ph forward scattering can lead to the Bardeen-Wentzel instability; see A. De Martino and R. Egger, Phys. Rev. B **67**, 235418 (2003). However, for the values of the e-ph couplings quoted in the literature [17] this does not occur even in the narrowest tubes, and thereby imply only inessential corrections to our treatment.

[22] O. Dubay, G. Kresse , and H. Kuzmany, Phys. Rev. Lett. **88**, 235506 (2002).

[23] L. Balents and M. P. A. Fisher, Phys. Rev. B **55**, R11973 (1997).

[24] T. Giamarchi, *Quantum Physics in One Dimension*, (Clarendon Press 2003).

[25] A. M. Tsvelik, *Quantum Field Theory in Condensed Matter Physics*, (Cambridge 2003).

[26] H. Frohlich, Proc. R. Soc. London Ser. A **215**, 291 (1952).

[27] S. Barisic, J. Labbé, and J. Friedel, Phys. Rev. Lett. **25**, 919 (1970).

[28] S. G. Lemay *et al.*, Nature **412**, 617 (2001).

[29] A. R. Hall *et al.*, Phys. Rev. Lett. **96**, 256102 (2006).

[30] M.S. Purewal *et al*, Phys. Rev. Lett. **98**, 186808 (2007).

[31] S.M. Bachilo *et al.*, Science **298**, 2361 (2002).

[32] J. Lefebvre, Y. Homma, and P. Finnie, Phys. Rev. Lett. **90**, 217401(2003).

[33] A. Hagen and T. Hertel, Nano Lett. **3**, 383 (2003).

[34] O.J. Korovyanko, C.X. Sheng, Z.V. Vardeny, A.B. Dalton, R.H. Baughman, Phys. Rev. Lett. **92**, 017403(2004).

[35] P. Avouris, M. Freitag, V. Perebeinos, Nature Photonics, **2**, 341(2008).

[36] C. Kramberger, *et al.*, Phys. Rev. Lett. **100**, 196803 (2008).

[37] Z. Zhong, N.M. Gabor, J.E. Sharping, A.L. Gaeta, P.L. McEuen, Nature Nanotechnology, **3**, 201 (2008).

[38] M. Bockrath, D.H. Cobden, J.G. Lu, A.G. Rinzler, R.E. Smalley, L. Balents, and P.L. McEuen, Nature **397**, 598 (1999).

[39] Z. Yao, H.W.Ch. Postma, L. Balents, C. Dekker, Nature **402**, 273 (1999).

[40] G.D. Mahan, *Many particle physics*, Kluwer Academic/Plenum Publishers (2000).

[41] D. Prober, private communication

[42] H. Yoshioka Phys. Rev. B **61**, 7316 (2000).

[43] M.I. Katsnelson, K.S. Novoselov and A.K. Geim, Nature Physics, **2** 620 (2006).

[44] D. L. Maslov and M. Stone, Phys. Rev. B **52**, R5539 (1995); V. V. Ponomarenko, ibid. **52**, R8666 (1995); I. Safi and H. J. Schulz, ibid. **52**, R17040 (1995).

[45] V.V. Ponomarenko, Phys. Rev. B **52**, R8666 (1995).

[46] I. Safi and H. J. Schulz, Phys. Rev. B **52**, R17040 (1995).

[47] E.G. Mishchenko, L.I. Glazman, *unpublished*

[48] W. Chen, A.V. Andreev, A.M. Tsvelik, and D. Orgad, Phys. Rev. Lett. **101**, 246802 (2008).

[49] C.L. Kane *et al*, Europhys. Lett., **41**(6), 683 (1998).

[50] J.Y. Park *et al*, Nano Lett. **4**, 517 (2004).

[51] E.G. Mishchenko, M.Yu. Reizer, and L.I. Glazman Phys. Rev. B **69**, 195302 (2004).

[52] Wei Chen, A.V. Andreev, L.I.Glazman, Phys. Rev. Lett. 106, 216801(2011)

[53] M. Gabor, *et al.* Science **325**, 1367 (2009).

[54] W. Chen, A.V. Andreev, E.G. Mishchenko, L.I. Glazman, Phys. Rev. B **82**, 115444(2010).

[55] C.L. Kane, M.P.A. Fisher, Phys. Rev. Lett. **68**, 1220 (1992); Phys. Rev. B. **46**, 15233 (1992).

[56] H. Yi, and C. Kane, Phys. Rev. B **57**, R5580 (1998).

[57] H. Ajiki and T. Ando, J. Phys. Soc. Jpn. **62**, 1255(1993); ibid. **65**, 505(1996).

[58] A.V. Andreev, Phys. Rev. Lett. **99**, 247204 (2007).

[59] S.L. Sondhi, S.M. Girvin, J.P. Carini, and D. Shahar Rev. Mod. Phys. **69**, 315 (1997).

[60] M. A. Reed, C. Zhou, C. J. Muller, T. P. Burgin, and J. M. Tour, Conductance of a molecular junction. Science **278**, 252 (1997).

[61] J. Chen, M. A. Reed, A. M. Rawlett, and J. M. Tour, Science **286**, 1550 (1999).

[62] H. Park, J. Park, A.K.L. Lim, E.H. Anderson, A.P. Alivisatos, and P.L. McEuen, Nature **407**, 57 (2000).

[63] J. Park *et al.*, Nature **417**, 722 (2002).

[64] W. Liang *et al.*, Nature **417**, 725 (2002).

[65] N. Agrait, A. L. Yeyati, J. M. van Ruitenbeek, Physics Reports, **377**, 81, (2003).

[66] P. L. McEuen, Nature **393**, 15 (1998).

[67] S. Iijima, Nature **354**, 56 (1991).

[68] K. S. Novoselov, A. K. Geim, S. V. Morozov, Science **306**, 666 (2004).

[69] N. D. Lang, and Ph. Avouris Phys. Rev. Lett. **81**, 3515 (1998).

[70] G. Cuniberti, G. Fagas, and K. Richter, J. Chem. Phys. **281**, 465 (2002).

[71] T.D. Yuzvinsky, W. Mickelson, S. Aloni, G. E. Begtrup, A. Kis, A. Zettl, Nano Lett. **6** 2718(2006).

[72] K.H. Khoo, J.B. Neaton, Y.W. Son, M.L. Cohen, and S.G. Louie, Nano Letters **8** 2900 (2008).

[73] B. Standley, W. Bao, H. Zhang, J. Bruck, C. N. Lau, and M. Bockrath, Nano Letters **8**, 3345 (2008).

[74] C. Jin, H. Lan, L. Peng, K. Suenaga and S. Iijima, Phys. Rev. Lett. **102**, 205501(2009)

[75] B. Larade, J. Taylor, H. Mehrez and H. Guo, Phys. Rev. B., **64**, 075420(2001).

[76] S. Tongay, R.T. Senger, S. Dag, and S. Ciraci, Phys. Rev. Lett. **93**, 136404-1(2004).

[77] Z. Crljen and G. Baranovic, Phys. Rev. Lett., **98**, 116801(2007).

[78] M. Fujita, K. Wakabayashi, K. Nakada, and K. Kosukabe, J. Phys. Soc. Jap. Lett., **7**, 1920 (1996).

[79] K. Nakada *et al*, Phys. Rev. B **54**, 17954(1996).

[80] L.D. Landau and E.M. Lifshitz, *Quantum Mechanics (non-relativistic theory)*, § 102, Butterworth-Heinemann (Oxford, 1997).

[81] S.Okano and D. Tomanek, Phys. Rev. B **75**, 195409(2007)

[82] G. Seelig and K. A. Matveev, Phys. Rev. Lett. **90**, 176804 (2003).

[83] G. Seelig, K. A. Matveev, and A. V. Andreev, Phys. Rev. Lett. **94**, 066802 (2005).

VITA

Wei Chen was born on Nov. 17th, 1981 in Hubei, China. She obtained her Bachelor's and Master's degree in Nanjing University in 2002 and 2005 respectively. She then went to University of Washington at Seattle in 2005 for a PHD degree and finished this dissertation in June, 2011.